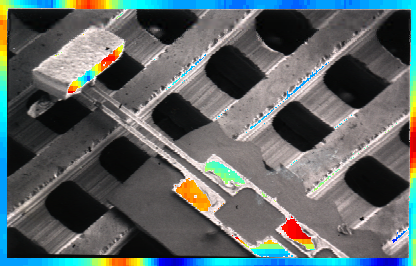

Study of Photonic Crystal Structures and their Application in the field of Antennas

Memoria de la Tesis Doctoral realizada por

Ramón Gonzalo García

Y dirigida por

Dr. Peter de Maagt
Dr. Mario Sorolla Ayza

Para optar al grado de

Doctor Ingeniero de Telecomunicación

Departamento de Ingeniería Eléctrica y Electrónica
Universidad Pública de Navarra

Pamplona, Mayo de 2000

Study of Photonic Crystal Structures and their Application in the field of Antennas

Memoria de la Tesis Doctoral realizada por
Ramón Gonzalo García
Y dirigida por
Dr. Peter de Maagt
Dr. Mario Sorolla Ayza
Para optar al grado de
Doctor Ingeniero de Telecomunicación

Departamento de Ingeniería Eléctrica y Electrónica
Universidad Pública de Navarra

Pamplona, Mayo de 2000

A María sin la que esta tesis nunca hubiese visto la luz

Agradecimientos

Es en estos momentos, con la tesis acabada o a punto de estarlo, cuando uno echa la vista atrás y se da cuenta del tiempo transcurrido y de todas aquellas personas que de una u otra manera aportaron su granito de arena para que esta tesis "por fin" viera la luz. Espero mencionar a todos, pero si alguno olvido, desde aquí van mis más sinceras disculpas.

Todavía me acuerdo del día en que llegue como becario del Ministerio de Educación y Ciencia al centro de la Agencia Espacial Europea en Holanda, y como el Dr. Peter de Maagt, gran artífice de que este trabajo haya llegado a buen término, confió en mí y me animó a que trabajara con él en un tema completamente desconocido para mí, pero a la vez tan excitante y con tantas posibilidades que atrajo rápidamente mi atención: "Photonic Band Gap" estructuras para aplicaciones de antenas. Ahí empezó mi gran reto.

Durante este tiempo el Dr. Peter de Maagt me ha ayudado en todo lo que ha podido y más, ha puesto todo su empeño y ganas en que este trabajo saliera adelante y al final se ha convertido en un gran amigo. A mi regreso a España siempre ha estado en contacto conmigo, ofreciéndome todo su apoyo y asistencia. Gracias de verdad, mucho de lo que hay aquí se lo debo a él.

Desde mis inicios en la Universidad el Dr. Mario Sorolla ha estado siempre ahí, animándome en todo y ofreciéndome toda su ayuda y experiencia. Han sido muchos años de convivencia, apoyo y confianza.

De todos los años en la "Uni", me gustaría hacer una mención especial al Dr. Carlos del Río, con el que la "vida" en la universidad se ha hecho realmente agradable, siempre escucha, apoya, y ofrece todo lo que tiene. Es un amigo de los que merecen la pena. Gracias Carlos por todo, realmente te debo mucho. Y por supuesto, no me puedo olvidar de Jorge y Bea, ¿qué puedo decir de ellos?, risas, alegrías, cenas, apoyo, ayuda,…..mucho a cambio de poco y de Libertad por su interés y ayuda. No puedo olvidarme tampoco de mis proyectistas, Gemma, Cristina y Maite con esos cálculos de última hora.

De mi época en Holanda, hay personas a las que siempre podré llamar amigos. Arturo que compartió conmigo despacho, desayunos, comidas y alguna que otra ayudita técnica. Eduardo y Félix, inseparables compañeros de piso, fútbol, juergas y charlas en cualquier momento y circunstancia. Emilio, Haviei y Maite con los que los viajes por Europa fueron muy agradables. Gracias a todos por estar ahí siempre que os necesité, con gente así se descubre el verdadero valor de la palabra "amistad".

Durante esta última época, y debido a mi estancia en el RAL, he conocida a una persona, el Dr. Chris Mann, que además de ofrecerme toda su ayuda y tiempo, trasmite un entusiasmo increíble que ayuda a superar cualquier adversidad. Es capaz de hacer fácil lo imposible. Gracias por todo, la última parte de la tesis no hubiese sido posible sin él.

Me gustaría agradecer a la gente del Grupo de Microondas de la Upna, destacando al Dr. Alberto Sánchez por su desinteresada revisión de la tesis, así como a los miembros de la división de Electromagnetismo (TOS-EEA) de ESA-ESTEC, y a la división de milimétricas del RAL por su apoyo durante mi estancia en dichos centros.

El apoyo institucional también merece ser reflejado: a la Universidad Pública de Navarra, al Ministerio de Educación y Ciencia por su apoyo económico a través de una beca FPI.

Por último, aunque no menos importante me gustaría agradecer de todo corazón a mis padres y a mi hermano por sacrificarse por mí y darme todo aquello que pudieron; y por supuesto a María, el alma de esta tesis, apoyo en los momentos difíciles, paciencia cuando era necesaria, comprensión, alegría,…. la mejor compañera que se puede tener. En esta recta final “Pablito” ha sido una gran motivación, se me ha adelantado por la mano.

RESUMEN

El propósito principal perseguido en esta tesis ha sido el diseño de estructuras “Photonic Crystal” y sus aplicaciones como substratos para antenas. Estos “Photonic Crystal” se definen como estructuras periódicas en una, dos o tres dimensiones las cuales no permiten la propagación de una onda electromagnética en su interior para cualquier dirección de propagación de la onda incidente en un determinado rango de frecuencias (“bandgap”).

Uno de los principales problemas que presentan hoy en día las antenas es la potencia que se transfiere a los modos de substratos. Esta energía no contribuye a la radiación principal de la antena, considerándose un mecanismo de pérdidas. Además, esta energía, dependiendo de la constante dieléctrica del substrato y de su grosor puede suponer más del 70% de la potencia total. Incluso algunas veces esta energía contribuye de forma negativa a la radiación principal, deteriorando en gran medida el diagrama de radiación de la antena. La idea fundamental es utilizar estructuras “Photonic Crystal” como substratos de antenas. Al no permitir la propagación de la onda electromagnética en su interior, no se excitarán modos de substrato y toda la potencia será radiada por la antena. Esto se traducirá en un incremento de la eficiencia y de la directividad de la antena, en la obtención de diagramas de radiación más simétricos y en la reducción de la radiación trasera.

La tesis se puede dividir fundamentalmente en dos partes.

- Inicialmente, en el Capítulo 2 se presentan las ecuaciones de Maxwell para estructuras dieléctricas periódicas. Con estas ecuaciones se ha formulado un sistema con el que se pueden obtener los autovalores y autovectores de cualquier “Photonic Crystal” de una, dos o tres dimensiones. La solución de este sistema son los diagramas de dispersión de la estructura, los cuales caracterizan completamente el comportamiento de cualquier “Photonic Crystal”. Estos diagramas de dispersión informan sobre la existencia de un “bandgap” completo o parcial.

  Se ha realizado un código que resuelve este sistema. Utilizando este software, en el Capítulo 3, se presenta un análisis de la dependencia del “gap” con la geometría de la estructura, con la diferencia de constantes dieléctricas y con el factor de llenado de la celda unidad para diferentes tipos de estructuras de una, dos o tres dimensiones. Además, se propone una nueva estructura tridimensional que presenta como ventaja su facilidad de construcción, ofreciendo un “bandgap” completo. Esta estructura se encuentra patentada por el autor y otros investigadores.

- Después del extensivo análisis llevado a cabo en el Capítulo3, los Capítulos 4 y 5 se centran en la utilización de estas estructuras “Photonic Crystal” para evitar la propagación de los modos de substrato en configuraciones de antenas dieléctricas. En el capítulo 4 se ofrece una comparación entre una antena tipo parche sobre un substrato convencional en tecnología microstrip frente a la misma antena pero sobre un substrato de tipo “Photonic Crystal”. Debido al tipo de tecnología empleado, la estructura que se ha utilizado como substrato es periódica en dos dimensiones Se ha comprobado como se ha reducido la potencia del modo de substrato y como repercute esto en la mejora de las características principales de la antena, eficiencia, directividad, diagrama radiación, etc. Se ha estudiado también el acoplo, plano E y plano H, entre dos antenas parches sobre ambos tipos de substrato y se ha podido comprobar como se reduce la energía acoplada de una antena a otra a través de modos de substrato para el caso del substrato “Photonic Crystal”. Con esto se han sentado las bases para aplicaciones de arrays de antenas donde la utilización de este tipo de substratos es muy prometedora.

  Por último, el Capítulo 5, debido al reciente interés de aplicaciones espaciales en el rango de las milimétricas, se muestra el uso de una estructura tridimensional como substrato para una antena dipolo trabajando a frecuencias de milimétricas. Se ha procedido al análisis, diseño y posterior construcción de una estructura tipo “woodpile” a 500 GHz. Las medidas de transmisión bajo incidencia normal para las polarizaciones TE y TM y las simulaciones son muy similares. Posteriormente, se ha simulado el comportamiento de la antena dipolo sobre la estructura comprobándose como se elimina la radiación trasera, como el diagrama de radiación se vuelve más simétrico y como se produce un incremento en la directividad de la antena. En vista de los resultados obtenidos, esta tecnología podría convertirse en una alternativa de futuro para aplicaciones de milimétricas substituyendo en los “front-ends” a las antenas de bocina o a las antenas integradas.

ABSTRACT

The aim of this thesis has been the design of “Photonic Crystal” structures and their application as substrates in dielectric antennas. “Photonic Crystals” defined as periodic structures in one, two or three dimensions, prevent the propagation of an incident electromagnetic wave inside them, over a determined frequency range (bandgap) and for any propagation direction.

Nowadays, one of the main problems in the antenna field is the power transferred to the surface wave modes. This energy does not contribute to the main radiation of the antenna, considering this effect as a loss mechanism. Besides, this energy, depending on the dielectric constant of the substrate and its thickness, could be more than 70% of the total power. Even sometimes, this energy will be added in counter-phase to the main radiation pattern of the antenna making worse this pattern. The main idea is to use the “Photonic Crystal” structures as substrates for these antenna configurations. If this “Photonic Crystal” does not allow the propagation of any electromagnetic wave, the surface wave mode will not be excited and the antenna will radiate all the power. This will lead to an increase of the antenna efficiency and of the antenna directivity, a more symmetric radiation pattern and a reduction of the back radiation of the antenna.

The thesis can be mainly divided into two parts.

- Firstly, the Maxwell’s equations for dielectric periodic structures are presented in Chapter 2. With these equations, an eigensystem has been formulated to solve for the eigenvalues and eigenmodes of any “Photonic Crystal” in one, two and three-dimensions. The solutions offer the dispersion relation of the periodic structure, which characterises completely the behaviour of any infinite “Photonic Crystal”. These dispersion relations provide the information to determine a full or a partial bandgap.

  A code to solve the eigensystem has been implemented. Using this software, the gap behaviour of different “Photonic Crystal” structures as function of the geometry, dielectric constant contrast or fill factor of the unit cell has been analysed in Chapter 3. Besides, a new three-dimensional structure has been proposed which presents the advantage of being easy to fabricate, although up to now, the obtained gaps are rather small. This structure has led to a patent filed by the author and others.

- After the extensive analysis carried out in Chapter 3, Chapter 4 and 5 focus on using “Photonic Crystal” to avoid propagation of surface wave modes in

dielectric antennas configurations, replacing conventional substrates for “Photonic Crystal “ structures. Initially, a two-dimensional configuration is employed in microstrip technology, where a patch antenna is analysed, comparing the conventional substrate features versus the “Photonic Crystal” substrate ones. The analysis reveals a decrease in coupled power to substrate modes and an improvement of efficiency, directivity, back radiation, and pattern symmetry. The mutual coupling, E and H plane, between adjacent patch antennas has also been studied, verifying that the coupling power due to the surface wave mode has been substantially reduced.

Finally, in Chapter 5, another application by the recent interest of space projects at millimetre-waves is the study of a dipole antenna atop a three-dimensional “Photonic Crystal” dielectric structure. A new fabrication method has been devised to fabricate a sample of a woodpile structure for use at 500 GHz. Transmission measurements of this sample for TE and TM polarisations at normal incidence show good agreement when compared with the simulations. If the structure is loaded with a dipole on its top, simulations reveal a highly symmetric main beam with very low back radiation. In view of this performance characteristics one can claim that this new technology could be a good alternative to horn antennas and integrated lenses as front-ends for millimetre-wave applications.

TABLE OF CONTENTS

CHAPTER 1

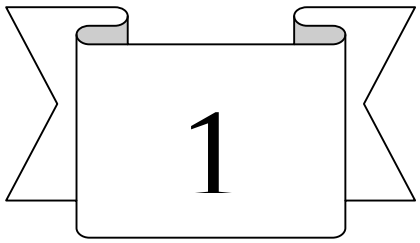

INTRODUCTION

In this introductory Chapter, the main achievements of the research work contained in this dissertation are highlighted. A historical perspective of the works published up to now is offered. In addition, an outline of the structure of this document is given.

1.1 Background

This century has seen substantial advances in semiconductor physics, which have allowed us to tailor the conducting properties of certain materials thereby initiating the transistor revolution in electronics.

Within the last decade there has been a breakthrough in the control of the optical properties of materials opening the path to control the emission and propagation of light [JOA 95]. Many major discoveries in physics in this century originate from the study of waves in periodic structures, examples include X-ray and electron diffraction by crystals, electronic band structure and holography [YAR 97].

Photonic band gap (PBG) materials are a new class of periodic dielectrics, which are the photonic analogues of semiconductors. Electromagnetic waves behave in photonic crystals as electrons behave in semiconductors [YAB 94b and PEN 96]. These artificially engineered periodic materials which control the propagation of electromagnetic waves [DEM 99c] may play an important role in the field of photonics as the laser plays today in optoelectronic systems.

A periodic structure is mainly characterised by three parameters, a spatial period defining the lattice constant, the fractional volume and the dielectric contrast between the constituent materials. Photonic band gap crystals have a further property of gap dimensionality, which is directly related to the number of dimensions of the structure that are periodic. Within these periodic structures the electromagnetic mode distributions and their dispersion relations differ significantly from those of free space. Although one-dimensional photonic crystals have been around for decades in the form of highly reflecting dielectric coatings for mirrors [YAR 97], (also known as Bragg stacks) the idea of making a two- or three-dimensional photonic crystal is only about 10 years old.

Within a one-dimensional periodic structure the electromagnetic dispersion relation has frequency regions in which propagating electromagnetic modes are forbidden. In such forbidden frequency gaps or “Bragg frequencies”, electromagnetic waves attempting to propagate experience evanescent exponential attenuation due to Bragg reflections (Figure 1.1). Although it has been shown that omni-directional reflection can be achieved with a one-dimensional periodicity, this is only true only when the point source of waves is not placed close to the crystal structure [WIN 98, YAB 98 and CHI 99]. By extending the periodicity from one dimension to three dimensions [HO 90, YAB 91, FAN 94, HO 94, SOZ 94, SUZ 95, DEM 99a and FLE 99], it is possible to control the electromagnetic propagation for the entire three-dimensional space. A structure that is periodic in only one dimension will have a one dimensional PBG, while another correctly designed structure that is periodic in all three dimensions can display a fully three-dimensional PBG. The resultant structures are generically called Photonic Crystals, PC.

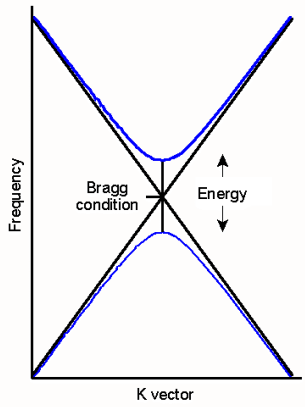

Figure 1.1: Plot showing an example of a dispersion relation and the Bragg condition.

Electromagnetic waves propagating in periodic structures may have discontinuous points or regions in their dispersion relations [BRI 46]. Such discontinuous regions are called “pseudogaps” [RUS 92]. Within a pseudogap, propagating waves can have energies or frequencies only at certain k-points, their existence at the other *k*-points being forbidden. When the forbidden region extends to cover all propagation directions in the dispersion relation then the resultant gap is particularly defined as a complete “bandgap”. A photonic crystal prohibits photon propagation irrespective of the propagation direction [JOA 95].

Since their discovery interest in photonic crystals has grown explosively. The promise of applications using photonic crystals such as highly efficient microwave devices and optical lasers, by significantly improving their efficiency, has spurred the excitement of this new, multidisciplinary field of study. Another exciting application for photonic crystals is as a substrate for antenna configurations [CLE 92, BRO 93 and KES 96].

Photonic Bandgaps (PBG’s) were originally reported in a pair of papers that were published almost simultaneously in 1987. One by Yablonovitch [YAB 87] introduced the forbidden gap for controlling spontaneous and stimulated emission of light. The second by John [JOH 87] introduced gaps to induce Anderson localisation of light waves. However, there was no proof in 1987 that any photonic bandgap could ever be produced experimentally with available refractive indexes. The search for a 3-D photonic bandgap entailed numerous blind alleys and false starts, culminating in 1990 with the remarkable discovery [HO 90] that diamond crystal

geometry was favoured by nature. This led to the first experimental demonstration [YAB 91] of a 3-D photonic bandgap.

Today many more types of electromagnetic crystal structures and designs are being investigated in various dimensions and made of various materials, including metals [SIE 96, POL 97 and SCH 99b]. These metal structures present the advantage of a small size for low operation frequency where RF field can benefit of this fact. In addition to the 3-D photonic crystals, the 2-D photonic crystals are playing an important role. For some applications were a complete gap is not needed, 2-D presents the advantage of the easy fabrication. They appear to be capable of *Q*-factor up to 10.000 in spite of being open structures, they can also confine the light propagation and be used as waveguide by arranging some defects in the crystal [SIG 93, SMI 93, KAR 94, MEA 94, OZB 95, RAR 95, SAK 98 and PAI 99].

There have been ongoing searches for efficient theoretical methods to evaluate dispersion relations in photonic crystals, and, indeed, many theoretical methods have been proposed based on numerical computations. The plane wave method, one powerful and successful method, allows researchers to generate various kinds of eigensystems readily prepared for commercial or public eigensystem package routines. Another method quite often used is the Transfer Matrix Method (TMM) [BEL 95], which allows to calculate the transmission and reflection coefficients through any photonic crystal structure. The combination of both methods characterises completely the behaviour of any PBG structure.

The importance of this new research field is reflected in the increasing number of publications, the special sessions in conferences and also the special journal issues [BOW 92, RAR 95, SOU 95, 1, SCH 99a, SCH 99b and YAN 99]. It should be noted that there is a special WEB site [2] dedicated exclusively to inform about recent publications in the field, the incoming courses, the new software, the conferences and the latest thesis work. The popular journal SCIENCE magazine [3] selected this research field as one of the 10 more important ones in the year 1999and it was also referenced by THE ECONOMIST in the year 1998 [4].

Finally, an example of this new concept can be found in nature [GRA 98]. The wings of the tropical butterfly *Morpho rhetenor* are home to one of the most complicated optical surface known to man. A microscopic lattice of ridges, ribs and struts generates brilliant iridescent colours by a combination of thin-film interference, diffraction and reflection from tiny curved mirrors (see Figure 1.2 and 1.3).

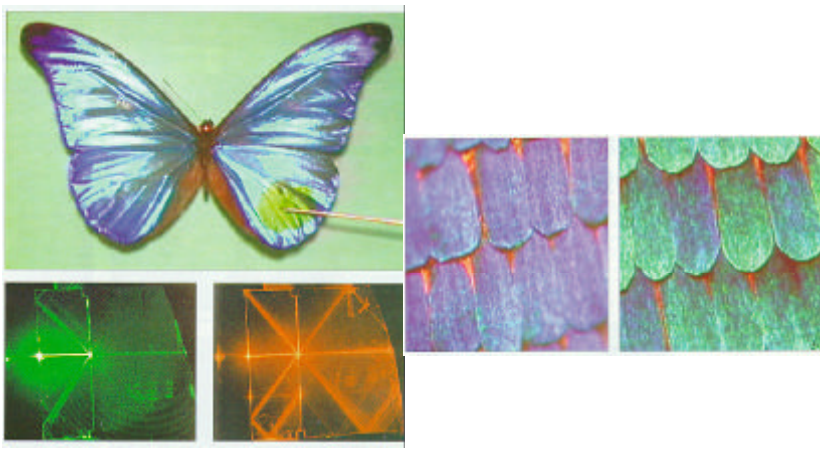

Figure 1.2: Tropical butterflies owe their colours to a mixture of diffraction, interference and reflection by the microscopic texture of their wings' scales [GRA 98].

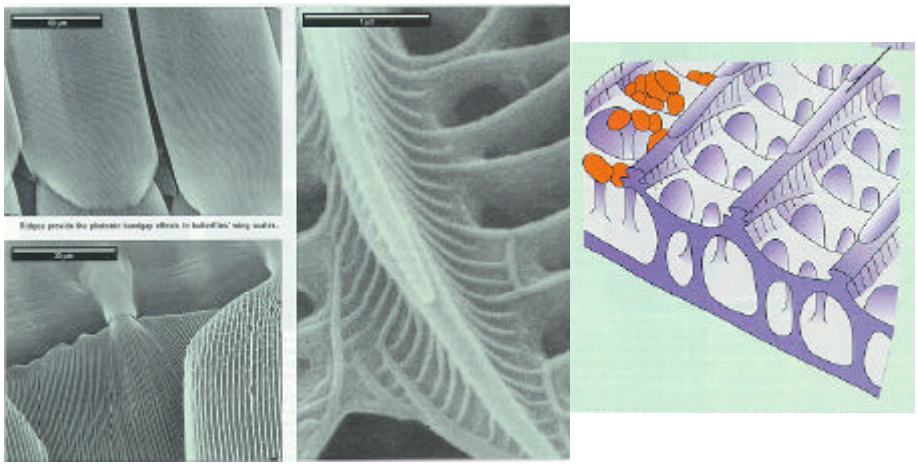

Figure 1.3: Drawings showing the internal structure of the wings. A three-dimensional periodic structure can be observed [GRA 98].

Biologists have known about the surface structure of the insect's wings for decades, but now physicists are performing optical analyses on single scales and attempting to build computer models of what they see. They believe that it is the sub-micrometer details of the structure rather than the chemical pigments that are responsible for the brilliant colours. If this turns out to be true, then the nature has found a way of fabricating sophisticated photonic bandgap (PBG) structures that are more advanced than those that are made in the laboratories.

1.2 Scope of the thesis and survey of its contents

Although most of the research is being performed in the field of optics [YAB 87, YAB 91, BOW 92, LIN 93, YAB 94a, YAB 94b, BAB 95b, KAR 95, SOU 95, KRA 96, KNI 98, PEN 98 SAK 99 and SCH 99a], nowadays, increasing efforts are being directed towards microwave and millimetre wave applications [AGI 94, AGI 96, SCH 99b and YAN 99]. The scalability of this photonic crystal structure makes the fabrication attractive at low frequencies, which allows extrapolating the results to higher frequencies [OZB 94b, OZB 96 and OZB 00]. In addition, one of the most exciting microwave and millimetre wave research fields is centred on antenna applications. This dissertation will be focused on analysing one, two and three-dimensional photonic crystal structures and their use as substrate in antenna configurations.

When an antenna is placed on a high permittivity dielectric substrate, it may couple power into substrate modes. As substrate modes do not contribute to the primary radiation pattern, these modes are a loss mechanism. For example, if the antenna is an elementary dipole, the ratio of the power radiated into the substrate to the power radiated to the air is approximately $e^{3/2}$ [RUT 83]. Thus a dipole on a GaAs substrate $(e = 12.8)$ radiates 46 times more power into the substrate. A second problem is that the power radiated into the substrate at angles greater than $q_c = sin^{-1}e^{-1/2}$ is totally internally reflected at the top and the bottom substrate-air interfaces (see Figure 1.4(a)). For GaAs this occurs at $q_c = 16^o$, so that in many antenna structures the vast majority of the radiated power is trapped in the substrate.

Photonic crystal can offer a real solution to this problem when it is used as antenna substrate (see Figure 1.4(b)). If the driving frequency of the antenna lies within the band gap, no power will be radiated into the substrate at any angle.

Figure 1.4: (a) Cross-sectional view of generic planar antenna on uniform-dielectric substrate. (b) Cross-sectional view of generic planar antenna on a photonic crystal substrate, showing expulsion of radiation at frequencies in the band gap.

Two different applications will be analysed in this dissertation. The first one consists on a 2-D photonic crystal structure for patch antennas in microstrip technology. Initially, a 3-D structure is not needed for this type of application because a ground plane is placed at the bottom of the antenna. Utilised as patch antenna substrates, photonic crystals suppress surface waves that would be otherwise excited in the substrate by the radiating element. Suppression or reduction of surface waves improves antenna efficiency and reduces the side lobe level that is caused by the diffraction of surface waves at the edges of the antenna substrate [KES 96, AGI 99, COL 99, DEM 99b, GON 99d, HOR 99, QUI 99, SCH 99b, YAN 99, GON 00a and GON 00b]. Surface wave diffraction plays a major role when thick substrates are used to increase the bandwidth of the antenna. Power losses due to surface waves can be as high as 70% of the radiated power when thick substrates with high dielectric constant value are used.

With dipole configurations, where the radiation is in every space direction, a 3-D photonic crystal seems to be the preferred structure to be used as substrate [DOW 93, SUZ 95a, SUZ 95c, ELL 96, SIG 96, LEU 97, SIG 97, SIG 99 and SMI 99]. In this case, the photonic crystal acts as some sort of metallic plane reflecting all the power. Improvements in the directivity, in the antenna efficiency and in the beam symmetry have been obtained.

The main contents of this dissertation are organised as follows,

- In Chapter 2 the Maxwell's equations for periodic dielectric structures have been developed. A theoretical tool to calculate the dispersion relations in one, two and three-dimensions has been implemented. The explanation of the main parameters to understand the crystallography concepts employed in this dissertation is presented.

- Chapter 3 presents an extensive study of one, two and three-dimensional photonic crystals. Some explanation about the origin of the gap is given. A complete study about the behaviour of the two-dimensional square and a triangular-hexagonal lattice has been performed. The gap width as a function of the fill factor and the dielectric constant has been analysed. Two three-dimensional structures are also analysed: the layer by layer or woodpile photonic crystal, and a new structure, which exhibits a complete gap and is very easy to manufacture.

- In Chapter 4, the use of a square lattice of holes in a dielectric medium is proposed as substrate for patch antennas. A comparison between a conventional

patch antenna and a photonic crystal antenna has been performed. Different cases have been analysed for different rows of drilled holes. Improvements in the main radiation parameters have been reported. The mutual coupling between antennas has also been studied, indicating that this technology reduces the surface wave mode propagation while minimising the coupling between antennas in an array configuration and improving the radiation parameters.

- In Chapter 5 the design, analysis, fabrication and measurements of a three-dimensional photonic crystal working at 500 GHz is presented. A new fabrication method has been proposed. The measurements are in agreement with the calculations. The theoretical radiation patterns of a dipole on top of this structure are also presented. An increase in the directivity, a reduction in the back radiation and a high symmetry beam has been obtained.

- Finally, the main conclusions of this work, and an outline of the future research to be done in this field are described in Chapter 6.

At point and before going through the dissertation, some words about the Photonic Band Gap terminology should be pointed out. The microwave field has utilised *1-D periodic structures* in many different applications and an extensive and sophisticated periodic-structure theory has been developed over the past 50 or more years in connection with these applications. Within the past few years a new terminology has been introduced into the microwave field: photonic band gap. This terminology comes from the photonics field, where stop bands are called band gaps and periodic structures are called photonic-band-gap structures. This new terminology is now creeping into the microwave field. However, there are people in the microwave community that disagree with this terminology and are prompting to reject it [OLI 99] and [OLI 00]. Due to this, in the whole dissertation to follow, the terminology used to define these periodic structures has been chosen to be "*Photonic Crystal*" structures. The term "Photonic Crystal" expresses the structure that undergoes the general 3-D effect of Bragg diffraction when X-rays excited.

CHAPTER 2

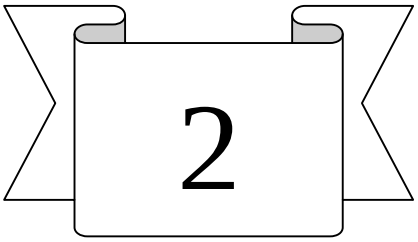

CRYSTAL STRUCTURES AND ELECTROMAGNETIC FIELDS IN PHOTONIC CRYSTALS

In this Chapter, the main parameters, which describe a Crystal structure will be defined. Their understanding is quite important to the study of the Photonic Crystal structures performed in the next Chapter. In addition, the plane wave expansion method to solve Maxwell's equations in periodic dielectric structures is developed. Maxwell's equations are transformed into sets of matrix equations and eigensystems. By solving the eigensystems the behaviour of a one-two or three-dimensional Photonic Crystal is completely characterised.

2.1 Crystal Structures

Ideal Photonic Crystals are made of an infinite number of arbitrarily shaped scatters forming either one, two or three dimensional periodic lattices designed to influence the behaviour of photons in much the same way that the crystal structure of a semiconductor affects the properties of electrons. A unit cell of such a Photonic Crystal is illustrated in Figure 2.1. The scatters usually consist of dielectric materials: but can be conductive, absorptive or active materials such as semiconductor or metals. Each Photonic Crystal can generate a characteristic photonic bandgap structure because of interactions between coherent scattering from lattice structures and scattering from individual scatters. Photonic Crystal are characterised by the following independent variables:

- Lattice Structure (lattice constant (a))
- Shape of the individual scatters
- Fill factor: ratio between volume of scatters in the unit cell and the total volume of the unit cell.
- Dielectric constants of the constituent materials
- Dielectric contrast.

These variables must be properly chosen in order to generate desirable band gaps in the dispersion relation diagrams.

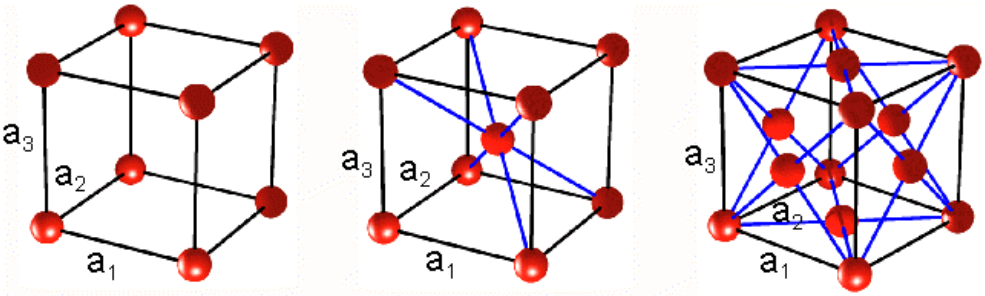

Figure 2.1: Different lattice structures. Simple Cubic structure at the left, Body Centred Cubic in the middle, and Face Centred Cubic at the right.

In the following sections, a brief summary on the different parameters (primitive lattice, reciprocal lattice and Brillouin Zone) to define a Crystal structure is presented.

The understanding of these parameters is important for the understanding of the following Chapters, because most of the theory is based on them.

2.1.1 Primitive lattice cell

In this section, a brief explanation, about how to obtain the primitive lattice vectors for any two or three-dimensional structure, is given. Once these vectors are known, the periodic structure will be completely defined in the real space.

The structure of all crystals can be described in terms of lattice vectors, with a group of scatters attached to every lattice point called the basis of the lattice. The basis is repeated in space to form the crystalline structure. The basis consists of a primitive cell, arranging one cell at each lattice point will fill up the entire crystal without leaving undefined voids or overlapping regions. The Bravais lattice vectors describe how these repeating units in a crystal are tiled. A Bravais lattice can be defined as all points with positions:

$$\vec{R} = n_1\vec{a}_1 + n_2\vec{a}_2 + n_3\vec{a}_3 \tag{2.1}$$

where $\vec{a}_i$ are not in the same plane, and n_i are integers. The $\vec{a}_i$ vectors are called the primitive vectors and there are many possible choices of these vectors (see Figure 2.2). The Wigner-Seitz cell [BRI 46] is the most common choice for the primitive unit cell. This defines a region of space that is closer to a particular point than to any other point on a Bravais lattice.

This Wigner-Seitz cell can be constructed following this procedure (see Figure 2.3):

- Draw lines to connect a given lattice point to all nearby lattice points.
- At the midpoint and normal to these lines, draw new lines or planes.
- The smallest volume enclosed in this way is the Wigner-Seitz primitive cell.

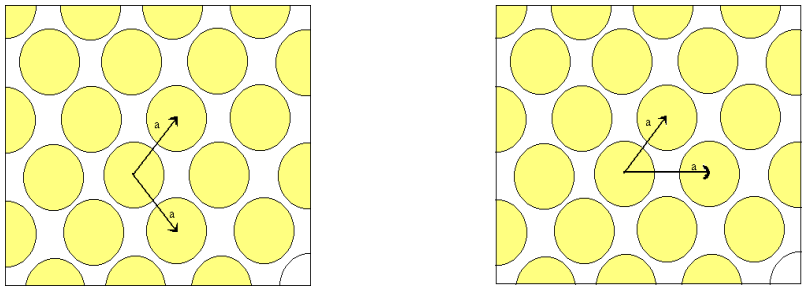

Figure 2.2: Different choices for the primitive vectors in a two-dimensional structure of triangular columns.

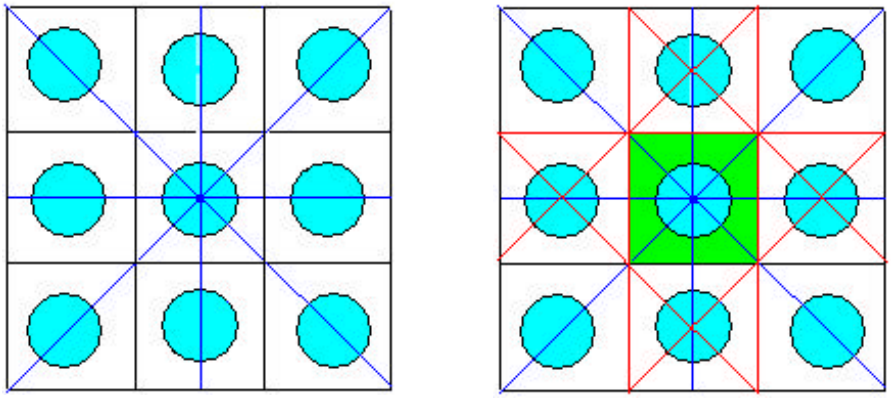

Figure 2.3: Procedure to obtain the Wigner-Seitz primitive cell. (a) Lines (blue colour) connecting the nearby lattice points. (b) Lines (red colour) normal to the previous lines at the midpoint and the Wigner-Seitz cell (green colour).

2.1.2 Reciprocal Lattice

The reciprocal lattice is a Bravais lattice itself, but it is defined in the wavevector $\vec{k}$ space. The reciprocal lattice can be defined as all $\vec{k}$ that satisfy:

$$\vec{k} = m_1\vec{b}_1 + m_2\vec{b}_2 + m_3\vec{b}_3 \tag{2.2}$$

where m_i are integers and $\vec{b}_i$ are the reciprocal vectors. The $\vec{b}_i$ vectors are generated by satisfying the following relation:

$$\vec{R}\cdot\vec{k} = (n_1\cdot\vec{a}_1 + n_2\cdot\vec{a}_2 + n_3\cdot\vec{a}_3)\cdot(m_1\cdot\vec{b}_1 + m_2\cdot\vec{b}_2 + m_3\cdot\vec{b}_3) = N\cdot 2\cdot p \tag{2.3}$$

For all choices of n_i *and* m_i, the above condition must hold for some N (integer). This condition is satisfied if the $\vec{b}_i$ are chosen such that $\vec{a}_i\cdot\vec{b}_j = 2\cdot p\cdot d_{ij}$. In this way the primitive reciprocal lattice vectors are obtained:

$$\vec{b}_1 = 2\cdot p\frac{\vec{a}_2\times\vec{a}_3}{\vec{a}_1\cdot(\vec{a}_2\times\vec{a}_3)} \tag{2.4}$$

$$\vec{b}_2 = 2\cdot p\frac{\vec{a}_3\times\vec{a}_1}{\vec{a}_1\cdot(\vec{a}_2\times\vec{a}_3)} \tag{2.5}$$

$$\vec{b}_3 = 2 \cdot p \frac{\vec{a}_1 \times \vec{a}_2}{\vec{a}_1 \cdot (\vec{a}_2 \times \vec{a}_3)} \tag{2.6}$$

Therefore, when the Fourier transform of a function that is periodic on a lattice is required it is only necessary to include terms with wave vectors that are reciprocal lattice vectors. The Wigner-Seitz cell of the reciprocal lattice is called the First Brillouin zone.

2.1.3 The Brillouin zone

The study of waves in periodic structures makes use of a single physical principle proposed by Floquet in 1884. The principle states that normal modes in periodic structures can be expressed as a superposition of a set of plane waves whose wavevectors are related by: $\vec{k}_n = \vec{k}_0 + n\vec{G}$, where $\vec{k}_0$ is the initial arbitrary wavevector, $\vec{k}_n$ is the wavevector of the nth mode and $\vec{G}$ is the reciprocal lattice vector [RUS 86]. Later extension of the theorem by Bloch covered multidimensional periodic structures in his treatment of electrons in a crystal and is referred to as the Bloch expansion. The modes $H_k(r)$ can be written in the Bloch form [JOA 95] as:

$$H_k(r) = e^{ikr} u_k(r) = e^{ikr} u_k(r + R) \tag{2.7}$$

Bloch modes have a fundamentally important feature: different values of k do not necessarily lead to different modes. Specifically, a mode with wave vector $\vec{k}$ and a mode with wave vector $(\vec{k} + \vec{G})$ are the same mode, if $\vec{G}$ is a reciprocal lattice vector.

Consequently there is redundancy in the label k and the attention can be restricted to a finite zone in reciprocal space. Within this zone it is not possible to translate from one part of the volume to another through the addition any reciprocal lattice vector $\vec{G}$. Values of k that lie outside of this zone can be reached from within the zone by adding $\vec{G}$, and are therefore redundant labels. This zone is the Brillouin zone.

The smallest region within the Brillouin zone for which the k directions are not related by symmetry is called the *Irreducible* Brillouin zone. For example a Photonic Crystal with the symmetry of a simple square lattice has a square Brillouin zone centred at $k=0$, as depicted in Figure 2.4. The *Irreducible* zone is a

triangular wedge with 1/8 the area of the full Brillouin zone defined by [JOA 95] the Γ, X, M points (this definition is used in the Crystallography field); the rest of the Brillouin zone contains redundant copies of the irreducible zone.

2.2 Electromagnetic fields in Photonic Crystals

In this section, the plane wave expansion method, a numerical computational method to solve Maxwell's equations (full-vector wave equations) with periodic dielectric functions, will be described. By applying the plane wave expansion, Maxwell's equations are conveniently transformed into a set of matrix equations and eigensystems. This section mainly focuses on computations of periodic propagating electromagnetic modes (propagating modes) in non-conducting loss-less passive dielectric Photonic Crystals.

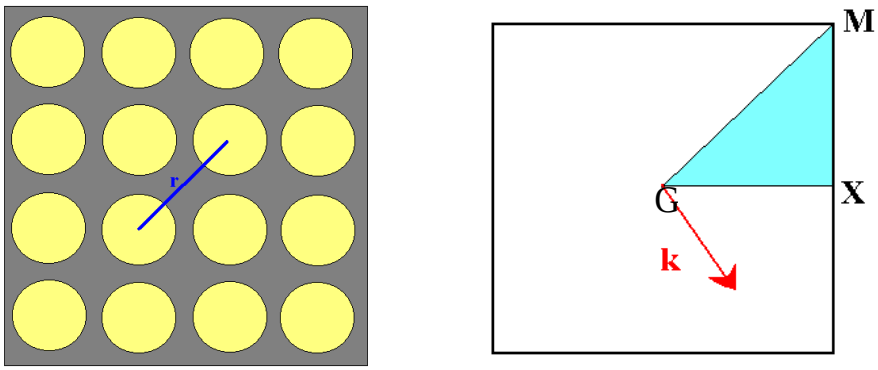

Figure 2.4: Left: A Photonic Crystal made using a square lattice. Right: The corresponding Brillouin zone of the square lattice. The Irreducible zone is plotted in blue colour.

2.2.1 Introduction

There is an active investigation into efficient theoretical methods to evaluate dispersion relations in Photonic Crystals and many theoretical methods have been proposed based on numerical computations [MEA 93b and BEL 95].

Because Maxwell's equations for linear dielectric materials are basically exact, computation has played a critical role in the analysis of Photonic Crystals. All these calculations involved the expansion of the electromagnetic fields in a basis of plane waves. The reason for this is that the plane waves are complete, can

be systematically improved and do not require any prior knowledge as the distributions of the fields. However, it is necessary to be careful because for some cases the accuracy of the method can be limited, suffering from poor plane-wave convergence [SOZ 92]. This can happen when defects are introduced in the calculations. In this section, a complete matrix representation of the Maxwell's equations valid for one, two and three-dimensional structures, has been developed by using the plane wave method.

The plane wave method, a powerful and successful method in the photonic band theory, generates various kinds of eigensystems readily compatible with commercial or public eigensystem solution package routines. The matrix equations and eigensystems formulated here are entirely based in Cartesian coordinates and are readily extendible to describe more general Photonic Crystals with conductive, absorptive or active media. The mathematical developments presented subsequently are based on [KWE 95]

2.2.2 Theory – Complete representation by the plane wave method

All of the macroscopic electromagnetism, including the propagation of light in a Photonic Crystal, is governed by the four macroscopic Maxwell equations. In MKS units, they are:

$$\nabla \cdot \vec{B} = 0 \tag{2.8}$$

$$\nabla \cdot \vec{D} = r \tag{2.9}$$

$$\nabla \times \vec{E} = -\frac{\partial}{\partial t}\vec{B} \tag{2.10}$$

$$\nabla \times \vec{H} = \frac{\partial}{\partial t}\vec{D} + \vec{J} \tag{2.11}$$

where $\vec{E}$ and $\vec{H}$ are the macroscopic electric and magnetic fields, $\vec{D}$ and $\vec{B}$ are the displacement and magnetic induction fields, and r and $\vec{J}$ are the free charges and currents.

The propagation conditi on will be restricted to a mixed dielectric medium, a composite of regions of homogeneous dielectric material, with no free currents or charges. In a medium with these features, the light can be propagated but $r = \vec{J} = 0$.

In the medium i n which the equations will be solved, it will be assumed that the material is macroscopic and isotropic, so, $\vec{E}(r,w)$ and $\vec{D}(r,w)$ are related by a scalar dielectric constant $e(r,w)$. Besides, the dependence of the dielectric constant with frequency will be ignored. Even more, $e(r)$ will be taken as real, this means a low-loss dielectric.

Using the ratio $\vec{D}(r) = e(r)\vec{E}(r)$ and taking into account that the relative magnetic permeability is very close to unity, the Maxwell's equation can now be written as:

$$\nabla \cdot \vec{H}(r,t) = 0 \tag{2.12}$$

$$\nabla \cdot e(r) \cdot \vec{E}(r,t) = 0 \tag{2.13}$$

$$\nabla \times \vec{E}(r,t) = -\frac{\partial}{\partial t}\vec{B} \tag{2.14}$$

$$\nabla \times \vec{H}(r,t) = \frac{\partial}{\partial t} e(r) \cdot \vec{E}(r,t) \tag{2.15}$$

The equations have be en restricted to linear and loss-less materials. Photonic Crystals made from non-linear dielectrics are certainly of great interest and deserve a separate investigation, which will not be the subject of this dissertation.

The above equations will be used to obtain the eigenvalues and eigenvectors, which define the behaviour of an infinite Photonic Crystal.

First of all, equation 2.15 can be written in the following way:

$$h(r) \cdot \nabla \times \vec{H} = e_0 \frac{\P\vec{E}}{\P t} \tag{2.16}$$

where

$$h(r) = \frac{1}{e_r(r)} \tag{2.17}$$

Introducing equation 2.16 into equation 2.14, the next expression is obtained

$$\nabla \times \left[h(r) \cdot \nabla \times \vec{H} \right] = -\frac{1}{c^2} \frac{\P^2 \vec{H}}{\P t^2} \tag{2.18}$$

Since the relative electric permitivity is a periodic function of position, the magnetic field should satisfy Bloch's theorem and also be divergence-free $(\nabla \cdot \vec{H} = 0)$; this is important to imply the *transverse* condition, which requires that if $\vec{H}(r) = \vec{a} \cdot \exp(i\vec{k} \cdot \vec{r})$, $\vec{a} \cdot \vec{k} = 0$. With all these requirements, the magnetic field can be expanded in a plane wave basis [KWE 95] as follows:

$$\vec{H}(r,t) = \sum_n \int_\Omega dk \cdot \vec{H}_{n,k}(r,t)$$

$$= \sum_n \int_\Omega dk \cdot f_{n,k} \sum_G \sum_{i=1}^{2} h_{n,k}(k+G) \cdot \hat{e}_i(k+G) \cdot \exp\left[j(\vec{k} + \vec{G}) \cdot \vec{r} - jw_{n,k} t \right] \tag{2.19}$$

where *n* is the mode index or the Bloch mode index, $\vec{k}$ is the wavevector in the first Brillouin zone, $\vec{G}$ is the reciprocal lattice vector, $\omega_{n,k}$ is the angular frequency corresponding to the given wavevector, *i* is the polarisation index, and $\hat{e}_1(k+G)$ and $\hat{e}_2(k+G)$ are polarisation unit vectors such that $\left\{ \hat{e}_1(k+G), \hat{e}_2(k+G), (k+G)/|k+G| \right\}$ form a right-handed triad. The factor $f_{n,k}$ is an expansion coefficient of an arbitrary magnetic field in terms of the eigensolutions. The parameter Ω represents all the k-space and $h_{n,k}$ is the eigenvector value for each plane wave in each direction of propagation.

In this development, the set of polarisation unit vectors is chosen in such a way as given below:

$$\begin{aligned} \hat{e}_1(-k-G) &= \hat{e}_1(k+G) \\ \hat{e}_2(-k-G) &= -\hat{e}_2(k+G) \end{aligned} \tag{2.20}$$

For example, the set of polarisation unit vectors can be chosen in the following way to satisfy the previous condition:

$$\begin{aligned} \hat{k} + \hat{G} &\equiv |k+G| \cdot (\sin q \cos f, \sin q \sin f, \cos q) \\ \hat{e}_2(k+G) &\equiv -\hat{x} \sin f + \hat{y} \cos f \propto \hat{z} \times (\hat{k} + \hat{G}) \end{aligned} \tag{2.21}$$

When $\hat{z}$ and $(\hat{k}+\hat{G})$ are parallel to each other, f can be set as an arbitrary value, for example $f=-p/2$, then $\hat{e}_2(k+G)=\hat{x}$. Then $\hat{e}_1(k+G)$ is determined uniquely:

$$\hat{e}_1(k+G)\equiv\hat{e}_2(k+G)\times\frac{\hat{k}+\hat{G}}{|k+G|}=\hat{x}\cos q\cos f+\hat{y}\cos q\sin f-\hat{z}\sin q \quad (2.22)$$

It is easy to prove that

$$\hat{e}_1(k+G)\times\hat{e}_2(k+G)=\frac{\hat{k}+\hat{G}}{|k+G|} \quad (2.23)$$

From the definition of the polarisation unit vectors, it is clear that the condition (equation 2.20) is satisfied.

Obviously, the selection of a set of polarisation unit vectors is not unique, and any other convenient definition can be given.

Defining the following relation,

$$\hat{v}=\frac{\hat{k}+\hat{G}}{|k+G|} \quad (2.24)$$

the vector components used in the computer code were fixed as follows,

$$\sin q=\sqrt{\hat{v}_x^2+\hat{v}_y^2} \quad (2.25)$$

$$\cos q=-\hat{v}_z \quad (2.26)$$

$$\sin f=\frac{\hat{v}_y}{\sqrt{\hat{v}_x^2+\hat{v}_y^2}} \quad (2.27)$$

$$\cos f=\frac{\hat{v}_x}{\sqrt{\hat{v}_x^2+\hat{v}_y^2}} \quad (2.28)$$

From the definition of the $\vec{H}$ field, an equation describing the electric field behaviour can be obtained as,

$$\vec{E} = -\frac{h(r)}{e_0}\sum_n \int_\Omega dk \cdot \frac{f_{n,k}}{w_{n,k}} \sum_G \sum_{i=1}^{2} h_{n,k}(k+G)\cdot(\vec{k}+\vec{G})\times\hat{e}_i(k+G)\cdot$$
$$\cdot\exp\left[j(\vec{k}+\vec{G})\cdot\vec{r} - jw_{n,k}t\right] \tag{2.29}$$

Since $e_r(r)$ is a periodic function of position, $h(r)$ can be Fourier expanded as follows:

$$h(r) = \sum_G h_G e^{i\vec{G}\cdot\vec{r}} \tag{2.30}$$

$$h_G = \frac{1}{V_0}\int_{V_0} dr \cdot h(r)\cdot e^{-i\vec{G}\cdot\vec{r}} \tag{2.31}$$

where V_0 is the volume of the Wigner-Seitz cell. It is assumed that the first Brillouin zone has inversion symmetry, then each wavevector and its inversion belong to the same Brillouin zone. Because of this, the Wigner-Seitz cell has inversion symmetry, i.e. $h(-r) = h(r)$ [BRI 46].

Using this expansion, the electric field can be written in a form in which the positional dependencies appear only in the exponent of the plane-wave-type exponential term. This set of electromagnetic fields automatically satisfies all the Maxwell equations except the Faraday's law. Imposition of Faraday's law (equation 2.14) on the electric and magnetic fields results in the dispersion relation:

$$\nabla\times\vec{E} = -\frac{i}{e_0}\sum_n \int_\Omega dk \frac{f_{n,k}}{w_{n,k}} \sum_G \sum_{G'} \sum_{i=1}^{2} h_{n,k}(k+G')h_{G-G'}(\vec{k}+\vec{G})\times\left[\left(\vec{k}+\vec{G}'\right)\times\hat{e}_i(k+G')\right]$$
$$\cdot\exp\left[j(\vec{k}+\vec{G})\cdot\vec{r} - jw_{n,k}t\right] = im_0\sum_n \int_\Omega dk\cdot f_{n,k}\cdot w_{n,k}\sum_G\sum_{i=1}^{2} h_{n,k}(k+G)\cdot\hat{e}_i(k+G)$$
$$\cdot\exp\left[j(\vec{k}+\vec{G})\cdot\vec{r} - jw_{n,k}t\right] \tag{2.32}$$

Note that $\nabla\times\vec{E} = (\vec{k}+\vec{G})\times\vec{E}$.

Since the relation must hold for each n mode and for all space directions, the following condition must also hold [KWE 95]:

$$\sum_{G'}\sum_{i=1}^{2} h_{n,k}(k+G')h_{G-G'}(\vec{k}+\vec{G})\times\left[(\vec{k}+\vec{G}')\times\hat{e}_i(k+G')\right]=$$

$$=-\frac{w^{2}_{n,k}}{c^{2}}\sum_{i=1}^{2} h_{n,k}(k+G)\cdot\hat{e}_i(k+G) \tag{2.33}$$

Since a linear polarisation basis is assumed, the following relation is obtained:

$$\hat{e}_i(k+G)\cdot\hat{e}_{i'}(k+G)=\delta_{i,i'} \tag{2.34}$$

Taking the scalar product in the eq uation 2.33 with a polarisation eigenvector results in

$$\sum_{G'}\sum_{i=1}^{2} h_{n,k}(k+G')h_{G-G'}\hat{e}_{i'}(k+G)\cdot\left\{(\vec{k}+\vec{G})\times\left[(\vec{k}+\vec{G}')\times\hat{e}_i(k+G')\right]\right\}=$$

$$=-\frac{w^{2}_{n,k}}{c^{2}}h_{n,i'}(k+G) \tag{2.35}$$

Recalling that $\left\{\hat{e}_1(k+G),\hat{e}_2(k+G),(\hat{k}+\hat{G})/|k+G|\right\}$ forms a right-handed triad,

$$\begin{aligned}(\hat{k}+\hat{G})\times\hat{e}_1(k+G)&=|k+G|\cdot\hat{e}_2(k+G)\\(\hat{k}+\hat{G})\times\hat{e}_2(k+G)&=-|k+G|\cdot\hat{e}_1(k+G)\end{aligned} \tag{2.36}$$

With the use of well-kno wn vector identities, the following relation is obtained:

$$\begin{aligned}&\sum_{G'}|k+G||k+G'|h_{G-G'}\left[-\hat{e}_2(k+G)\cdot\hat{e}_2(k+G')h_{n,1}(k+G')+\right.\\&\left.+\hat{e}_2(k+G)\cdot\hat{e}_1(k+G')h_{n,2}(k+G')\right]=-\frac{w^{2}_{n,k}}{c^{2}}h_{n,1}(k+G)\end{aligned} \tag{2.37}$$

A similar result for $i'=2$ can be obtained and both expressions can be put into a matrix form:

$$\sum_{G'} |k+G\|k+G'|h_{G-G'} \begin{bmatrix} \hat{e}_2(k+G)\cdot\hat{e}_2(k+G') & -\hat{e}_2(k+G)\cdot\hat{e}_1(k+G') \\ -\hat{e}_1(k+G)\cdot\hat{e}_2(k+G') & -\hat{e}_1(k+G)\cdot\hat{e}_1(k+G') \end{bmatrix}$$
$$\begin{pmatrix} h_{n,1}(k+G') \\ h_{n,2}(k+G') \end{pmatrix} = \frac{w^2{}_{n,k}}{c^2} \begin{pmatrix} h_{n,1}(k+G) \\ h_{n,2}(k+G) \end{pmatrix} \tag{2.38}$$

This result leads to a standard matrix diagonalisation problem for the eigenvectors and eigenvalues. Assuming that $w^2_{n,k,s}/c^2$ for s=1,2 are the eigenvalues of equation 2.38 corresponding to a given energy band *n* with wavevector *k*, and the corresponding eigenvectors denoted by

$$[h(n,k,s)] = \begin{pmatrix} h^{(s)}_{n,1}(k+G_1) \\ h^{(s)}_{n,2}(k+G_1) \\ h^{(s)}_{n,1}(k+G_2) \\ \cdot \\ \cdot \\ \cdot \end{pmatrix} \tag{2.39}$$

As result of the diagonalisation, the eigenvectors with different indices are orthogonal to each other (e.g. TE and TM modes in a 2-dimensional structure):

$$[h(n,k,s)]^+[h(n,k,s')] = \sum_G \sum_{i=1}^{2} h^{(s)*}_{n,i}(k+G)h^{(s')}_{n,i}(k+G) = \delta_{s,s'} \tag{2.40}$$

It can be proven [KWE 95] that the general equation 2.38 satisfies the following conditions:

$$\frac{w^2{}_{n,k,s}}{c^2} = \frac{w^2{}_{n,-k,s}}{c^2} \tag{2.41}$$
$$h^{(s)}_{n,1}(-k-G) = h^{(s)}_{n,1}(k+G) \tag{2.42}$$
$$h^{(s)}_{n,2}(-k-G) = h^{(s)}_{n,2}(k+G) \tag{2.43}$$

Note that the matrix in equation. 2.38 is real, and that the eigenvalue is also real because it is the eigenvalue of a hermitian operator. [JOA 95 and KWE 95] Therefore, equation 2.39 is an eigenvector of a real matrix with a real eigenvalue. Then the eigenvector itself can be made real, if it is not already real. For example,

if a complex vector is an eigenvector of the matrix, then its complex conjugate is also an eigenvector of the same matrix with the same real eigenvalue. By adding the two, a real eigenvector with the original value is obtained. Therefore, it will be assumed that the eigenvectors are real:

$$h_{n,i}^{(s)*}(k+G) = h_{n,i}^{(s)}(k+G) \tag{2.44}$$

In this new basis set, the magnetic field can be written as

$$\vec{H}(r,t) \equiv \sum_n \int_\Omega dk \sum_s \vec{H}_{n,k,s}(r,t) = \vec{H}^+(r,t) + \vec{H}^-(r,t) =$$
$$\sum_n \int_\Omega dk \sum_s f_{n,k,s} \vec{H}^+_{n,k,s}(r,t) + \sum_n \int_\Omega dk \sum_s f^*_{n,k,s} \vec{H}^-_{n,k,s}(r,t) \tag{2.45}$$

where + and – means forward and reflected propagation direction respectively,

$$\vec{H}^+_{n,k,s}(r,t) \equiv \left[\vec{H}^-_{n,k,s}(r,t)\right]^* = \sum_G \sum_{i=1}^{2} h_{n,i}^{(s)}(k+G) \cdot \hat{e}_i(k+G) \cdot$$
$$\cdot \exp\left[j(\vec{k}+\vec{G}) \cdot \vec{r} - jw_{n,k,s}t\right] \tag{2.46}$$

It is important to notice that solving the previous equations does not take into account the edge effect, because an infinite structure in all directions is supposed.

Since, the relative dielectric permitivity is purely real, and the system to solve (equation 2.38) is a hermitian eigenvalue problem and therefore the eigenvalues should be real and the eigenvectors with different eigenvalues should be orthogonal to each other,

$$\int dr \vec{H}_{n,k,s}(r,t) \cdot \vec{H}^*_{m,k',s'}(r,t) = C_{n,k,s}\, d_{n,m}\, d(k-k')\, d_{s,s'} +$$
$$+ C'_{n,k,s}\, d_{n,m}\, d(k+k')\, d_{s,s'} \tag{2.47}$$

where equation 2.41 has been used and the $C_{n,k,s}$ and $C'_{n,k,s}$ are multiplicative constants.

After algebraic manipulations from this equation [KWE 95], the following conclusion can be extracted,

$$\sum_G \sum_i h_{n,i}^{(s)}(k+G) \cdot h_{m,i}^{(s')}(k+G) = d_{n,m}\, d_{s,s'} \tag{2.48}$$

Although this equation should be arbitrary within a multiplicative constant, the vectors could be normalised so that $f_{n,k,s}$ absorbs all the scalar components.

The set of $\vec{H}_{n,k,s}(r,t)$ constitutes a complete set in the sense that an arbitrary continuous magnetic field satisfying the required Bloch theorem can be expanded in terms of $\vec{H}_{n,k,s}(r,t)$. Then since the electric field and magnetic field are related by Maxwell's equations, the set of $\vec{E}_{n,k,s}(r,t)$ also should be complete.

Using the equation 2.15 the electric field can be derived and expanded as,

$$\vec{E}^{+}(r,t) = \sum_n \int_\Omega dk \sum_s C_{n,k,s} \sum_G \sum_{G'} \sum_i h_{n,i}^{(s)}(k+G') h_{G-G'}(\vec{k}+\vec{G}') \times \hat{e}_i(k+G') \cdot \cdot \exp\left[j(\vec{k}+\vec{G}) \cdot \vec{r} - j w_{n,k,s} t \right] \tag{2.49}$$

Finally, note that all this theoretical development has been done for the magnetic field, and not for the electric field. Nevertheless, a similar procedure could have been followed beginning with the equation 2.15 in order to get an eigensystem with the eigenvalues and eigenvector for the electric field. This has not been done because the resulting general equation for the electric field is not an Ordinary Hermitian System but a Generalised Hermitian system, which is a far more difficult task to solve using the direct traditional method.

Since the final system to solve is Hermitian, a special kind of routines can be used to obtain the eigenvalues and eigenvectors. These routines allow the possibility of solving only for the lowest eigenvalues and eigenvectors reducing the required computational time.

It should be noted that another source of inaccuracies is coming from the representation of the dielectric function. Because the true dielectric function $e(r)$ is piecewise constant, the FFT grid is poor to describe the boundary between dielectrics. There are different techniques to minimise this effect , all of them are based on the smoothing of the dielectric constant values around the boundaries [MEA 93b]. The method used for the calculations in this dissertation is based on performing a weighted average of the inverses of the dielectric constants.

2.2.3 Electromagnetic Energy

Although the harmonic modes in a periodic dielectric medium can be quite complicated, there is a simple way to understand some of their qualitative features. Roughly, a mode tends to concentrate its displacement energy in regions of high dielectric constant, while remaining orthogonal to the modes below it in frequency. This intuitive notion finds expression in the *electromagnetic variational theorem* [JOA 95]. The lowest frequency mode is the field pattern that minimises the electromagnetic energy functional:

$$E_f(H) = \frac{1}{2}\frac{(H, \Theta H)}{(H, H)} \tag{2.50}$$

where

$$(H, \Theta H) = \int_V \left[\nabla \times \left(\frac{1}{e(r)} \nabla \vec{H}(r)\right)\right] \vec{H}^*(r)\, dV \tag{2.51}$$

$$(H, H) = \int_V \vec{H}(r)\vec{H}^*(r)\, dV \tag{2.52}$$

Using the following vector identity:

$$B \cdot \nabla \times A = \nabla A \times B + A \nabla \times B \tag{2.53}$$

and using the following relations,

$$\begin{aligned} \vec{A} &= \nabla \times \vec{H}(r) \\ \vec{B} &= \vec{H}(r) \end{aligned} \tag{2.54}$$

the electromagnetic energy functional can be written as;

$$\begin{aligned} E_f(H) &= \left(\frac{1}{2(H, H)}\right) \int_V \frac{1}{e(r)} \left|\nabla \times H(r)\right|^2 dV \\ &= \left(\frac{1}{2(H, H)}\right) \int_V \frac{1}{e(r)} \left|\frac{w}{c} \vec{D}(r)\right|^2 dV \end{aligned} \tag{2.55}$$

From this expression, $\vec{E}_f(H)$ will be minimised when the displacement field $\vec{D}$ is concentrated in the regions of high dielectric constant.

2.2.4 Scaling Properties of the Maxwell Equations

One interesting feature of electromagnetism in dielectric media is that there is no fundamental length scale other than the assumption that the system is macroscopic.

To probe the scaling properties [JOA 95], an analysis about what is happening in the equation 2.18 when the dielectric constant is compressed or expanded will be performed. In fact, if $e'(r) = e(r/s)$ for some scalar parameter s. The equation 2.18 can be rewritten using $r' = sr$ and $\nabla' = \nabla / s$ as,

$$s\nabla' \times \left(\frac{1}{e(r'/s)} s\nabla' \times \vec{H}(r'/s) \right) = \left(\frac{w}{c} \right)^2 \vec{H}(r'/s) \tag{2.56}$$

But $e(r'/s)$ is none other than $e'(r')$. Dividing out the s's shows that

$$\nabla' \times \left(\frac{1}{e'(r')} \nabla' \times \vec{H}(r'/s) \right) = \left(\frac{w}{cs} \right)^2 \vec{H}(r'/s) \tag{2.57}$$

But this is just the equation 2.18 again, this time with mode profile $H'(r') = H(r'/s)$ and frequency $w' = w/s$. As conclusion it can be said that the solution of the problem at one length scale determines the solution at all other length scales.

This simple fact is of outstanding practical importance. The fabrication of complex micron-scale Photonic Crystals can be quite difficult. Nevertheless, models can be easily made and tested in the microwave regime, at the much larger length scale of centimetres. The result of this section guarantees that the model will have the same electromagnetic properties.

CHAPTER 3

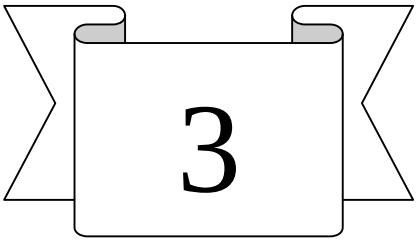

MODELLING OF PHOTONIC CRYSTAL STRUCTURES

The previous chapter dealt with the electromagnetic fields in Photonic Crystals. The theoretical basis to analyse the behaviour of periodic structures in one, two or three-dimensions has been developed. In this chapter, different periodic structures configurations will be studied. As working rule, one-dimensional structures exhibit a complete band gap for one propagation direction, which coincides with the periodicity direction in the Photonic Crystal. Two-dimensional structures have the band gap in the plane of periodicity and three-dimensional ones present a complete gap for any direction of propagation. These assumptions are not always true: one-dimensional structures show sometimes a complete bandgap.

As starting point, the one-dimensional Photonic Crystal will be used to introduce more easily the understanding of the features of the Photonic Crystals. After that, the analysis of two-dimensional structures will be performed. Two

different configurations have been selected, a square and a triangular lattice. Both of them have been evaluated for air columns embedded in a dielectric material and for dielectric columns on air. The selection of these structures is based on the fact that they will serve as substrate for the antenna applications presented in Chapter 4. Finally, two three-dimensional structures will be presented. The first one is the so-called "woodpile" and the second one is a new structure that exhibits a complete band gap that it is very easy to fabricate.

3.1 A One-dimensional Photonic Crystal

The study of Photonic Crystals will be started with the simplest possible case: a one-dimensional system. To understand the propagation of electromagnetic waves through these systems, the concepts of electromagnetism developed in the previous chapter will be applied. Even in these simple systems, the important features and the understanding of the Photonic Crystal can be achieved. Although the properties of dielectric layers may be known, because it is a system largely studied, by casting the discussion in terms of band structures and band gaps, the more complicated two, and three-dimensional system will be easier to develop and understand.

3.1.1 Introduction

The simplest possible Photonic Crystal consists of alternating layers of material with different dielectric constants [RUS 86, RUS 92, SMI 93, JOA 95 and YAR 97], as it is shown in Figure 3.1. This arrangement is not a very new idea, the properties of such *multilayer films* have been widely studied [HEC 74]. This Photonic Crystal can act as a perfect mirror for electromagnetic waves with a sharply defined frequency gap, and can localise modes if there are defects in its structure. This kind of device is commonly used in dielectric mirrors, optical filters and matching layers.

The traditional approach to an understanding of this system is to allow a plane wave to propagate through the material and to consider the multiple reflections that take place at each interface. In this chapter a method related with the analysis of band structure will be considered, which is easily generalised to the more complex two, and three-dimensional photonic band gap.

The structure, as shown Figure 3.1, is periodic in the z-direction, and homogeneous in the xy-plane. This allows indexing the modes using $k_{\|}$, k_z and n:

the wave vector in the plane, the wave vector in the z-direction, and the band number.

This configuration has been proven for a long time, showing a wide band gap for an incident wave in the z-direction, which depends on the thickness of the different layers, number of layers that form the repetition period and the dielectric contrast.

Recently, new studies about this configurati on have been performed. The working as a three-dimensional structure reflecting the incident wave for any direction of propagation has been proven in [WIN 98, YAB 98 and CHI 99]. This assumption is only valid when any source is not placed close to the one-dimensional structure. In this case evanescent modes in the free space become as propagating modes inside the Photonic Crystal. Therefore, under certain working conditions, the one-dimensional structure can act with three-dimensional performances. This new phenomenon can be used in a large number of applications to get easily onmi-directional reflections.

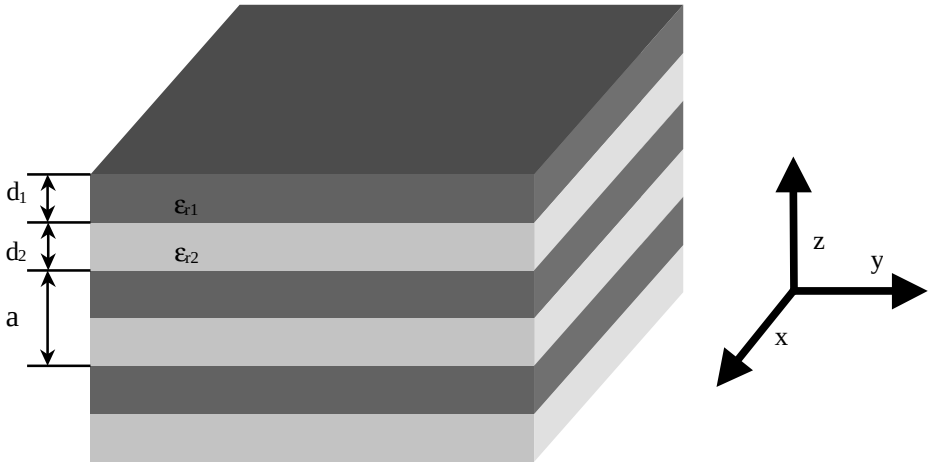

Figure 3.1: A one-dimensional Photonic Crystal formed by alternating layers of material (at least two) with different dielectric constant, spaced by a distance a.

The field distribution inside of this Photonic Crystal can be expressed as a combination of Bloch modes, which can be written in a brief way as,

$$H_{n,k_z,k_\parallel}(r) = e^{jk_\parallel r} e^{jk_z z} u_{n,k_z,k_\parallel}(z) \tag{3.1}$$

where n is the Bloch mode index, $u(z)$ is a z-periodic function, so that $u(z) = u(z+R)$ whenever R is an integral multiple of a, the layer spacing, k_z is the

wave vector in the propagating direction and $k_{\|}$ is the wave vector in the transverse direction (x-y plane).

3.1.2 Theoretical Analysis

After the description of the one-dimensional Photonic Crystal, the analysis of its features [JOA 95] will be carried out. In order to follow a coherent development, first of all, the parameters of the structure will be fixed (primitive lattice vectors, reciprocal lattice vectors and Brillouin Zone) , to finish with the dispersion relation curves obtained after solving the eigensystem given in equation 2.38.

For this case, the deduction of the crystal parameters is evident. As the only variation in the dielectric constant is in the z-direction, the primitive lattice vector is defined by $a\hat{z}$, and the reciprocal lattice vector, applying the condition set in the Chapter 2, is given by $(2p/a)\hat{z}$.

Only the case of an electromagnetic wave propagating in the z-direction, crossing the layers of dielectric at normal incidence will be considered. In this case, $k_{\|}=0$, hence only the wave vector component k_z will be important. The assumption $k_z = k$ can be done in the rest of this section without possibility of confusion.

The range of values which defines the Brillouin zone, following the consideration explained in the previous chapter, are $-p/a < k_z < p/a$.

As starting point, the analysis of a single infinite layer of an unchanging dielectric constant material will be done. It is known that in a uniform medium, the speed of an electromagnetic wave is reduced proportionality to the index of refraction. The frequency spectrum, dispersion curve, is just the light-line given by

$$w(k) = \frac{ck}{\sqrt{e}} \tag{3.2}$$

The normalised curve is plotted in Figure 3.2a where a dielectric cons tant of 13 has been used. In this way, from the equation 3.2, a normalised frequency, for $k=0.5$, of 0.1368 should be obtained. This result has been obtained solving the equation 2.38, and taking into account 100 modes in the calculations.

Once the analysis of the simplest case has been performed, the next step is to check what is happening when a layer of different dielectric constant is introduced periodically, as Figure 3.1 shows. The width of each layer is fixed to $0.5a$, where a is the size of the lattice and consequently the constant of periodicity in the z-direction.

Using two layers of alternating dielectric constant with $e_r = 1$ and $e_r = 13$, the dispersion relation plotted in Figure 3.2b has been obtained. A clear gap has appeared between the first and second energy bands, a frequency gap in which no mode, regardless of k, can exist in the crystal. This is what will be called *"photonic band gap"* for all the electromagnetic structures that will be analysed.

The dispersion relation is calculated by solving the eigenvalue problem of the equation 2.38. For each possible direction of propagation in k-space, the equation 2.38 is solved, obtaining, in this way, the different frequency values (eigenvalues) for each mode that can be propagated in the Photonic Crystal. At the same time, the eigenvectors are achieved. With these, the shape of each mode can be visualised. An example of this can be seen in Figure 3.3 and 3.4. The first one represents the first propagating mode (normalised frequency 0.16) when the normalised wave vector in z-direction is $k = 0.5$. Figure 3.4 is showing the second mode with normalised frequency 0.278 and for the same wave vector. It should be pointed out as the pattern in Figure 3.4 shows a higher frequency than the one plotted in Figure 3.3.

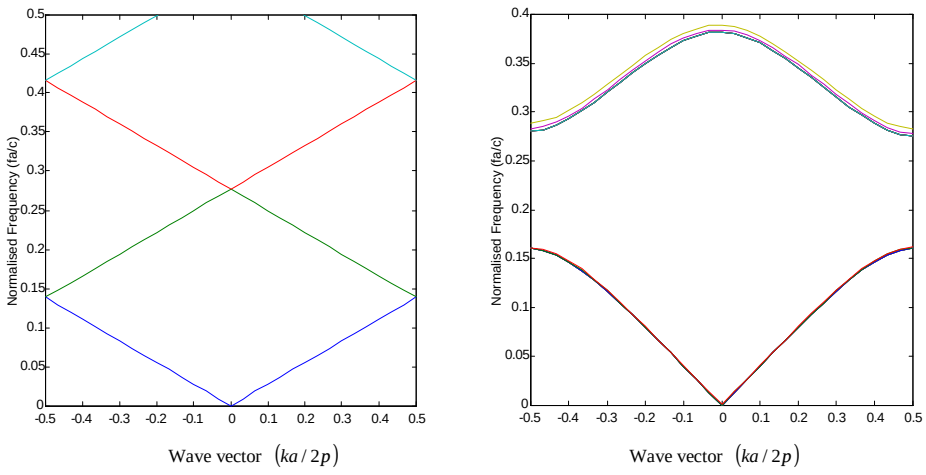

Figure 3.2: The dispersion relation diagram. *Left*: each layer has the same dielectric constant $e_r = 13$. *Right*: layers alternate between $e_{r_1} = 13$ and $e_{r_2} = 1$.

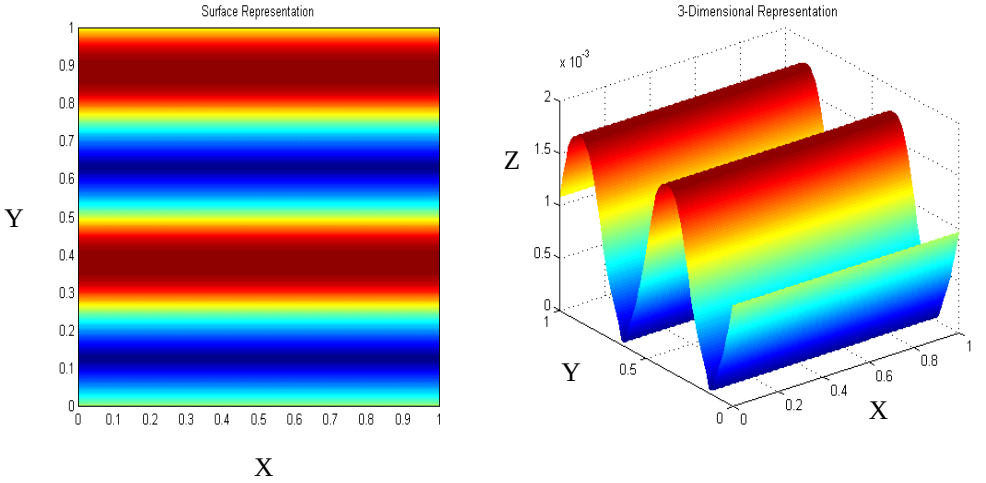

Figure 3.3: Magnetic field structure in absolute value for the first mode that can be generated in the studied case of one-dimensional Photonic Crystal of different dielectric layers. Two normalised periods of the structure are shown. *Left side*: surface plot. *Right side*: 3-D plot.

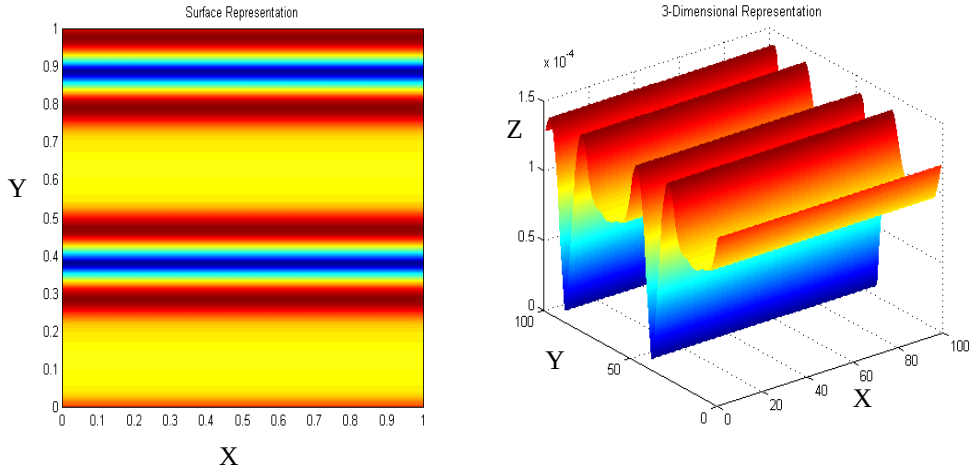

Figure 3.4: Magnetic field structure in absolute value for the second mode. Two normalised periods of the structure are shown. *Left side*: surface plot. *Right side*: 3-D plot.

It is important to n otice that the width of the gap depends of the dielectric contrast and it is increased when the dielectric contrast is larger. This fact can be

corroborated comparing Figure 3.2(b), where the difference between dielectric constant is high (*13/1*), and Figure 3.5, where this difference is much less (*13/12*).

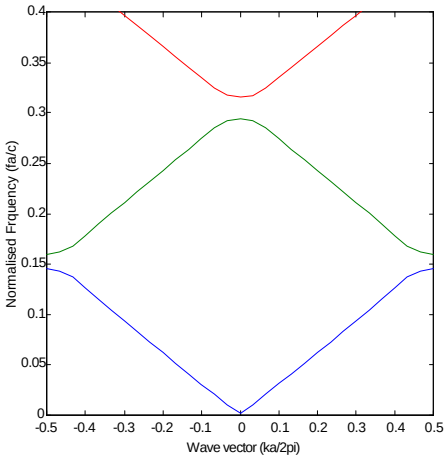

Figure 3.5: The dispersion relation of the one-dimensional Photonic Crystal formed by layer of two different dielectric constant ($e_{r_1} = 13$ and $e_{r_2} = 12$).

The extent of a band gap can be characterised by its frequency width Δw , but this is not a really useful measure, because all the results are scalable, as it was explained in Chapter 2. This means that the photonic band crystal is expanded by a factor *s*, the frequency width will becomes in $\frac{\Delta w}{s}$. A more useful characterisation, which is independent of the scale of the crystal, is the gap- midgap ratio [JOA 95]. Letting w_0 be the frequency at the middle of the gap, the gap- midgap ratio is defined as $\frac{\Delta w}{w_0}$. If the system is scaled up or down, all the frequencies scale accordingly, but this quantity stays the same. For the cases under study, the obtained gap-midgap ratio is about 52% for the case with higher dielectric contrast and 10% for the another case.

3.1.3 An intuitive explanation about the origin of the band gap

In order to offer an explanation for the physical origin of the gap, the electric field distribution for the modes immediately above and below the gap will be studied. The gap between bands always occurs at the edges of the Brillouin zone, in this case, this gap appears at $k = p / a$. Focusing on the case where a high

dielectric contrast is used, for $k = p / a$, the modes are standing waves with a wavelength of $2a$, twice the crystal lattice constant.

There are two ways to centre a standing wave of this type. One possibility is with its nodes in each low- ε layer, or in each high- ε layer. Any other position would violate the symmetry of the unit cell about its centre.

But in the study of the electromagnetic *variational theorem* carried out in Chapter 2, it was found out that the low-frequency modes concentrate their energy in the high- ε regions [JOA 95]. With this in mind, it is understandable why there is a frequency difference between the two cases.

The mode just under the gap has its power concentrated in the $e_r = 13$ regions, giving it a lower frequency (see Figure 3.6). Meanwhile, the mode just above the gap has most of its power in lower $e_r = 1$ regions, so its frequency is raised a bit.

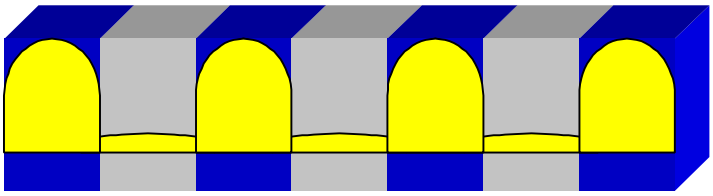

Figure 3.6: Schematic illustration of the mode associated with the lowest band in the gap. The blue colour represents the high dielectric constant and the grey one the low.

Observing the real representation of the field distribution in the different modes, see Figure 3.3 and Figure 3.4, it can indeed be seen that the power is concentrated in the high dielectric medium (first mode) and in the low dielectric medium (second mode), confirming the previous discussion.

Unfortunately, this is a guideline and is not always valid. Sometimes, the two modes at the bottom and at the upper part of the gap do not have the field completely concentrated in the different layers of the Photonic Crystal respectively. In these cases, it is found that the fields for both bands are primarily concentrated in the high- ε layers, but in different ways; the bottom band being more concentrated than the top. The gap is generated due to the different field energy localisation. As in semiconductors, different energy localisation means different level of energy, needing an external energy to be able to pass from a low mode to a high order mode.

As conclusion of this section, it can be asserted that a gap always happens between every set of bands, at either the Brillouin's zone edge or its centre. This property can be observed in Figure 3.2(b), as well as in Figure 3.5. Finally, note that band gap always appears in one-dimensional Photonic Crystal for any dielectric constant. The smaller the contrast, the smaller the gap, but the gap opens up as soon as $e_{r_1} / e_{r_2} \neq 1$.

3.2 Two-dimensional Photonic Crystal

After discussing some interesting properties of one-dimensional Photonic Crystals in the previous section, the analysis of two-dimensional periodic structures will be performed in this section. The structure will be considered periodic in the x-y plane and unchanged in z-direction. Therefore, the propagation will be examined in the plane of periodicity.

The electromagnetic wave propagating in this plane will be split into two independent polarisations. The analysis of the Photonic Crystal will depend on the considered incident polarisation. The different behaviours as function of this dependence will be explored. A theoretical explanation about how it is possible to separate the two polarisations will be shown.

There are a great number of two-dimensional structures, which can be studied [MAR 93, MEA 93a, KUR 94, MAR 94, BAB 95a, CAS 96, DUR 98, GON 98a and GON 98b], depending principally on the lattice structure and the shape of the atoms. However, only two main different configurations will be analysed; a square [MEA 93a, KUR 94, JOA 95 and GON 98c] and a triangular-hexagonal [KUR 94, JOA, 95, CAS 96 and GON 98c] lattice of columns. Each of them offers two possibilities, dielectric columns or air columns embedded in air or in dielectric materials respectively. The idea of focusing only in these structures is because it is already known that they exhibit different type of band gap, as function of the polarisation or the lattice arrangement. Besides, as it will be shown in Chapter 4, they are very promising candidates as Photonic Crystal substrate for antenna applications in microstrip technology.

The field energy distribution will be shown in order to be able to distinguish modes from different energy bands, trying to explain the reason of appearance of the photonic band gap, like it was done in the previous section.

Plots with the localisation of the photonic band gaps of these two-dimensional Photonic Crystals, when one or more of the main parameters of the crystal are varied, will be presented. These plots are called " *Gap Maps*" [JOA 95].

3.2.1 Introduction

A two dimensional Photonic Crystal is a periodic structure along two axes and homogeneous along the third. For simplicity, the selected plane of periodicity will be the x-y plane. These crystals can have a band gap in the x-y plane as function of the plane of polarisation, size of the columns, dielectric contrast and filling factor. Two cases will be analysed, consisting of a square lattice and a triangular hexagonal of columns.

As it has already been proven, the one-dimensional Photonic Crystal was able to reflect all the waves in the periodicity direction, now, the two-dimensional Photonic Crystal will reflect all incident waves from any direction in the plane of periodicity.

The electromagnetic field inside of these two-dimensional Photonic Crystal can be written in a Bloch form as,

$$H_{n,k_z,k_\parallel}(r) = e^{jk_\parallel \cdot r} e^{jk_z z} u_{n,k_z,k_\parallel}(r) \tag{3.3}$$

being n the Bloch mode and $u(r)$ a periodic function, $u(r) = u(r+R)$, for all lattice vectors R. In this case, the wave vector $k_\parallel$, where $k_\parallel = kx \cdot \hat{x} + ky \cdot \hat{y}$, is restricted to the Brillouin zone, because it is the plane in which the periodicity is placed, and k_z is unrestricted, because there is not periodicity in that direction.

The function is periodic in the x-y direction and not in the z-direction. Selecting $k_z = 0$, the electromagnetic wave is propagating strictly in the x-y plane, then the system is invariant under reflections in the x-y plane.

3.2.2 Electromagnetic fields

For two-dimensional structure, the field behaviour can be divided into two polarisations since the interaction between them is not possible. In order to clarify how it is achieved this separation [GON 98c] , the main equation of the obtained eigensystem in Chapter 2 is written again,

$$\sum_{G'} |k+G\|k+G'| h_{G-G'} \begin{bmatrix} \hat{e}_2(k+G)\cdot\hat{e}_2(k+G') & -\hat{e}_2(k+G)\cdot\hat{e}_1(k+G') \\ -\hat{e}_1(k+G)\cdot\hat{e}_2(k+G') & -\hat{e}_1(k+G)\cdot\hat{e}_1(k+G') \end{bmatrix}$$

$$\begin{pmatrix} h_{n,1}(k+G') \\ h_{n,2}(k+G') \end{pmatrix} = -\frac{w^2{}_{n,k}}{c^2} \begin{pmatrix} h_{n,1}(k+G) \\ h_{n,2}(k+G) \end{pmatrix} \tag{3.4}$$

In the case of considering only a two-dimensional structure, it very easy to prove that the following values in the equation 3.4 are zero:

$$-\hat{e}_2(k+G)\cdot\hat{e}_1(k+G') = 0 \tag{3.5}$$

$$-\hat{e}_1(k+G)\cdot\hat{e}_2(k+G') = 0 \tag{3.6}$$

this means that there is not interaction between the $\hat{e}_1$ and $\hat{e}_2$ vectors and therefore, the equation 3.4 can be divided as,

$$\sum_{G'} |k+G\|k+G'| h_{G-G'} \hat{e}_2(k+G)\cdot\hat{e}_2(k+G') h_{n,1}(k+G') =$$

$$= -\frac{w^2{}_{n,k}}{c^2} h_{n,1}(k+G) \tag{3.7}$$

$$\sum_{G'} |k+G\|k+G'| h_{G-G'} \hat{e}_1(k+G)\cdot\hat{e}_1(k+G') h_{n,2}(k+G') =$$

$$= -\frac{w^2{}_{n,k}}{c^2} h_{n,2}(k+G) \tag{3.8}$$

Solving these two equations, the eigenvalues an d eigenvectors for the two different polarisations are obtained. The band structure or dispersion relation for any *k* in the two-dimensional Photonic Crystal can now be achieved.

The two polarisations in which the field can be divided will be defined as the *transverse electric* (TE) modes when the *H* field is normal to the plane of periodicity, and the *E* field is in the plane of periodicity, and, *transverse magnetic* (TM) modes have just the reverse. These one will correspond with the $\hat{e}_1$ (for TM polarisation) or $\hat{e}_2$ (for TE polarisation) vectors.

The dispersion relation for TE and TM modes will be completely different; in particular, there will be cases in which band gaps will appear for one polarisation and not for the other.

3.2.3 A Square Lattice of Columns

This two-dimensional Photonic Crystal is composed by a square array of columns infinite periodic in the x-y plane and constant in z-direction. Two different cases are going to be studied, dielectric columns in air substrate and air columns in a dielectric substrate. A complete analysis as function of their main parameters will be developed. The action as TM suppresser for the case of dielectric columns embedded in air substrate and as TE and TM suppresser for the other case will be proven.

Before beginning with these cases, the parameters of the unit cell for the crystal structure under study will be presented. In order to analyse the two-dimensional structure , the primitive lattice vector, the reciprocal lattice vector and the Brillouin zone have to be correctly defined.

3.2.3.1 Primitive lattice

A two-dimensional structure periodic in the x-y plane will be composed by two main vectors placed in the periodic plane. As this two-dimensional Photonic Crystal is formed by a square lattice, the vectors that define the direct lattice can be written as:

$$\begin{aligned} \hat{a}_1 &= a\,\hat{x} \\ \hat{a}_2 &= a\,\hat{y} \end{aligned} \tag{3.9}$$

where a is any lattice size. Due to this general definition, the size of the Photonic Crystal will be completely normalised and will be scalable in frequency. The most important parameter that will be used to define the shape of this structure is the r/a ratio, where r is the radius of the column (see Figure 3.7). This ratio will define the filling factor of the columns material in relation with the unit cell size.

3.2.3.2 Reciprocal Lattice

Once the primitive lattice vectors are defined, the reciprocal lattice vectors can be fixed. Using the equation 2.3 the vectors are the defined as:

$$\begin{aligned} \hat{b}_1 &= 2p/a\,\hat{y} \\ \hat{b}_2 &= 2p/a\,\hat{x} \end{aligned} \tag{3.10}$$

A plot of these vectors in the reciprocal space is shown in Figure 3.8:

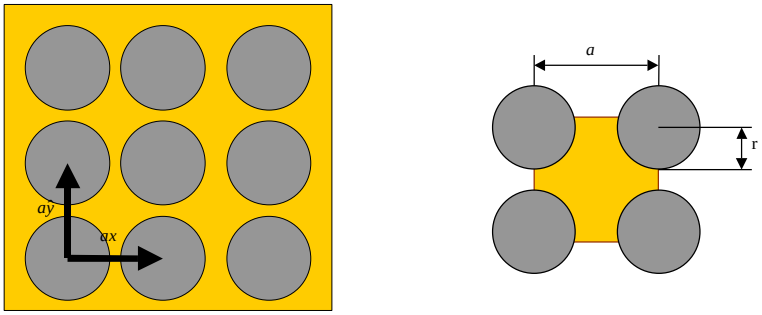

Figure 3.7: Array of square lattice points in the real space.

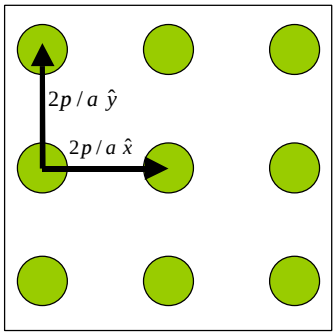

Figure 3.8: Reciprocal lattice vectors of a square lattice.

3.2.3.3 Brillouin zone

Following the steps mentioned in Chapter 2, the Brillouin zone for this structure can be found. The Figure 3.9 represents the steps followed (taking the centre point as the origin, the lines connecting the origin with the other lattice points (red) are drawn, their perpendicular bisectors (blue), and highlighted is the square boundary of the Brillouin zone (yellow)) and the final zone, which defines the Brillouin *k*-space.

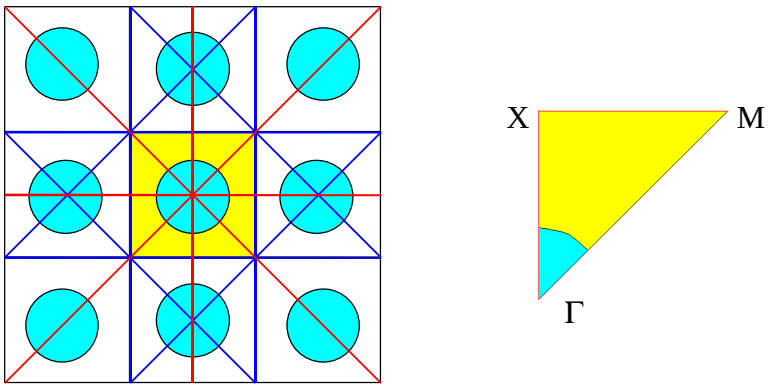

Figure 3.9: *Left*: The construction of the Brillouin zone. *Right*: Irreducible Brillouin zone.

The irreducible Brillouin zone is the triangular wedge in the upper-right corner; the rest of the Brillouin zone can be related to this wedge by rotational symmetry. There are three special points called Γ, X and M which correspond respectively to $k_{\|}=0, k_{\|}=\frac{p}{a}\hat{x}, k_{\|}=\frac{p}{a}\hat{x}+\frac{p}{a}\hat{y}$ which describe completely the irreducible Brillouin zone. This means that doing a sweep over this zone, all directions in the *k*-space of the propagating incident waves will have been taken into account.

3.2.3.4 A Square Lattice of Dielectric Columns

In this section, the analysis of the two-dimensional array of square dielectric columns will be performed (see Figure 3.10). For all the analysed cases, a wave that propagates in the x-y plane will be considered. As starting point, the dispersion relation for a Photonic Crystal structure consisting of dielectric ($e_r=10$) rods with a $r/a=0.3$ ratio has been calculated (see Figure 3.11). The dielectric constant value has been chosen following a conventional value used in microstrip technology. The obtained results have been compared with the results presented in [JOA 95]. Both polarisations TE and TM are plotted. Along the horizontal axis, the in-plane wave vector *k* goes along the edge of the irreducible Brillouin zone.

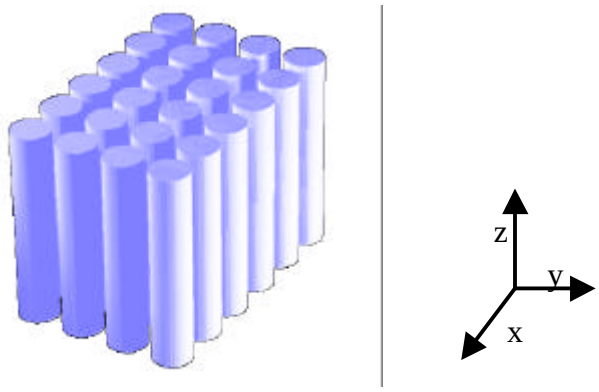

Figure 3.10: A two-dimensional square array of dielectric columns in an air substrate, with radius r and dielectric constant e_r.

It is important to remember that in all the cases, the vertical axis shows the normalised frequency value, this means, that the behaviour of this Photonic Crystal can be scaled to work at any frequency.

The results shown in Figure 3.11 have been obtained using 12 points to sample the unit cell for each periodic direction x-y. This is equivalent to take into account 144 plane waves in the analysis. The TE modes are represented by solid lines, while the TM modes by dashed lines. As conclusion of these results, it is clear that this Photonic Crystal exhibits a complete band gap for the TM modes but not for TE modes.

In order to check the convergence of the calculations, other checks were done increasing the number of modes without obtaining any appreciable variation in the final results. In Figure 3.12 the calculated TE and TM modes for 12 and 16 sampled points respectively are plotted (144 and 256 plane waves, respectively). Therefore, it is sufficient to take into account 12 points in each direction of periodicity, because the results present enough convergence.

Nevertheless, if high order modes have to be considered, considerable differences are found. This is something expected because, for an adequately representation of the high order modes it is necessary to take into account a larger number of plane waves.

Note that in Figure 3.11 it is possible to see that the second and third band for TM modes have the same eigenvalue in the M point. This means that they are degenerate modes, and in this case, the energy field structure will be the same for

both modes. The same behaviour is happening at this point between the second and third band for TE modes.

The exhibition of these degenerate modes for both TE and TM polarisations modes means that this Photonic Crystal configuration presents a symmetry point in the propagation direction marked by the M point.

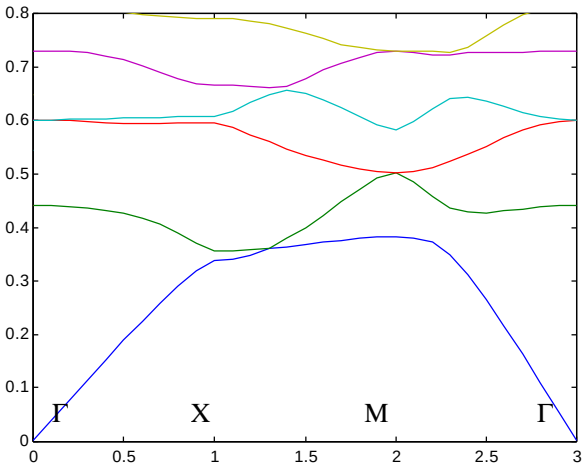

Figure 3.11: Dispersion relation diagram for TE (solid lines) and TM (dashed lines) modes in the case of a square lattice of the dielectric columns. Each colour indicates different energy bands. The design parameters are, $r = 0.3a$ and $e_r = 10$.

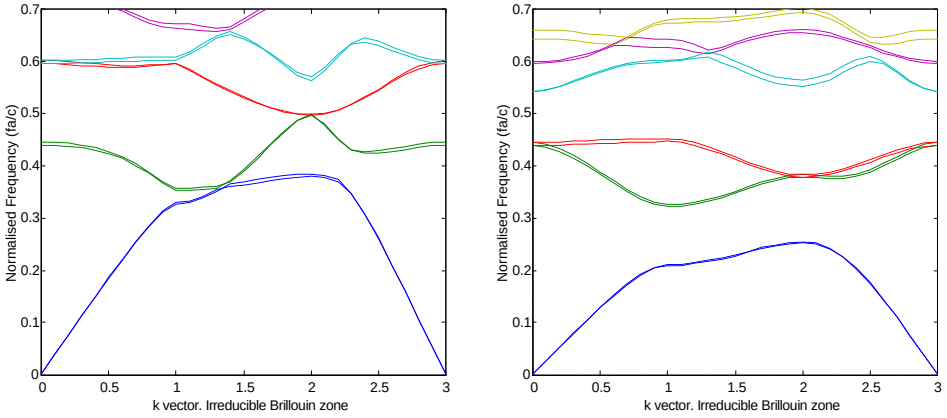

(a) (b)

Figure 3.12: Dispersion relation for TE (a) and TM (b) modes obtained using 144 (solid lines) and 256 (dashed lines) plane waves.

Once the dispersion relations representing the eigenvalues have been calculated and analysed, the next step is to represent the field structures of the modes using the eigenvectors obtained in the same calculations. The idea is to visualise the modes in order to be able to explain the behaviour of the band gap between two different energy modes, by proving whether the mode concentrates its energy in the air or in the dielectric regions.

As it was explained in Chapter 2, the eigenvectors obtained correspond to the $\vec{H}$ field component. This implies that the magnetic field $\vec{H}$ will be achieved automatically after solving the eigensystem. From the $\vec{H}$ field, the displacement field $\vec{D}$ can be solved knowing that $\nabla x\vec{H} = \frac{\P\vec{D}}{\P t}$. Developing this equation,

$$\begin{aligned} \hat{d}_{TE} &= -\frac{|k+G|}{jw_p}\hat{h}_{TM} \\ \hat{d}_{TM} &= -\frac{|k+G|}{jw_p}\hat{h}_{TE} \end{aligned} \tag{3.11}$$

where $\hat{h}_{TE}$ and $\hat{h}_{TM}$ are the eigenvectors for the magnetic field, $\hat{d}_{TE}$ and $\hat{d}_{TM}$ for the displacement field and w_p is the corresponding eigenvector in the *k*-point where the displacement field is going to be calculated.

Focusing on a specific point in the Brillouin zone, the $\vec{H}$ and $\vec{D}$ field distribution for any mode can be obtained. Selecting the X point of the Brillouin zone, the Figures 3.13 and 3.14 represent the $\vec{H}$ field surface plots for the first and second modes. In both cases two periods have been drawn. The period length has been normalised to the constant value *a*.

Another very interesting feature to check is how the modes look like at the degenerated normalised frequency point. To see this, the $\vec{H}$ field distribution for the second and third TE mode in the M point has been plotted in Figure 3.15. As it was expected, both configurations have the same $\vec{H}$ field distribution, the only difference is a 180 degrees displacement in phase.

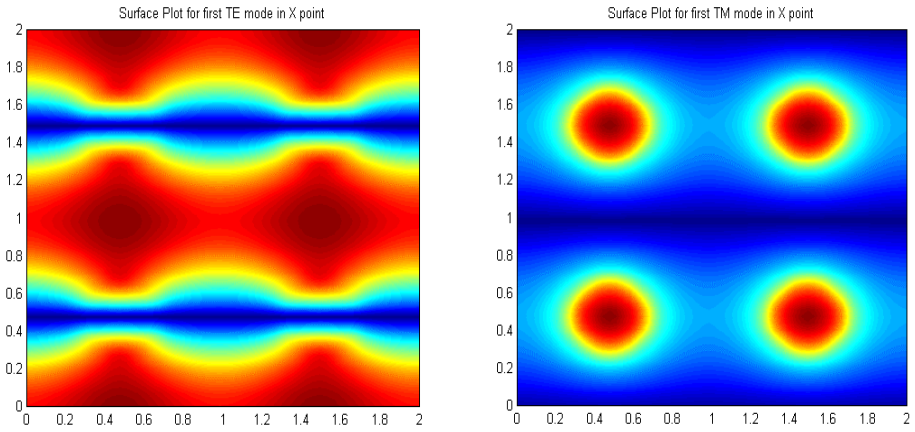

(a) (b)

Figure 3.13: Surface plots of the first TE (a) and TM (b) modes. The figures have been plotted with the absolute value of the $\vec{H}$ field. Two periods have been drawn.

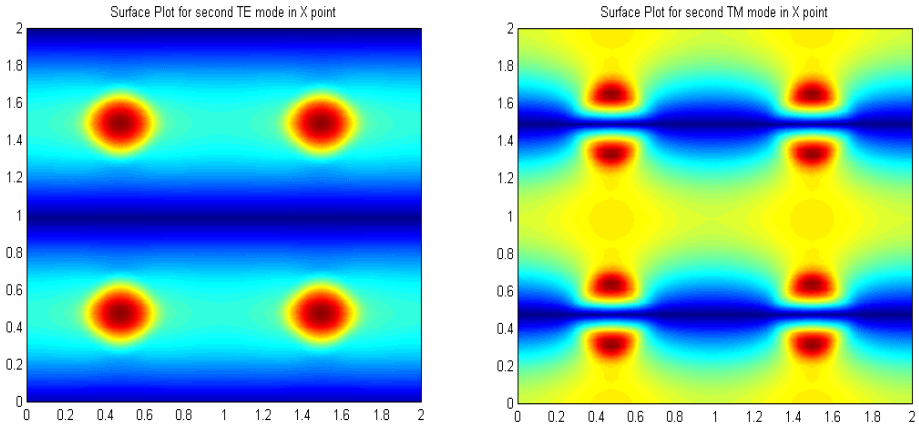

(a) (b)

Figure 3.14: Surface plots of the second TE (a) and TM (b) modes. The figures have been plotted with the absolute value of the $\vec{H}$ field. Two periods have been drawn.

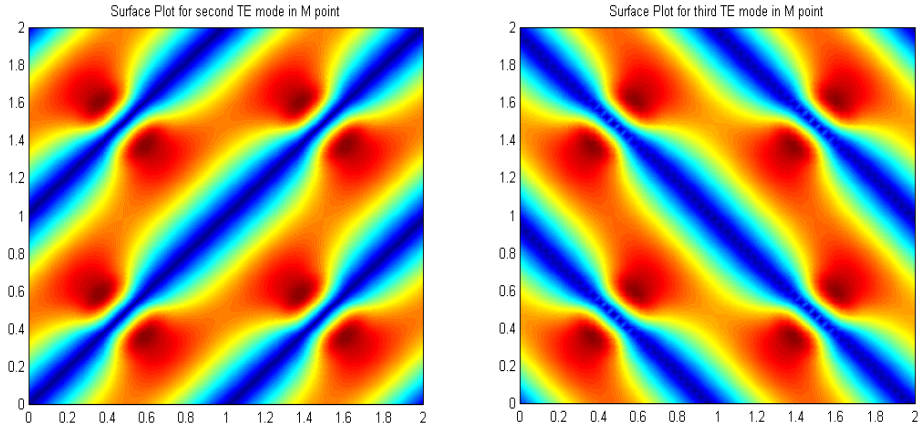

(a) (b)

Figure 3.15: Surface plots of the second TE (a) and third TE (b) modes. The figures have been plotted with the absolute value of the $\vec{H}$ field. Two periods have been drawn.

As it was explained in the previous section, a low frequency mode concentrates most of its displacement energy ($\vec{D}$ field) in the high- ε regions, as it is stated by the varational theorem. Normally, this fact explains the large frequency difference between two modes. In order to prove whether the first band has the most of its power in the dielectric regions and the second in the air region, which correspond with an increase in frequency for higher modes, the degree of concentration of the displacement fields in the unit cell will be computed. In order to perform it, the "*fill factor*" [JOA 95] parameter will be defined as

$$f = \frac{\int_{Vdiel} \vec{E}^* \cdot \vec{D} \cdot dVdiel}{\int_{V} \vec{E}^* \cdot \vec{D} \cdot dV} \tag{3.12}$$

This parameter measures the fraction of electrical energy located inside the high-ε regions. Table 3.1 shows the fill factor for first and second TE and TM modes in the case of dielectric columns of $e_r = 8.9$ and $r = 0.2a$. This change in the parameters of the unit cell has been done in order to be able to perform a comparison with the other author's results. The behaviour of this lattice can be looked up in [JOA 95 and GON 98c]. Also the dispersion relation diagram is quite close to that shown in Figure 3.11.

	1er Mode	**2nd Mode**
TE	7.37 %	37.8 %
TM	86.5 %	27.8 %

Table 3.1: Fill factor for square dielectric rods in the X point at the Brillouin zone. Radius $r = 0.28a$.

Note that the radius used to get these results is not $r = 0.2a$, but $r = 0.28a$. This is due to the smoothing done in the definition of the dielectric constant in the unit cell performed in the generation of the eigensystem in Chapter 2. This implies that the radius must be elongated a little bit before calculating the fill factor in order to compensate for that smoothing. The radius variation can appear quite large, but taking into account that each point in the dielectric constant mesh is taken with approximately a resolution of 0.1, the selected radius in Table 3.1 is as expected.

The first band of the TM mode has a fill factor of 86.5%, far from the 27.8% obtained for the second mode. This difference in the energy distribution of consecutive modes generates the band gap along this direction of propagation.

The fill factors for TE modes do not contrast as strongly. An explanation for this could be as follows: the scalar D_z field of the TM modes can be localised within the columns, but the continuous field lines of the TE modes are obliged to penetrate the air regions to connect neighbouring columns; as a result, consecutive TE modes can not exhibit markedly different fill factors, and band gaps do not appear.

Instead of using the fill facto r defined for the electric field, the magnetic field fill factor may be defined as,

$$f = \frac{\int_{Vdiel} \vec{H}^* \cdot \vec{B} \cdot dVdiel}{\int_{V} \vec{H}^* \cdot \vec{B} \cdot dV} \tag{3.13}$$

Table 3.2 shows the obtained results using the above equation for the same case studied previously.

Different results have been achieved using equation 3.12 or equation 3.13. This was expected, since the magnetic field is related to the electric field, through the impedance value.

	1er Mode	**2nd Mode**
TE	16.8 %	58.9 %
TM	75 %	27.7 %

Table 3.2: Fill factor obtained using equation 3.12 for square dielectric rods in the X point at the Brillouin zone. Radius r=0.28a.

In order to validate the obtained results, a comparison between the values published in [JOA 95] and those of Table 3.1 are shown in Table 3.3.

	Values Obtained		Values of [JOA 95]	
	TM	TE	TM	TE
Dielectric Band	**86.5**	**27.8**	**83**	**23**
Air Band	**37.8**	**7.37**	**32**	**9**

Table 3.3: Comparison between results from equation 3.11 and results in [JOA 95]. Now, the modes have been classified as dielectric and air modes depending on the energy distribution (see [JOA 95] for more clarity).

As a conclusion of this analysis, it is possible to say that the results shown in Table 3.3 are in good agreement.

Up to now, the dispersion relations given in Figures 3.11 and 3.12 show the existence of band gaps for TM or TE modes, but only for fixed parameters. This means that the figures are only valid for a dielectric constant value and for a r/a ratio. This is not the most useful tool in order to design the adequate parameters of any Photonic Crystal structure to work within the band gap region.

In order to allow a fast design, a graphical tool called " *gap map*" can be used. This graph can be obtained by doing a sweep for r/a ratio and obtaining the different dispersion relations. Plotting the band gap for each solution, the gap map is achieved. Along the horizontal axis of the gap map the radius of the columns is plotted; whereas along the vertical axis the normalised frequency is represented.

Figure 3.16 shows the gap map for the square array of dielectric columns with dielectric constant $e_r = 10$. The dielectric constant used is 10 in order to use these results for the design in the next chapter. The plot has been calculated using 400 plane waves.

Analysing the Figure 3.16, the TM gap map reveals some interesting features. First of all, the gaps decrease in frequency as r/a increases. This is an expected feature, since the average dielectric constant of the medium is increased (the frequency scales as $1/\sqrt{e}$). Secondly, there is a repetition pattern of the largest gap whereby smaller copies of it are stacked along the frequency axis at

roughly equal intervals. About the TE Gap Map case, there are no significant gaps at all, therefore it is proven that this Photonic Crystal can not be used to suppress TE propagation.

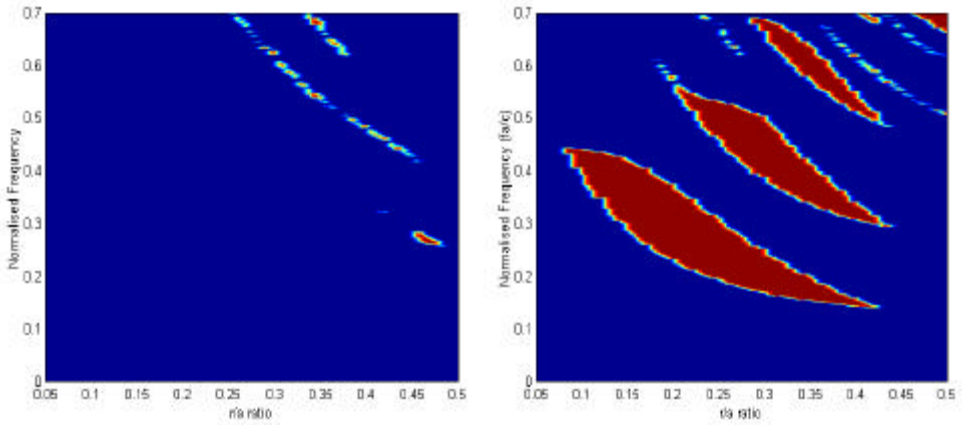

Figure 3.16: Gap Map for TE (right side) and TM (left side) modes in the case of dielectric columns with $e_r = 10$.

3.2.3.5 A Square Lattice of Air Columns

The next Photonic Crystal structure to study corresponds to the complementary case, a square array of air columns in a dielectric substrate, as it is illustrated in Figure 3.17.

In this section, due to the extensive development carried out for the case of dielectric columns embedded in an air substrate, only the most representative analysis will be presented. This corresponds to the gap map solutions, which define completely the features of this Photonic Crystal.

Using the same dielectric constant that in the previous case $e_r = 10$, the gap map plots are shown in Figures 3.18 and 3.19, where Figure 3.18 shows the TE and TM gap maps and Figure 3.19 shows the total (TE-TM) gap map. The analysis has been performed using 400 plane waves.

Immediately it can be seen from these figures that the working frequencies are longer when r/a ratio is increased. This effect is reverse to the previous case and it is expected because, in this case, increasing the r/a ratio, the average dielectric constant of the medium is reduced.

The gap structure for TM modes is opening up around $r/a = 0.4$, in contrast with the previous case where for this value the gap was closed. It seems that both structures are in one sense complementary.

For the TE polarisation, the square lattice of air columns presents several gaps. Furthermore, one of these gaps overlaps in a small amount with the gap for the TM polarisation, so in this case a *complete gap* appears (see Figure 3.19). This complete gap is thin, appearing from $r/a = 0.46$ to $r/a = 0.5$ with relative small bandwidths.

Note that in all figures the r/a ratio is swept up to values bigger than 0.5, this means that the air columns are touching each other, and air columns from one unit cell are entering in other unit cells.

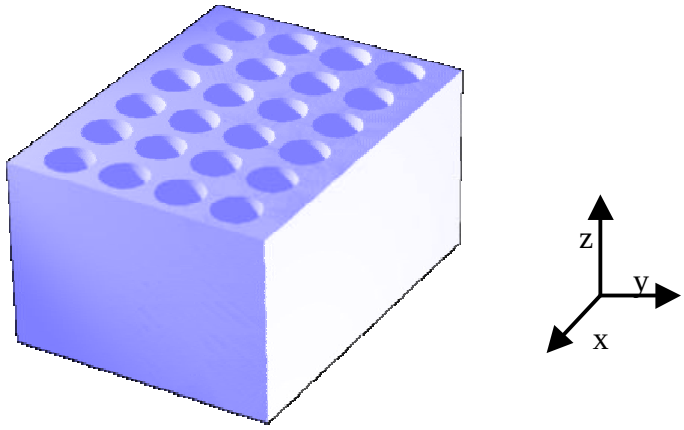

Figure 3.17: Two-dimensional Photonic Crystal formed by a square array of air columns embedded in a dielectric substrate.

Finally, it should be pointed out that with this structure an advantage for the TM polarisation in relation with the frequency-size ratio could be achieved. For the case of $r/a \cong 0.45$, very low normalised frequency values are obtained ($\cong 0.17$). This means that fixing the working frequency, the size of the structure, which possesses a band gap, will be quite small, which is translated to the fabrication of smaller structures.

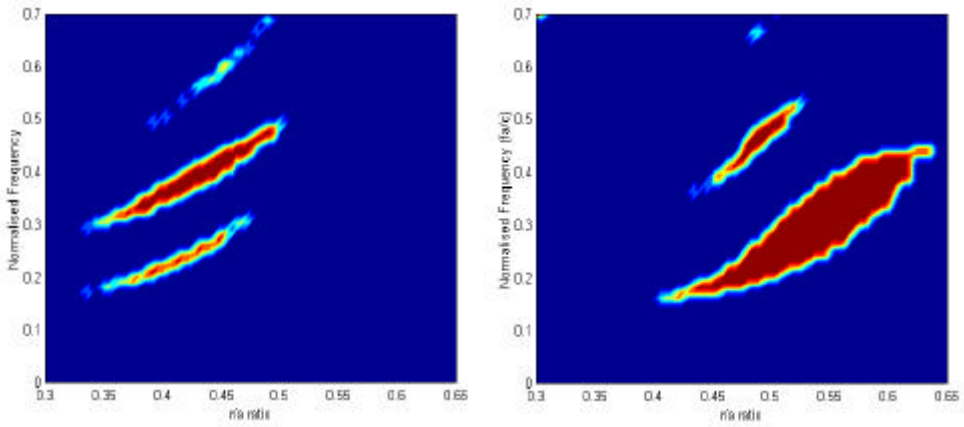

Figure 3.18: Gap Map for TE (left side) and TM (right side) modes in the case of air columns in a dielectric substrate with $e_r = 10$

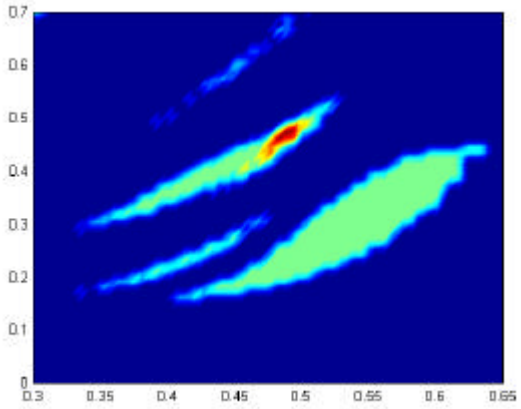

Figure 3.19: Gap Map for TE and TM modes. A complete gap can be observed (red colour in the picture).

3.2.4 A triangular-hexagonal lattice of columns

This two-dimensional Photonic Crystal is composed by an array of columns infinitely periodic in the x-y plane and constant in z-direction forming a triangular-hexagonal lattice. As in the previous section, the two complementary cases will be studied; dielectric columns in air substrate and air columns in a dielectric substrate.

First of all, the unit cell parameters for this Photonic Crystal will be described; the primitive lattice vector, the reciprocal lattice vector and the Brillouin zone.

3.2.4.1 Primitive lattice

As the two-dimensional Photonic Crystal is formed by a triangular lattice, the vectors that define the primitive lattice are as:

$$\begin{aligned} \hat{a}_1 &= \frac{a}{2}\left(\hat{x} + \sqrt{3}\cdot\hat{y}\right) \\ \hat{a}_2 &= \frac{a}{2}\left(\hat{x} - \sqrt{3}\cdot\hat{y}\right) \end{aligned} \tag{3.14}$$

where a is any lattice size defined as the distance between the any centres of two columns. As always, the structure will be completely normalised and will be scalable in size and frequency.

Note that for this case, this is not the unique definition for the direct vectors (see Figure 3.20), other definitions can be used obtaining the same performances.

3.2.4.2 Reciprocal Lattice

Once the primitive lattice vectors are defined, it is possible to find the reciprocal lattice vectors. Using the equation 2.3, these vectors can be written as,

$$\begin{aligned} \hat{b}_1 &= \frac{2p}{a}\left(\hat{x} + \frac{\hat{y}}{\sqrt{3}}\right) \\ \hat{b}_2 &= \frac{2p}{a}\left(\hat{x} - \frac{\hat{y}}{\sqrt{3}}\right) \end{aligned} \tag{3.15}$$

A plot of these vectors in the reciprocal space is shown in Figure 3.21. Note that these vectors will depend on the selected primitive lattice.

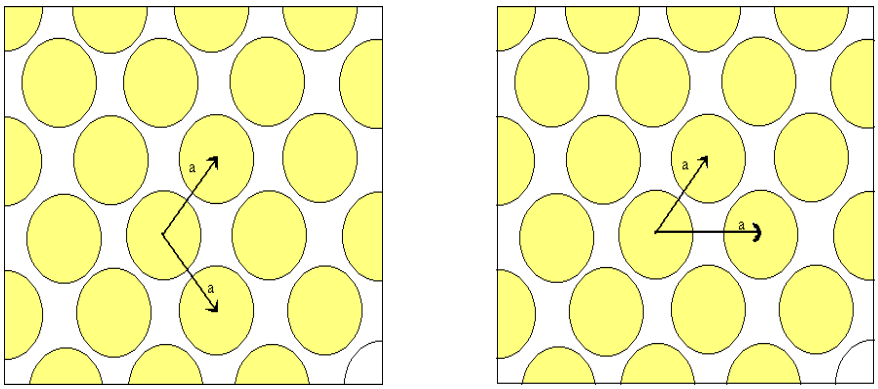

Figure 3.20: The network of the lattice points in the direct lattice. Right and left side are showing the same structure but with two different ways to select the primitive vectors.

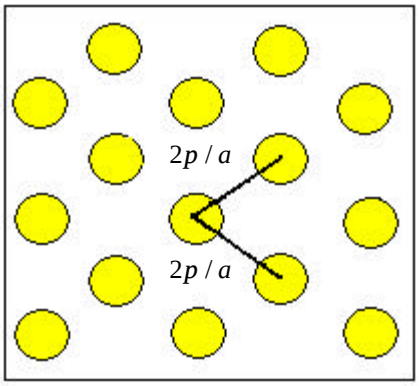

Figure 3.21: Reciprocal lattice vectors of a triangular-hexagonal lattice.

3.2.4.3 Brillouin zone

Following the steps mentioned in Chapter 2, the obtained Brillouin zone for this structure is plotted in Figure 3.22, where the steps (taking the centre point as the origin, the lines connecting the origin with the other lattice points (black) are drawn, their perpendicular bisectors (red), and highlighted is the square boundary of the Brillouin zone (yellow)) and the final result to achieved this zone are represented..

The irreducible Brillouin zone is the triangular wedge in the upper-right corner; the rest of the Brillouin zone can be related to this wedge by rotational symmetry. There are three special points called Γ, X and M which correspond

respectively to $k_{\|}=0, k_{\|}=\frac{2p}{\sqrt{3}a}\hat{y}, k_{\|}=\frac{2}{3}\frac{p}{a}\hat{x}+\frac{2p}{\sqrt{3}a}\hat{y}$ which describe completely the Irreducible Brillouin zone.

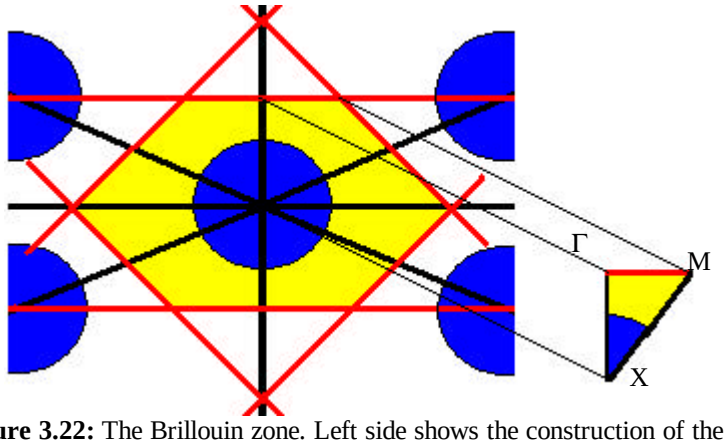

Figure 3.22: The Brillouin zone. Left side shows the construction of the Brillouin zone and the right side the Irreducible Brillouin Zone.

3.2.4.4 A triangular-hexagonal dielectric columns Photonic Crystal

In this section, the behaviour of a triangular-hexagonal Photonic Crystal with dielectric columns embedded in an air substrate is performed (see Figure 3.23).

The band structure (dispersion relation) for this lattice with a particular relation $r/a=0.28$ and dielectric constant $e_r=10$ is shown in Figure 3.24. The calculations were performed by using 20 points to sample the unit cell (400 plane waves in the analysis). The TE modes are represented by solid lines and the TM modes by dashed lines. This Photonic Crystal structure exhibits a complete photonic band gap for the TM modes but not for TE modes, similar features that in the square lattice case.

A remarkable feature is found out looking at the second and third TE mode. Following the sweep along *k*-vector, it seems that a gap is going to appear, however, just in the M point both modes present the same eigenvalue (degenerate modes). This is produced because this crystal is showing a symmetry point in that place which does not allow to open the band structure.

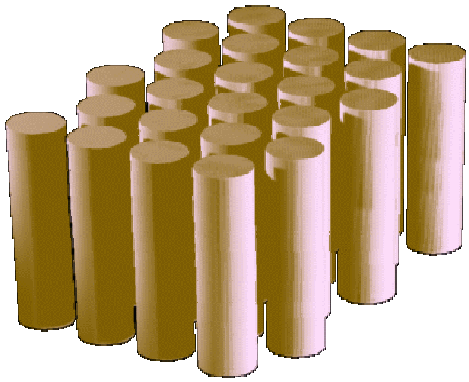

Figure 3.23: Two-dimensional Photonic Crystal formed by dielectric columns in an air substrate.

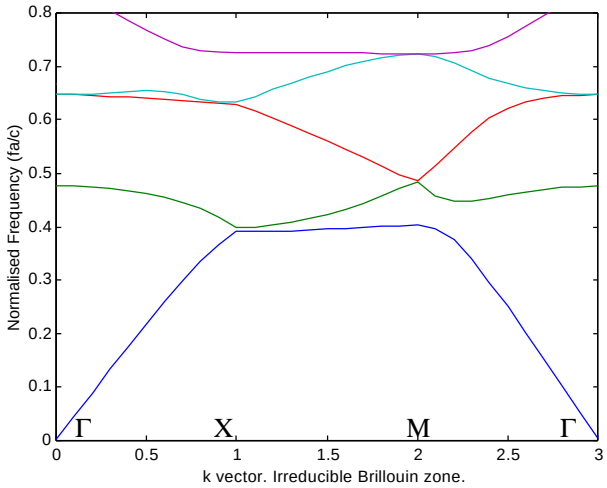

Figure 3.24: Energy Bands structure for TE (solid lines) and TM (dashed lines) modes for a triangular-hexagonal lattice of dielectric columns. Each colour indicates a different mode. The parameters used to obtain the plot are $r = 0.28a$ and $e_r = 10$.

The validation of these results have been done in (GON 98c) by doing a comparison between Figure 3.24 and the results from the Pendry's program [BEL 95], which analyses the transmission and reflection parameters using the TMM (Transfer Matrix Method).

As it was said in the previous section, this kind of representation does not give a full information about the behaviour of a Photonic Crystal as function of its parameters, and it is only applicable to a specific case. The gap map for this configuration will be calculated in order to characterise completely the features of this structure. This will be performed for both polarisations.

Figure 3.25 shows the gap maps for TE and TM modes respectively in the case of dielectric columns with dielectric constant $e_r = 10$. The figure has been performed using 400 plane waves.

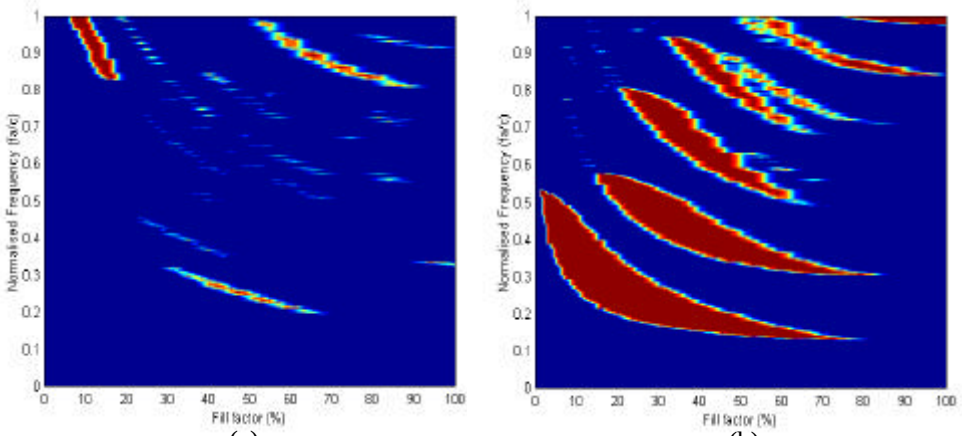

(a) (b)

Figure 3.25: Gap map for TE (a) and TM (b) modes in the case of dielectric columns with $e_r = 10$.

Along the horizontal axis is represented the " *unit cell fill factor*", which is a measurement about how full is with dielectric material or with air the unit cell. In the case of a triangular-hexagonal lattice, this value is defined as,

$$f.f. = \frac{2p}{\sqrt{3}}\left(\frac{r}{a}\right)^2 \tag{3.16}$$

Looking at Figure 3.25, similar characteristics than those for the square lattice are found. TM modes present an evident and wide gap, which is reducing its working frequency when the fill factor is increased and repeating progressively with smaller copies when the frequency is raised. TE modes do not show considerable gaps, only a couple of small minor zones.

The combination of both figures should allow the deter mination of the possible complete gaps. Figure 3.26 shows this feature. Nearly no complete band gap appears, only a couple of small red zones but their significance is negligible.

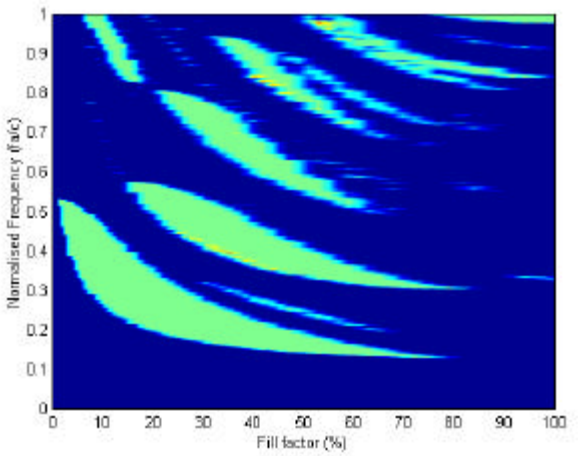

Figure 3.26: Gap map for TE and TM modes in the case of dielectric columns with $e_r = 10$.

3.2.4.5 A triangular-hexagonal air columns Photonic Crystal

In this section the opposite case will be analysed, a triangular-hexagonal lattice of air columns embedded in a dielectric substrate (see Figure 3.27). As it has been done up to now, the simple dispersion diagram will be calculated in order to get the eigenvalues and eigenvectors from different modes and check the behaviour of this structure.

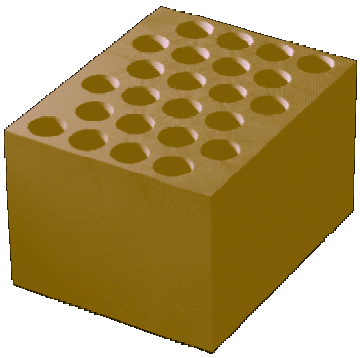

Figure 3.27: Two-dimensional Photonic Crystal formed by air columns in a dielectric substrate.

Figure 3.28 shows this energy bands for a case with parameters $r/a = 0.47$ and dielectric constant $e_r = 10$. A total of 400 plane waves were introduced in the code to perform the analysis. In this case a complete photonic band gap for both polarisations TE and TM have been found.

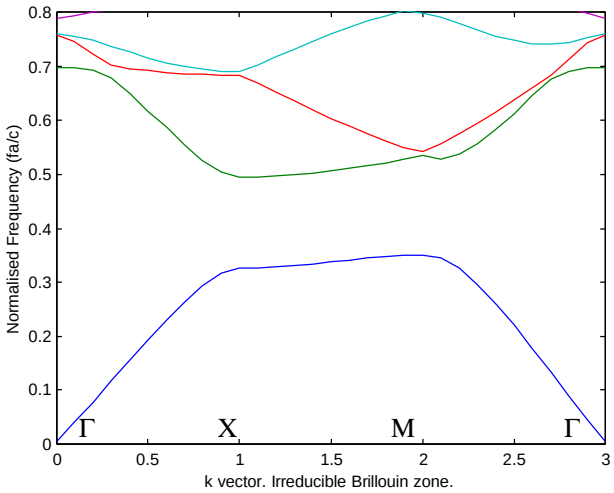

Figure 3.28: Dispersion relation diagram for TE (solid lines) and TM (dashed lines) modes for a triangular-hexagonal lattice of air columns. TE mode solid lines and TM modes dashed lines. The design parameters are $r/a = 0.47$ and $e_r = 10$.

Once the energy bands representing the eigenvalues have been determined and analysed, the representation of the field structures of the modes using the eigenvectors will be carried out. As it was established before, the eigenvectors correspond with the $\vec{H}$ field and the $\vec{D}$ displacement field can be obtained as,

$$\vec{D} = \frac{1}{jw_p} \nabla \times \vec{H} \tag{3.16}$$

being w_p the corresponding eigenvalue for each particular mode in each k-direction.

Any direction of propagation in the Brillouin zone can be selected for this representation, each point will correspond to a different mode. By taking the M point the $\vec{D}$ field distribution is as Figure 3.29 shows. In both cases two periods

have been drawn. The length of the period has been normalised to the lattice value *a*.

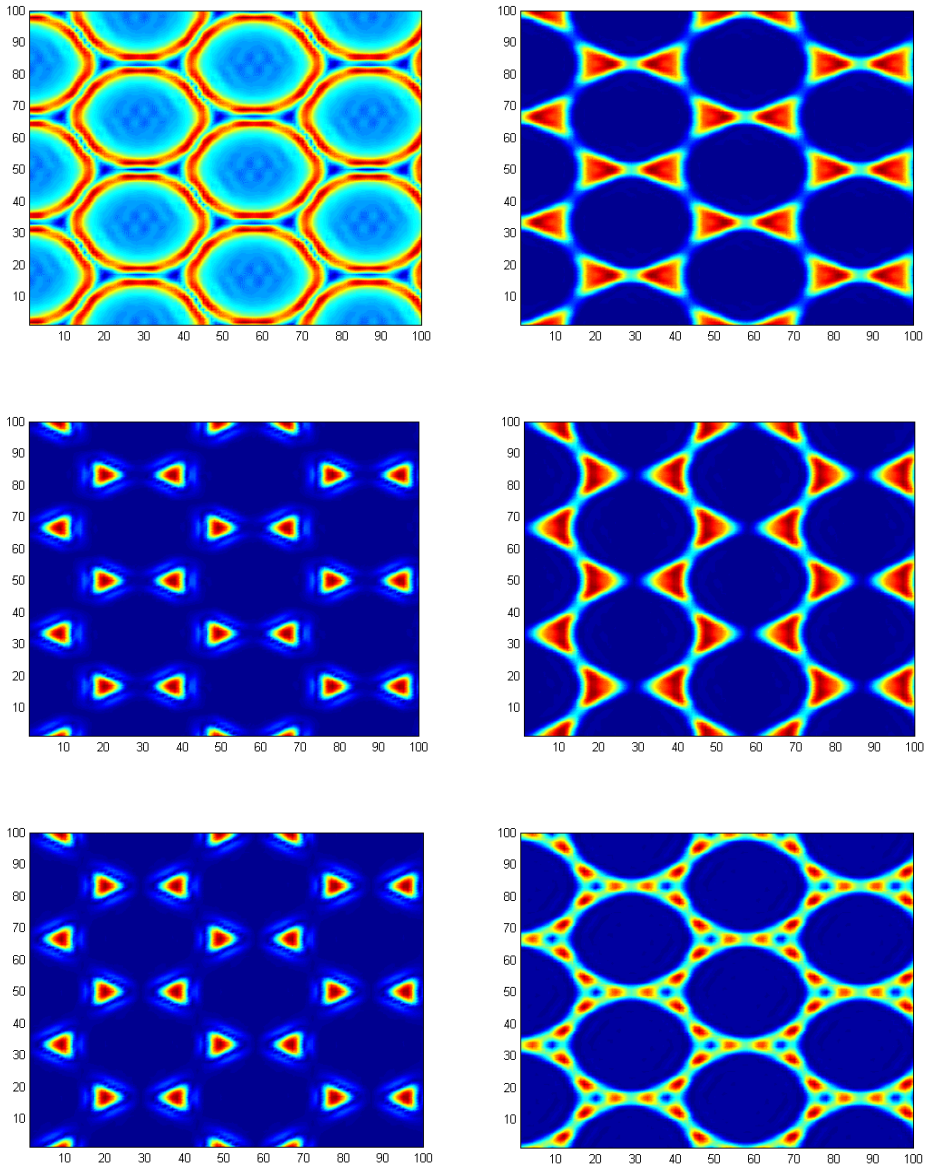

Figure 3.29: $\vec{D}$ field structure for TM (left side) and TE (right side) modes. By descending order, the first, the second and the third mode are plotted. Each picture shows two periods of the unit cell.

Note that using $\vec{D}$ field what it has been called TE and TM polarisations up to now are interchanged (see equation 3.11).

If the TE polarisation plots in Figure 3.29 are evaluated, it is found out that the two first modes are of similar appearance, this means that their field distribution is analogous. However, there is a considerable difference with the shape of the third mode. Its field distribution is quite different. Looking at Figure 3.28, it can be observed that for the corresponding TM polarisation, the two first modes have approximately the same eigenvalues while a big jump appears with the third one giving a clear band gap.

Checking the reverse polarisation, the same behaviour is found out. A clear change in the field distribution between the first and second modes but quite close between the second and third modes. With this remarkable demonstration, it is concluded that the appearance of the band gap is directly related to the field distribution as it was explained before.

The next step to continue with the study of this Photonic Crystal will be the calculation of the Gap Map for this structure. The results of this analysis can be seen in Figure 3.30. The gap map has been performed using 400 plane waves.

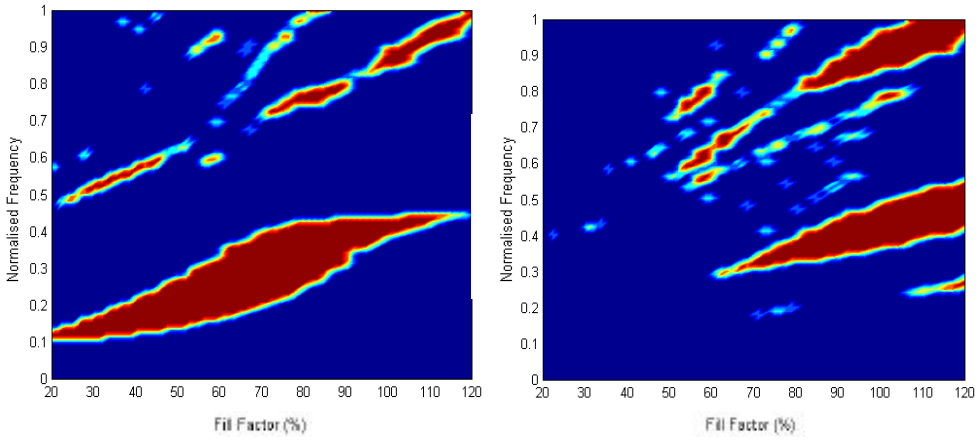

(a) (b)

Figure 3.30: Gap Map for TE (a) and TM (b) modes in the case of air columns embedded in a dielectric substrate with $e_r = 10$.

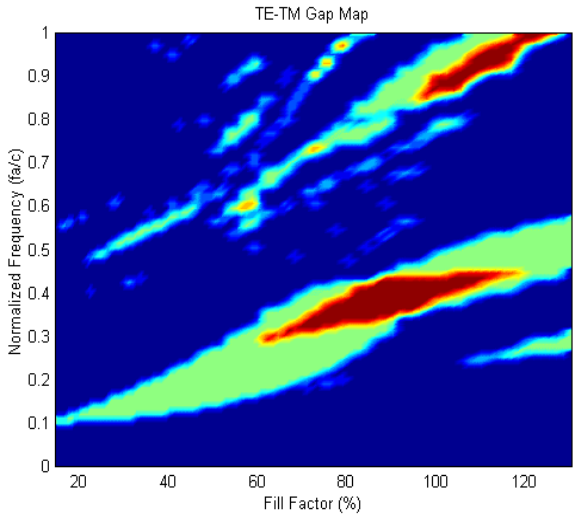

Figure 3.31: Gap Map for the composition of TE-TM modes in the case of air columns embedded in a dielectric substrate with $e_r = 10$. Red zones show the complete band gap.

In this case the gaps for both polarisations are comparable, the structure affects equally TE and TM modes, and this gives rise to a complete photonic band gap (see Figure 3.31). This is centred on a fill factor of 86%, corresponding to a ratio $r/a = 0.49$, extending from 70% to 110%. The appearance of another full band gap is reported for higher frequencies, close to a normalised frequency of 0.9.

From all the studied cases, this is the case that presents a clearer complete band gap. Due to this, the case has been selected to perform an analysis that it has not been carried out up to now: the relation between the dielectric constant value and the appearance of a band gap.

For a fixed ratio of $r/a = 0.47$, the behaviour of this Photonic Crystal as a function of the dielectric constant has been analysed [GON 99c]. The obtained gap maps using 400 plane waves are shown in Figure 3.32. As it will be shown later on, the number of plane waves has to be checked in order to guarantee the convergence for high dielectric constant.

Several band gaps can be observed for both polarisations (TE and TM). The broadest band is obtained for the case of TE modes. Looking at Figures 3.32(a) and (b), it is noted that a minimum value of dielectric constant around 6 is necessary in order to guarantee the existence of a band gap. As it was expected, the frequency response shows a decrease of the band gap when the dielectric constant

is increased (frequency scales with $1/\sqrt{e}$). This will be a general rule, which is translated into a reduction in the size of the final design of any Photonic Crystal structure.

As other authors already defined it [JOA 95], the relative bandwidth of a photonic band gap can be characterised by its gap- midgap ratio, $\frac{\Delta w}{w_0}$. If the system is scaled up or down, all the frequencies scale accordingly, but this quantity stays the same.

A combination of TE and TM polarisation gap map plots can be seen in Figure 3.33, where the existence of several full 2-D gaps becomes clear and the largest bandwidth gap is obtained for the lowest band of gaps as function of normalised frequency.

Using the previous definition, the total bandwidth for the lowest band gap in terms of the dielectric constant has been evaluated, and the results are shown in Figure 3.34. In this figure also it can be seen that the bandwidth for TE polarisation is much larger than that for TM one; therefore, the structure bandwidth, taking into account both polarisations, is completely limited by the value of the bandwidth for TM polarisation. It is also noteworthy that the total Photonic Crystal bandwidth rises when the dielectric constant is increased. This is relevant for some applications, since it is possible to reduce the total device size while obtaining broader operational bandwidths.

As it was commented earlier, an analysis of the solution accuracy with respect to the number of plane waves considered in the computation has been carried out. The results, which are shown in Figure 3.35, reveal that in the range of relative permitivity values up to 25, a small number of plane waves is required; thus, reducing the total calculation time. For larger relative dielectric constants but below 200, an amount of 400 plane waves is judged to be sufficient. Experience with different analysis runs shows that an insufficient plane wave number produces an underestimation/overestimation for the TE/TM polarisations respectively (see Figure 3.36).

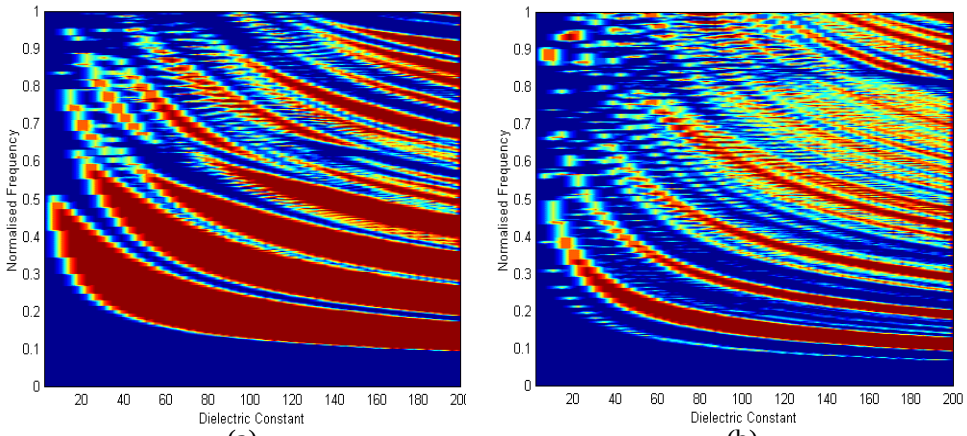

(a) (b)

Figure 3.32: Gap map showing the behaviour of TE (a) and TM (b) polarisations with $r/a = 0.47$ for a sweep in the dielectric constant value.

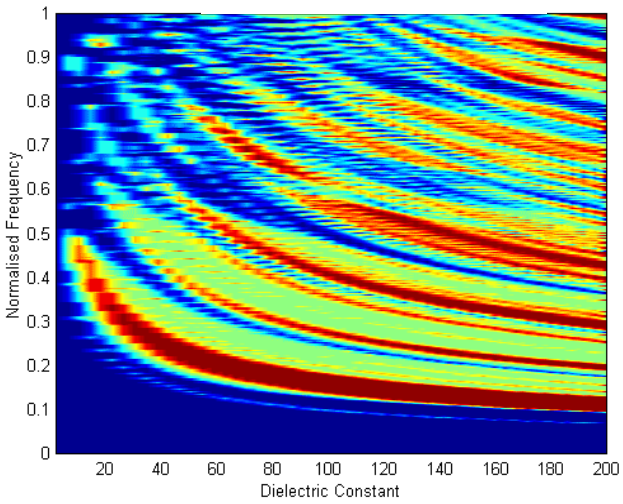

Figure 3.33: Gap map with the behaviour of TE -TM polarisations with $r/a = 0.47$ for a sweep in the dielectric constant value.

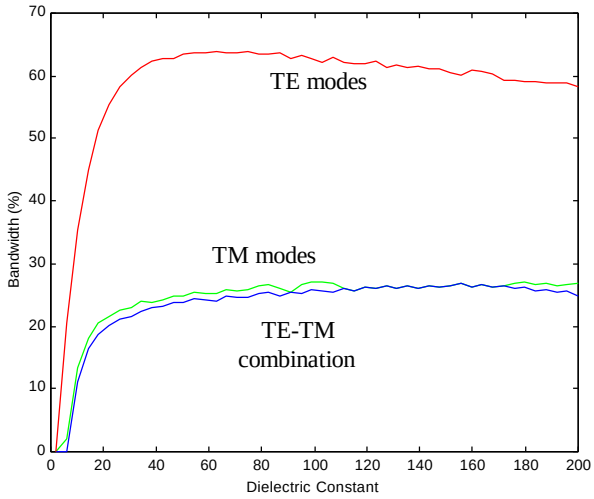

Figure 3.34: Gap-midgap ratio for a triangular-hexagonal lattice of air columns with $r/a = 0.47$ when the dielectric constant is varied.

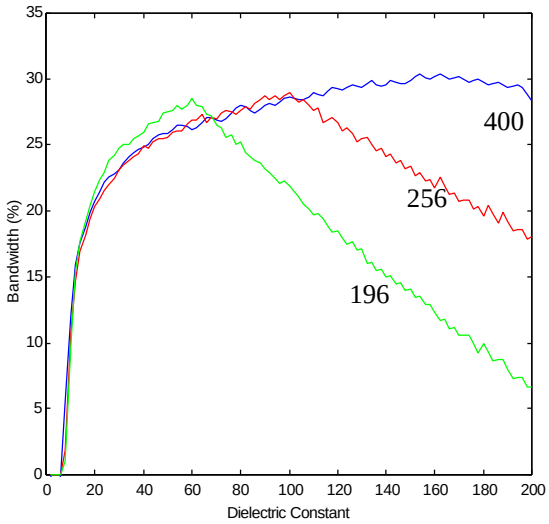

Figure 3.35: Bandwidth for TE -TM polarisations together. The considered number of plane waves has been 196 (green line), 256 (red line) and 400 (blue line).

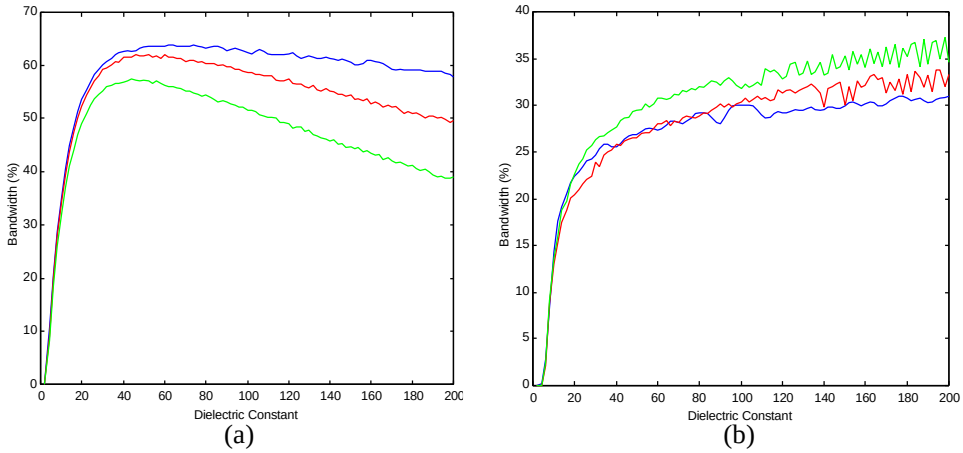

Figure 3.36: Bandwidth for TE (a) and TM (b) polarisations. The analysed numbers of plane waves are 196 (green line), 256 (red line) and 400 (blue line).

3.3 Three-dimensional Photonic Crystal

The electromagnetic analogue of an ordinary crystal is a three-dimensional Photonic Crystal, a dielectric that is periodic along three different axes. These structures present the same novel properties that have been shown up to now in previous sections. But now, the propagation will be prohibited for all possible direction in the *k*-space, in the three-dimensions.

There are many possible geometries for a three-dimensional Photonic Crystal. Some of them are coming from the crystallography field, as the simple cubic centred structure [SUZ 95], the face centred cubic [YAB 89 and SUZ 95b] or the diamond structure [HO 90]. Others are new arrangements of the atoms in a new cell to design novel structures with new properties, as the layer by layer [HO 94] or woodpile [SOZ 94] structure, the Yablonovite structure [YAB 91] or the three-dimensional structure presented in [FAN 94].

These structures are the most promising because the suppression of wave propagation is obtained for any *k*-direction inside the Photonic Crystal. It should be noted that the analysis of this three-dimensional Photonic Crystal is much more complex than the previous cases. Now, the determination of the primitive vectors is a very difficult and tricky task. As general rule, any three-dimensional structure can be referred to one of the crystallography systems.

Once the unit cell has been determined by the primitive lattice vectors, finding the rest of parameters needed to analyse the structure is straightforward. The only consideration that is necessary to take into account is that for the three-dimensional case the number of plane waves to include in the analysis is increased substantially. There are mainly two reasons for this increase: one is due to the new dimension added, and the other is to assure convergence for lower modes. This is automatically translated into more calculation time.

In this section, only a couple of three-dimensional Photonic Crystals will be analysed. Namely, the woodpile structure, which will be used in Chapter 5, and a novel structure [DEM 99a] which exhibits the features of a three-dimensional one formed by the combination of two-dimensional and one-dimensional Photonic Crystal structures.

3.3.1 Electromagnetic fields

In the two-dimensional Photonic Crystal case, it was relatively simple to split the main equation in two different polarisations (TE and TM modes).

However, the three-dim ensional case is different, it is found out that it is not possible to separate the main equation in two others corresponding to TE and TM polarisations. This is due to the cross product between the two vectors that are defining the field polarisation being different from zero.

$$-\hat{e}_2(k+G)\cdot\hat{e}_1(k+G')\neq 0 \tag{3.17}$$

$$-\hat{e}_1(k+G)\cdot\hat{e}_2(k+G')\neq 0 \tag{3.18}$$

This basically means that there is interaction between both polarisations which can not be neglected and has to be taken into account in the analysis.

In general, what some authors do anyway it is to divide the final solution into TE and TM polarisations by looking at the different field components, however, these are not pure TE or TM polarisations, there remain some field components corresponding to the other polarisation [HO 90].

The dispersion diagram that will be obtained in this work after analysing the Photonic Crystal behaviour will show the eigenvalues without separating into TE or TM polarisations [GON 98c].

The eigensystem to be solved for thi s case is defined by the following equation,

$$\sum_{G'} |k+G\|k+G'|h_{G-G'} \begin{bmatrix} \hat{e}_2(k+G)\cdot\hat{e}_2(k+G') & -\hat{e}_2(k+G)\cdot\hat{e}_1(k+G') \\ -\hat{e}_1(k+G)\cdot\hat{e}_2(k+G') & -\hat{e}_1(k+G)\cdot\hat{e}_1(k+G') \end{bmatrix}$$
$$\begin{pmatrix} h_{n,1}(k+G') \\ h_{n,2}(k+G') \end{pmatrix} = -\frac{w^2{}_{n,k}}{c^2} \begin{pmatrix} h_{n,1}(k+G) \\ h_{n,2}(k+G) \end{pmatrix} \tag{3.19}$$

3.3.2 Woodpile Structure Analysis

An elegant solution for a three-dimensional Photonic Crystal is the woodpile structure proposed by Iowa State University Group [HO 94] and Dowling [SOZ 94] practically at the same time. This structure combines the ease of manufacturing, together with the advantage of being able to place on top an antenna, such as a dipole, double dipole, etc. This is the main reason to analyse the features of this structure because it will be employed in Chapter 5 as substrate for antenna applications.

The structure consists of layers of dielectric rods with each layer consisting of parallel rods having a centre to centre separation of *a*. The rods are rotated by 90° in each successive layer. Starting at any reference layer, the rods of every neighbouring layer are parallel to the reference layer but shifted by a distance of *0.5a* perpendicular to the rod/bar axis. The stacking sequence is repeated every four layers (see Figures 3.37 and 3.38). Square or rectangular bars can replace rods.

As it was done in all the previous cases, the definition of the main parameters (direct lattice, primitive lattice and Brillouin zone) of this structure will be given.

3.3.2.1 Primitive lattice

This case is more complicated than the previous ones, and presents more problems to define correctly the unit cell. The primitive lattice vector that defines the woodpile can be written as,

$$\begin{aligned}\hat{a}_1 &= a\hat{x} \\ \hat{a}_2 &= a\hat{y} \\ \hat{a}_3 &= \frac{a}{2}\left(\hat{x}+\hat{y}+c\hat{z}\right)\end{aligned} \tag{3.20}$$

where a is the normalised unit cell size and c defines the high of the unit cell.

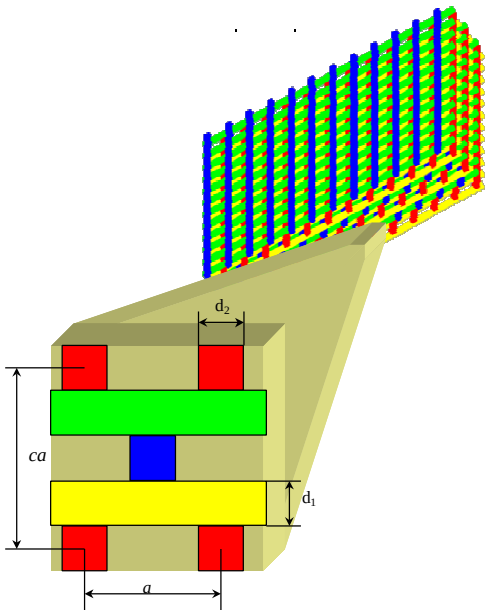

Figure 3.37: Three-dimensional view of the Woodpile structure.

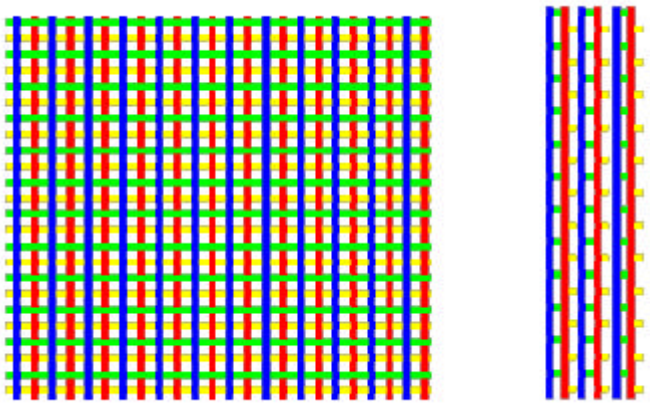

Figure 3.38: Top (a) and Side (b) view of the Woodpile structure.

3.3.2.2 Reciprocal Lattice

With the definition of the primitive lattice vectors the reciprocal lattice vector can be obtained directly resulting in the following expressions,

$$\begin{aligned} \hat{b}_1 &= \frac{2p}{a}\left(\hat{x} - \frac{1}{c}\hat{z}\right) \\ \hat{b}_2 &= \frac{2p}{a}\left(\hat{y} - \frac{1}{c}\hat{z}\right) \\ \hat{b}_3 &= \frac{2p}{a}\left(\frac{2}{c}\hat{z}\right) \end{aligned} \tag{3.21}$$

3.3.2.3 Brillouin Zone

Identification of the Brillouin zone parameters is a difficult task in the woodpile structure for its shape depends on the unit cell thickness, and for the arduous work involved in describing the Irreducible Brillouin Zone.

Figure 3.39 shows a possible Brillouin zone, whose shape will depend on the selected parameters, and will remain quite similar to the one shown in that figure.

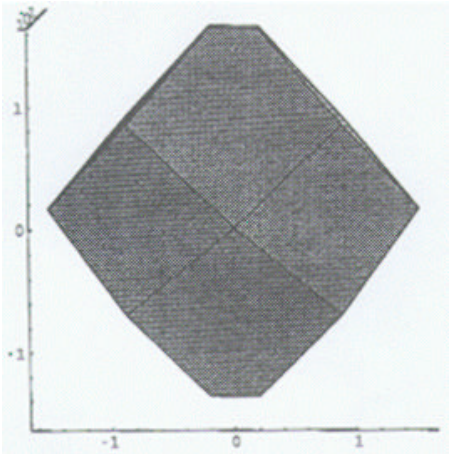

Figure 3.39: Brillouin Zone for the selected case of the Woodpile structure.

Using the symmetries of the structure, the irreducible Brillouin zone goes through the path, defined for the following directions in the k-space; $k_\Gamma = (0,0,0)$, $k_L = \left(\frac{p}{a},\frac{p}{a},0\right)$, $k_M = \left(\frac{p}{a},\frac{p}{a},\frac{p}{ca}\right)$, $k_X = \left(\frac{c^2-1}{c^2}\frac{p}{a},\frac{c^2-1}{c^2}\frac{p}{a},\frac{2p}{ca}\right)$, $k_R = \left(0,0,\frac{2p}{ca}\right)$, $k_Z = \left(0,\frac{c^2+1}{c^2}\frac{p}{a},0\right)$ and $k_P = \left(0,\frac{c^2-1}{c^2}\frac{p}{a},\frac{2p}{c^2 a}\right)$. Note that the selected nomenclature for the k-points does not follow any specific notation.

3.3.2.4 Analysis Results of the parametric variations

In this section a quite complete analysis of this structure will be presented, but only for the case of dielectric rods in air. Initially and looking at Figure 3.37, there are three important parameters to be changed in the geometry of this structure, in addition to the variation of the dielectric contrast. Only variations in the structural geometry will be performed keeping the rods rectangular for all calculations. All the bars will touch each other without air gaps. This will fix the d_1 value in Figure 3.37 to be equal to $d_1 = ca/4$.

Specifically, the first analysis will consist on a sweep for different thickness (c parameter) maintaining the rods square ($d_1 = d_2$). After determining the value which defines the maximum bandwidth, a sweep changing the bars aspect (the height d_1 is fixed by the total thickness of the unit cell but the width, d_2 can be changed) will be carried out. The results of this analysis are shown in Figure 3.40. The dielectric constant of the bars was fixed to 11.9.

The dispersion relation for a particular case is shown in Figure 3.41. This case was selected to perform a comparison with the results presented in [OZB 94c]. The configuration has a centre-to-centre distance , a, a bar width of $d_2 = 0.2128a$, a bar thickness of $d_1 = 0.4256a$ and a dielectric constant of 11.7. The analysis has been performed using 3456 plane waves.

The measured results presented in that paper state that for normal incidence the gap goes from 370 to 520 GHz. With the diagram shown in Figure 3.41, and knowing that $a = 235mm$, a gap from 387 to 533 GHz was found out for normal incidence (point R in the k-space). Besides, the total gap calculated in the paper goes from 425 to 518 GHz versus 413 to 498 GHz obtained in the diagram of Figure 3.41.

The results are in good agreement, the small discrepancy can be explained due to the number of plane waves used for the calculation or the dielectric constant value employed in the calculations, because it is not clear specified in the paper, but the difference is less than 5%.

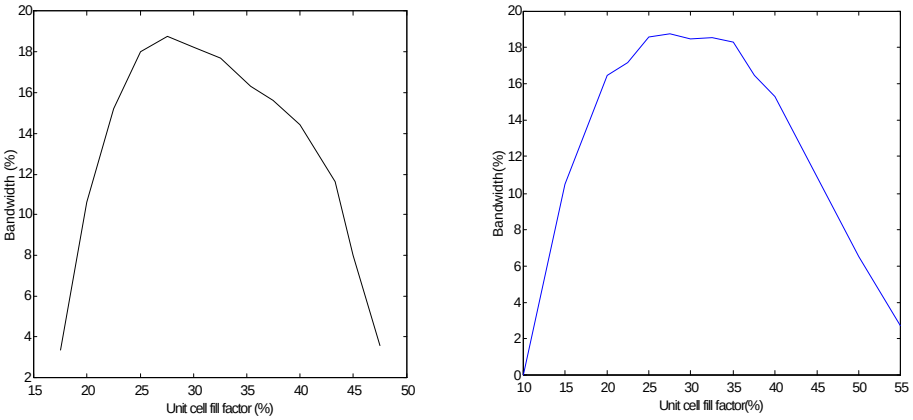

(a) (b)

Figure 3.40: Bandwidth of the woodpile structure as function of the unit cell fill factor. (a) For all the cases, the bars remain square changing the length of their side at the same time that the thickness of the unit cell (*c*) to maintain bar contact. (b) The width of the bars (d_2) is changed but the thickness remains constant ($c=1.1a$; $d_1=0.275a$).

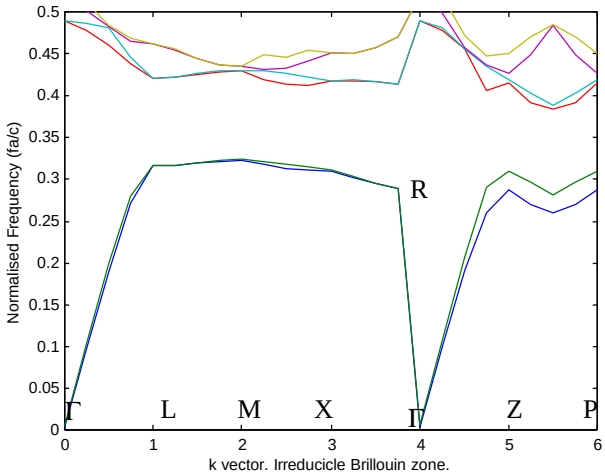

Figure 3.41: Dispersion relation diagram for the woodpile structure for $d_1 = 0.4256a$, $d_2 = 0.2128a$ and $e_r = 11.9$.

3.3.3 3-D Photonic Crystal by stacking 2-D patterned dielectric layers

In this section, a novel three-dimensional Photonic Crystal structure is proposed, which presents a complete three-dimensional band gap for any direction of propagation in the *k*-space. The principal idea is to stack two dimensionally patterned dielectric layers to produce a complete three-dimensional gap. The Photonic Crystal behaviour will be confirmed by plane-wave analysis.

The two-dimensional structures that have been analysed up to now have the advantage that they are quite easy to manufacture. Nevertheless, although such two-dimensional structures could be useful, a three-dimensional Photonic Crystal seems most appropriate. At least, when it is going to be used as a substrate for antennas because an antenna fundamentally radiates in 3-D and consequently a full three-dimensional band gap (covering all radiation directions) will be preferred.

Some configurations, showing three-dimensional performances have already been proposed in literature and commented previously, but these seem to suffer from either a complex manufacturing process or from fragility problems.

The novel structure that is proposed here [DEM 99a] combines the ease of manufacturing of a two-dimensional structure with the performance of a full three-dimensional Photonic Crystal. The innovative idea is to combine a 2-D with a 1-D configuration in order to obtain 3-D performance.

The one-dimensional structure is essentially a layered structure made of a material, having certain dielectric constant and, at least, another layer of a different dielectric constant (see Figure 3.42a). The number of layers can vary as function of the desired features. The dielectric contrast between the different layers should be sufficient to provide a band gap.

Once the one-dimensional structure is fabricated, an array of holes constituting a two-dimensional lattice has to be formed into the one-dimensional structure in order to get the performance of a three-dimensional structure. The layout of the holes can be square, triangular, hexagonal, etc. The holes go through the complete one-dimensional structure (see Figure 3.42b). Air holes are preferred in order to provide the desired large dielectric contrast between the different materials.

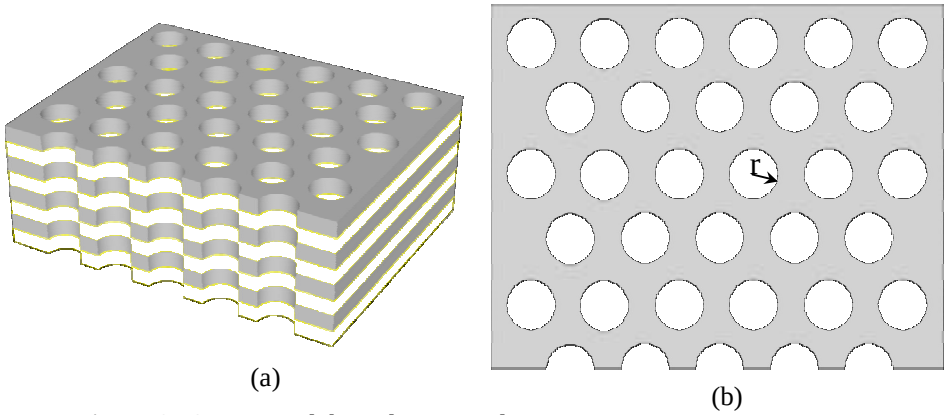

(a) (b)

Figure 3.42: Proposed three-dimensional structure.

The one-dimensional structure can be fabricated by different techniques, e.g. growing layer by layer, depositing or gluing layers of different material. The two-dimensional configuration can be obtained by simple drilling, photolithography, active ion etching, micromachining, etc, depending on the desired operating frequency (from microwave to optical frequencies).

The design of the structure has many degrees of freedom, which can be used to optimise the size of the band gap, depending of the layout of the holes as well as the materials used to form the stacks. This structure is naturally robust and the manufacturing process is very simple.

Now, the analysis of this structure will be performed. The selected two-dimensional structure will be a hexagonal arrangement of holes in a one-dimensional structure formed by two different layers of dielectric constant. But any other two-dimensional pattern could be employed. First of all the definition of the main unit cell parameter will be performed.

3.3.3.1 Primitive lattice

For this structure, the definition of the vector in the direct l attice is quite easy because will be the combination of the one-dimensional and the two-dimensional triangular-hexagonal lattices. These vectors can be written as,

$$\begin{aligned}\hat{a}_1 &= \frac{a}{2}\left(\hat{x} + \sqrt{3}\cdot\hat{y}\right)\\ \hat{a}_2 &= \frac{a}{2}\left(\hat{x} - \sqrt{3}\cdot\hat{y}\right)\\ \hat{a}_3 &= a\left(c\hat{z}\right)\end{aligned} \tag{3.22}$$

where a is the normalised unit cell size and c defines the high of the layers in relation with the unit cell size.

3.3.3.2 Reciprocal Lattice

With the definition of the primitive lattice vectors the reciprocal lattice vector can be obtained directly resulting in the following expressions,

$$\begin{aligned}\hat{b}_1 &= \frac{2p}{a}\left(\hat{x} + \frac{1}{\sqrt{3}}\hat{y}\right)\\ \hat{b}_2 &= \frac{2p}{a}\left(\hat{x} - \frac{1}{\sqrt{3}}\hat{y}\right)\\ \hat{b}_3 &= \frac{2p}{a}\left(\frac{1}{c}\hat{z}\right)\end{aligned} \tag{3.23}$$

3.3.3.3 Brillouin Zone

The Brillouin zone of this two-dimensional structure has already been depicted in Figure 3.22. It has an hexagon shape. Taking into account that the structure is three-dimensional with a constant value in k_z-direction, the Brillouin zone can be plotted as in Figure 3.43(a). By using the symmetry properties, it is only necessary to analyse a part of the whole Brillouin zone , this one is called irreducible Brillouin zone. In this case, the result is shown in Figure 3.43(b).

The k vector components for the R point in Figure 3.43(b) are defined by,

$$k_x = \frac{2p}{a}\frac{1}{3}$$
$$k_y = \frac{2p}{a}\frac{1}{\sqrt{3}} \qquad (3.24)$$
$$k_z = \frac{p}{a}$$

By performing a sweep from Γ to *R* point via X and M points, a completed analysis of the irreducible Brillouin zone will have been provided.

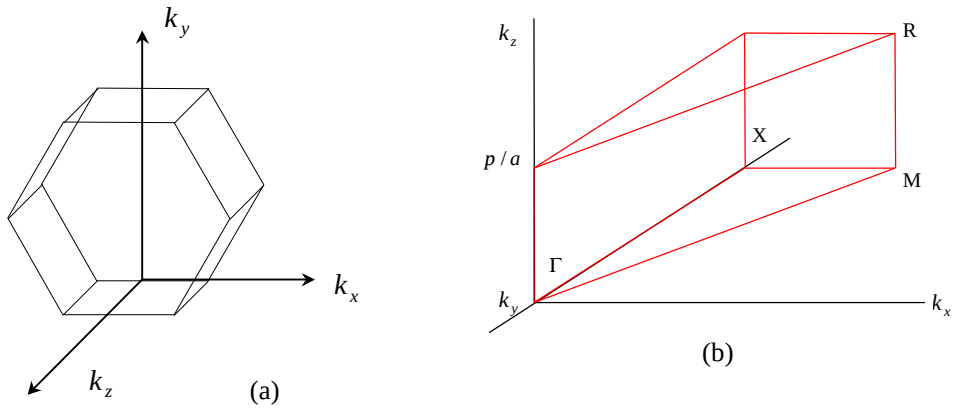

Figure 3.43: Brillouin zone (a) and Irreducible Brillouin zone (b) for this three-dimensional Photonic Crystal structure.

3.3.3.4 Analysis Results of the parametric variations

In this section, the analysis of one of the possible structures designed to exhibit a complete gap is presented. The selected values to simulate the behaviour of this novel structure have been two different layers of $e_{r_1} = 2.1$ and $e_{r_2} = 70$ with thickness $a/2$, forming the one-dimensional part of the crystal. The two-dimensional part will be a triangular array of holes with the ratio $r/a = 0.45$. The size of the lattice (a) will be normalised. The high dielectric contrast has been chosen to improve the three-dimensional performance of the crystal.

Figure 3.44 shows the band structure result for the analysed Photonic Crystal taking into account 3456 plane waves. Several band gaps can be visualised

in the plot, where the total bandwidth obtained is approximately 3%. It should be clear that the performance could be optimised by adjusting the r/a ratio, the values of the dielectric constant of the layers, the number of layer or the thickness of each layer.

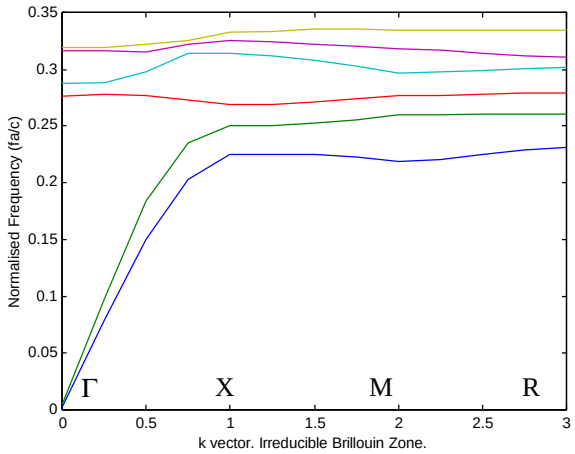

Figure 3.44: Projected dispersion relation for the novel Photonic Crystal. The dielectric constants of the one-dimensional layers are $e_{r_1} = 2.1$ and $e_{r_2} = 70$. The thickness of each layer is $a/2$ and the two-dimensional pattern is a triangular lattice with $r/a = 0.45$.

Performing an analysis of the bandwidth as a function of the dielectric contrast, the results presented in Table 3.4 were found. In all cases the ratio between the radius of the hole and the lattice size was fixed to 0.45 and the value of the dielectric constant of one of the dielectric layers was fixed to $e_{r_1} = 2.1$ in order to increase the dielectric contrast.

e_{r_2}	Bandwidth (%)
10	0
50	0
60	0.82
70	2.5
100	4.2

Table 3.4: Bandwidth values as function of the dielectric contrast.

It is important to note that although the bandwidths is not too large, the ease of manufacture and the possibility to obtain more gaps for different crystal parameters give this structure promising applications in the near future.

CHAPTER 4

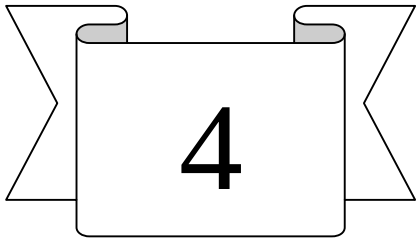

PHOTONIC CRYSTAL STRUCTURES AS SUBSTRATES IN PATCH ANTENNA CONFIGURATIONS

The previous chapters have been concerned with the electromagnetic theory related to Photonic Crystal structures and with the theoretical modelling of one, two and three-dimensional configurations.

This chapter will deal with one application of Photonic Crystal structures in the microwave or millimetre wave ranges which it is based on using these structures as substrate for microstrip patch antennas. A drawback of conventional antennas on a semi-infinite semiconductor substrate (with dielectric constant ε) is that the power radiated into the substrate is a factor $\varepsilon^{3/2}$ larger than the power into the free space [RUT 83]. For the specific case of patch antennas on a microstrip substrate, most of this power is trapped in surface wave modes, which are

propagating at angles larger than the critical angle for the substrate. Because this power does not contribute, as it is desired, to the radiation pattern, it is generally considered as a loss mechanism. This chapter focuses on a single patch antenna on a Photonic Crystal substrate. However, the first steps towards an array configuration have been established.

The chapter will be divided into four sections. In the first one, a brief summary about some concepts of microstrip antennas will be presented. The patch antenna features, advantages and disadvantages of using this configuration and their associated problems that can be solved by using Photonic Crystal substrates will be treated. The second one will deal with the analysis of the Photonic Crystal configuration selected as substrate, which will consist of a square lattice of drilled air holes in a dielectric substrate. The reasons to employ this specific configuration will be explained. Once the Photonic Crystal structure has been selected, the next step will be to apply this configuration to patch antenna configurations. Three patch antenna structures with different feeding techniques have been investigated. Only the results obtained for the feeding case based on the aperture coupling method will be presented. The other cases have already been developed and published in [GON 99a, GON 99b, GON 99d, GON 00a and GON 00b]. Finally and as starting point for array applications, a study about the coupling performances between two patch antennas in a conventional substrate and in a Photonic Crystal substrate have been analysed. The improvements obtained by using the Photonic Crystal configuration will be shown.

4.1 Introduction (Some considerations about microstrip patch antennas)

The first practical microstrip antennas were developed in the early 1970's by Howell [HOW 72] and Munson [MUN 74]. Since then, extensive research and development of microstrip antennas and arrays, exploiting the numerous advantages such as light weight, low volume, low cost, planar configuration, compatibility with integrated circuits, etc., have led to diversified applications and to the establishment of the particular research field.

Various types of flat profile printed antennas have been developed, the microstrip antenna, the stripline slot antenna, the cavity backed printed antenna and the printed dipole antenna. Microstrip antennas can be divided into three basic categories: microstrip patch antennas, microstrip travelling-wave antennas and microstrip slot antennas. The microstrip patch antenna is the selected configuration whose performance will be improved by using Photonic Crystal substrates.

Theoretical considerations about the radiation mechanism, the radiation fields or microstrip antenna calculations are given in [BAH 80, JAM 81, JAM 89 and BAL 97] and they will be not treated in this work. Nevertheless, some comments about different feeding techniques and how the surface wave modes are excited will be briefly given due to their relevance for the developments of this chapter.

A microstrip patch antenna consists of a conducting patch of any planar geometry on one side of a dielectric substrate backed by a ground plane on the other side. The case under study corresponds to a rectangular antenna. A microstrip or a coaxial line may feed the antenna, but in this section only microstrip feeding techniques will be studied.

Matching is usually required between the feeding line and the antenna because the antenna input impedances differ from the normal 50 ohms. The proper selection of the location of the feeding line may achieve the required matching. However, the location of the feed may also affect the radiation characteristics. The most commonly used feeding techniques are based on the microstrip line or the aperture coupling method. Two microstrip line techniques are depicted in Figure 4.1 and the aperture coupling technique in Figure 4.2, respectively.

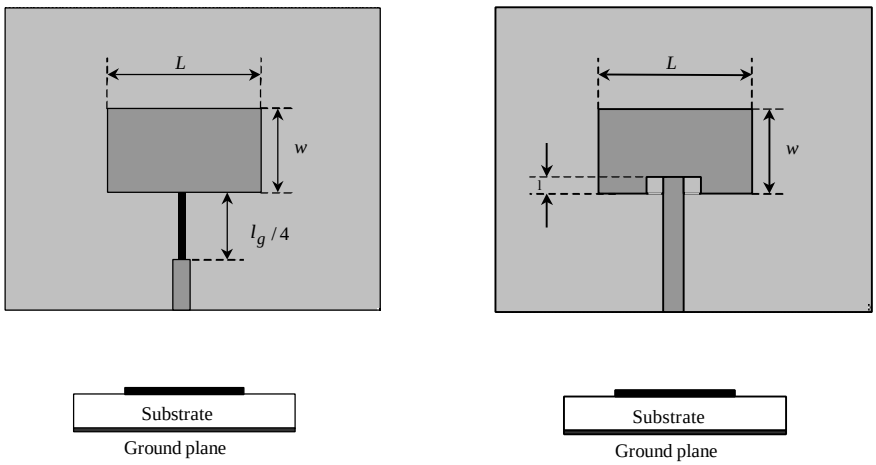

(a) (b)

Figure 4.1: Two different microstrip feeding techniques. In (a), the matching is obtained by using a quarter of wavelength microstrip line and in (b), by controlling the inset position of the microstrip line.

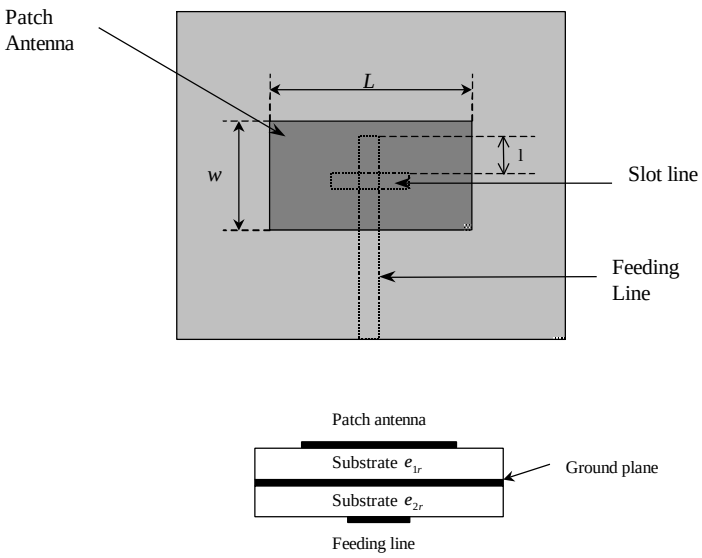

Figure 4.2: A microstrip patch antenna feeds by using the aperture coupling method.

The microstrip feed line is easy to fabricate, simple to match by selecting an appropriate quarter wavelength adapter (Figure 4.1a) or controlling the inset position (Figure 4.1b). However as the substrate thickness increases excitation of surface wave modes and spurious feed radiation increases. The typical bandwidth [BAL 97] for this type is restricted to 2-5%.

The aperture coupling method of Figure 4.2 is more difficult to fabricate and it also has narrow bandwidth. The aperture coupling consists of two substrates separated by a ground plane. On the bottom side of the lower substrate there is a microstrip feed line whose energy is coupled to the patch through a slot on the ground plane separating both substrates. This arrangement allows independent optimisation of the feed mechanism and for the radiating element. This configuration minimises the spurious radiation from the feed to the main radiation pattern coming from the radiating element [BAL 97].

One of the problems, which appears when the thickness of the substrate is increased, is the excitation of surface wave modes. These modes may be excited giving rise to end-fire radiation, and hence must be considered in the design. These waves are either TM or TE modes, which propagate into the substrate outside the microstrip patch (see Figure 4.3). These modes are formed by waves attenuating in the transverse direction (normal to the antenna plane) and waves in propagation.

The analysis of these surface wave modes is presented in Appendix A. The lowest order TM mode has no cut-off frequency, and the corresponding value for higher TE and TM modes is defined by the following expression:

$$f_c = \frac{nc}{4h\sqrt{e_r - 1}} \tag{4.1}$$

where c is the velocity of light in the free space and $n=1,3,5,\ldots$. For TE_n modes and $n=2,4,6,\ldots$ for TM_n modes.

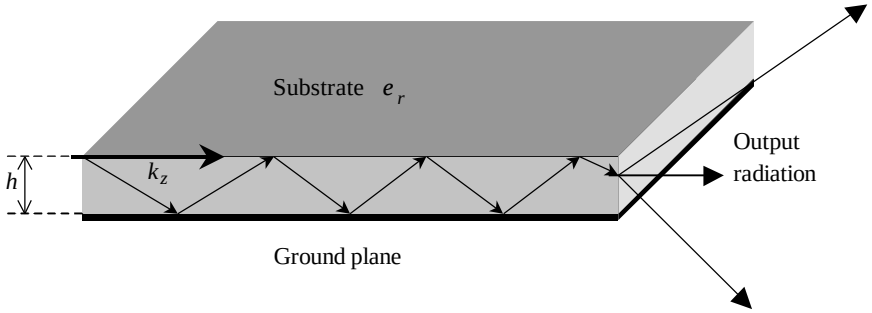

Figure 4.3: Surface wave mode propagation in a dielectric slab.

The excitation of higher order surface wave modes depends on the dielectric constant (e_r) and the thickness (h) of the substrate. If any of these parameters increase, the cut-off frequency of these modes decreases, as it can be seen from equation 4.1.

As the TM_0 mode has no lower cut-off frequency, it will be always excited to some extent at an open-circuited microstrip antenna. It will even propagate on very thin substrates having low dielectric constant values. As a practical rule given in [JAM 79], the surface wave excitation becomes appreciable when $h / l_0 > 0.09$ for $e_r \cong 2.3$ and $h / l_0 > 0.03$ for $e_r \cong 10$. If the above constraints are observed, no significant surface wave problems should be experienced.

In general, thicker substrates could improve the radiation efficiency, conductor losses, bandwidth, and sensitivity to tolerances depending on the substrate relative permittivity. Nevertheless, this leads to an increase of the surface wave mode excitation. Besides, in array configurations, coupling between antennas is favoured by surface wave excitation.

In the next sections a Photonic Crystal substrate, based on the procedures developed in previous chapters, will be proposed as solution to avoid surface wave propagation in the microstrip substrate.

4.2 Photonic Crystal Structure selected as substrate

In this section the analysis of the features of the Photonic Crystal configuration (square lattice of drilled air holes) selected as substrate for patch antenna applications will be presented. The selection of this configuration above other possible configurations will be justified. A thorough theoretical analysis will demonstrate how good a Photonic Crystal can act as a suppresser of surface wave modes.

Due to the natural geometry of the microstrip technology, it seems more appropriate to work with two-dimensional Photonic Crystal structures instead of three-dimensional. The additional reflectivity obtained in the third dimension by using a three-dimensional Photonic Crystal configuration is already guaranteed in microstrip technology by the metallic ground plane. The structures based on drilling a pattern of holes in the dielectric substrate look to be the most appropriate because they are very easy to fabricate, robust and light.

Up to now, all the analysis performed in the previous chapters have assumed that the structure was infinite in all directions. In reality, the structure under consideration is finite. However, applying the developments carried out in [JOH 99], a study of the finite structure in the z-direction can be performed in order to perform a more realistic simulation.

In order to analyse the Photonic Crystal substrate behaviour , it will be considered infinite in the x-y plane and finite in the z-plane, as it is displayed in Figure 4.4a. The properties of this structure, which can be described as a two-dimensionally lattice of air holes embedded in a dielectric material that present a band gap for propagation in the plane and that uses index guiding to confine the electromagnetic field in the third dimension, will be investigated.

The dispersion relations calculated in Chapter 3 for two-dimensional structures assume that the periodic structure is infinitely extended in the third dimension. Therefore, these modes represent electromagnetic waves that have no propagation component in the vertical direction (perpendicular to the plane of periodicity). Applying the restriction of finiteness to the Photonic Crystal microstrip substrate leads to a more accuracy analysis of the structure which takes into account the third dimension.

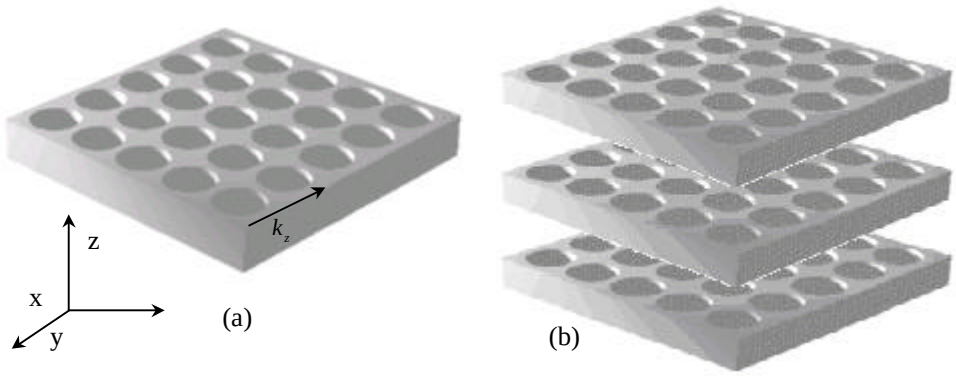

Figure 4.4: Square lattice of air holes embedded in a dielectric substrate which will be implemented in as substrate in microstrip patch antennas. In Figure (a), the propagation direction of the surface wave mode is shown. Figure (b) shows the addition of periodic structures at large intervals.

The computation of the mode structures for the Photonic Crystal substrate is achieved by assuming the substrate as infinite periodic in the x-y plane and repeated in z-direction by a sufficient amount of background region, air in this case (see Figure 4.4b). This leads to perform the analysis of a normal 2-dimensional configuration as it was developed in Chapter 3, but imposing a new lattice vector in the z-direction. Then, the light band is calculated and superimposed to the dispersion relation for the Photonic Crystal substrates. The bands below the light curve will correspond to the guided modes for the Photonic Crystal substrate configuration as described previously. All the bands above the light curve will correspond to non-guided modes.

Due to the fact that guided modes are localised inside the Photonic Crystal substrates the addition of periodic substrates at large intervals will not alter noticeably the frequency behaviour of the resultant dispersion relation. The only modes affected will be the non-guided modes. For these modes, the working frequencies fall above the light band and initially, they will be not important as propagating modes. However, it should be noted that they become important considering the radiation phenomenon.

In Chapter 3, different two-dimensional structures of drilled holes have been studied and any of them could be employed as substrate. Initially, it could seem logical to work with a triangular-hexagonal lattice, due to the fact that it presents a complete gap for TE and TM polarisation. This configuration has

already been employed in [AGI 99 and COL 99]. Nevertheless, the square lattice shows a very important advantage; for the same working frequency, the lattice size is the smallest one. This will lead to a maximum number of periods of the structure per wavelength, which will increase the rejection factor of the surface wave modes (this property will be very useful for array configurations). A clear disadvantage is that this lattice configuration exhibits a gap for TM modes and not for TE. Anyway, in Appendix A, it is shown that only the TM surface wave mode is always in propagation. By, selecting the appropriate microstrip parameters (substrate thickness and dielectric constant) in the design, the propagation of the first TE surface wave mode can be avoided.

Therefore, the final 2-dimensional selected structure will be the square lattice of air columns embedded in a dielectric medium [MEA 93a, BAB 95a and GON 98c], see Figure 4.4. The dielectric material will be taken to have a dielectric constant ε_r=10 and a thickness of 1.27mm. These substrates are commercially available which is desirable for future fabrication.

Before embarking upon the electromagnetic analysis of this Photonic Crystal structure, the primitive lattice vectors, the reciprocal lattice vectors and the Brillouin zone will be redefined (see Chapter 3 for a more detailed explanation). The direct lattice is described by three main vectors, which can be written as:

$$\begin{aligned} \hat{a}_1 &= a \cdot \hat{x} \\ \hat{a}_2 &= a \cdot \hat{y} \\ \hat{a}_3 &= a \cdot a \cdot \hat{z} \end{aligned} \tag{4.2}$$

where a is any lattice size and α is the periodicity factor in z-direction. With the primitive lattice vectors defined, the reciprocal lattice vectors are defined as (see equations 2.4, 2.5 and 2.6):

$$\begin{aligned} \hat{b}_1 &= \frac{2 \cdot p}{a} \hat{x} \\ \hat{b}_2 &= \frac{2 \cdot p}{a} \hat{y} \\ \hat{b}_3 &= \frac{2 \cdot p}{a \cdot a} \hat{z} \end{aligned} \tag{4.3}$$

The irreducible Brillouin zone for the propagation direction in the x-y plane is the triangular wedge formed by these three special points called Γ, X and M which have already been explained in Chapter 3. Sweeping over this zone, all

directions in the *k*-space of the propagating waves will have been taken into account fully characterising the dispersion relation for the Photonic Crystal substrate.

As the Photonic Crystal substrate presents the features of a three-dimensional structure, the modes will not exhibit a pure state of TM and TE polarisations. Some coupling coefficients appear when the eigenvalue equation is solved (see section 3.3.3). The calculation of the dispersion relation for the case of taking into account this coupling between TE and TM polarisations and also for the case of only TM or TE polarisation was performed. As it appears, the coupling factor is negligible because the results for both cases are almost identical (see Figure 4.5) and, hence, the obtained solution by analysing only TM modes can be taken as valid. With this consideration, the computational effort is considerably reduced.

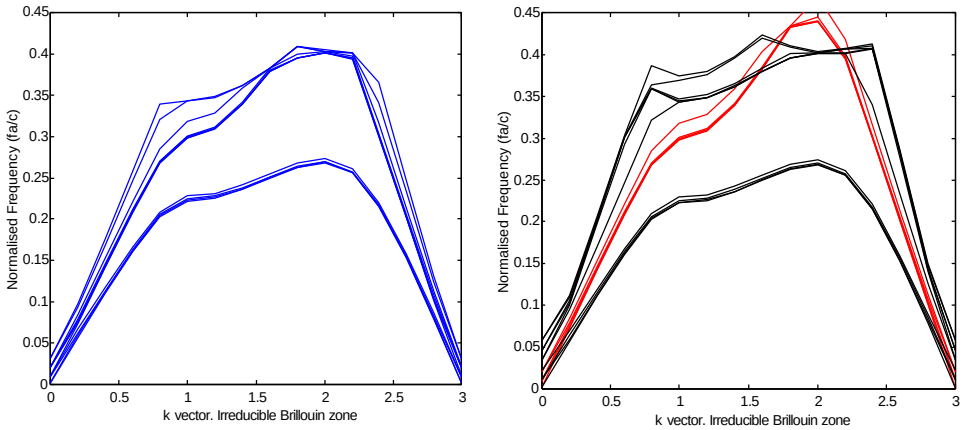

(a) (b)

Figure 4.5: Dispersion diagram for a dielectric slab repeated in the z-direction. (a) Obtained modes for a TE-TM analysis. (b) Black line shows the TM modes and red line the TE modes. A total number of 3456 plane waves were used in the calculations.

The corresponding TM projected band structures for the three-dimensional Photonic Crystal substrate are shown in Figure 4.6. These results have been obtained by using 5488 plane waves. This number could lead to an inaccurate representation of the eigenmodes because the structure under study is quite large. But this is the maximum number of plane waves that can be handled with our computer facilities (a larger number will suppose many days of calculation). Anyway, a comparison between the results presented in [JOH 99] and the obtained by using the equations defined in Chapter 2 do not differ significantly, at least for the lower bands. A comparison is not shown in this dissertation because the

analysed structures are different. Finally, it should be noted that the obtained bandwidth is about 16%.

The difference between this analysis and the one performed in Chapter 2 is found in the use of the light band. Above this line, all the bands correspond to radiating modes, which are generated outside of the Photonic Crystal substrate, below this line, the bands are guided modes, which are localised inside the Photonic Crystal substrate. These last modes decay exponentially into the background region. This behaviour is similar to that produced by total internal reflection case because the guided modes are seeing a higher effective index in the substrate than in the air.

When a band below the light cone (guided mode) just reaches the edge of the light curve, it becomes in a radiated mode, it extents infinitely far into the air and it can not be used as a guided mode.

Looking at Figure 4.6, a band gap for a range of frequencies can be found in which there is no guided mode. But this is not a real gap because there are still radiation modes at those frequencies. For this kind of structures (finite dielectric slabs) it is impossible to obtain a complete band gap. The radiating region becomes in a problem because these radiating modes will be excited contributing to undesired radiation, which will be impossible to avoid in these kind of open structures.

The thickness of the Photonic Crystal substrates plays a very important role to determine whether the structure shows a band gap in its guided modes and its value. A complete study for the cases of a hexagonal lattice of drilled holes in a dielectric medium and a square lattice of dielectric columns embedded in an air medium can be found in [JOH 99]. Here, the bandwidth results as function of the substrate thickness are presented for a square lattice of drilled air holes (see Figure 4.7).

From that study, the selection of the adequate thickness to maximise the band gap could be made. However, the commercial availability of the microstrip substrates will fix the thickness used in the design and analysis in the next sections up to 1.27mm (50mils).

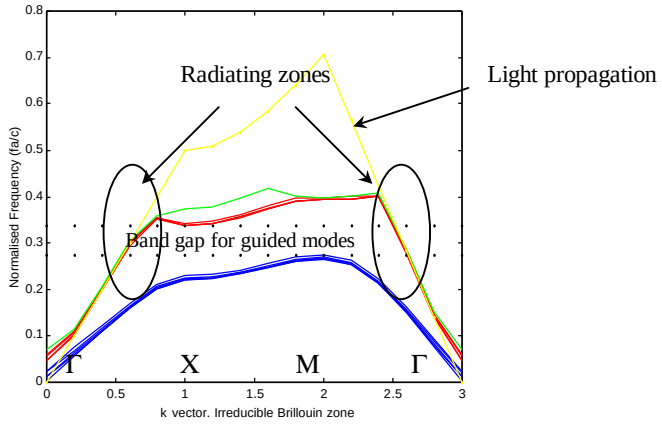

(a)

Figure 4.6: Dispersion relation for TM polarisation in the case of finite substrate thickness. Only the lowest modes are shown .

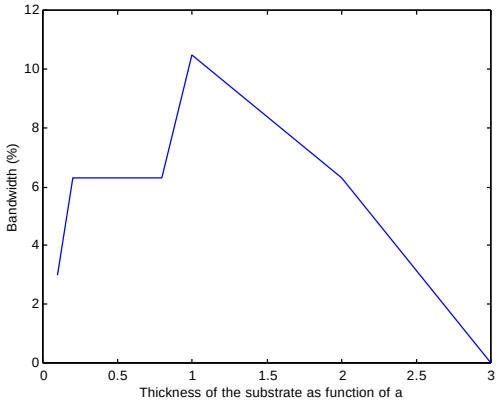

Figure 4.7: Bandwidth of the TM modes for a finite dielectric substrate as function of the thickness.

4.3 Patch Antenna Configuration

This section describes the patch antenna configurations that have been selected to perform the comparison between using a conventional substrate and a Photonic Crystal substrate. Three different patch antenna configurations have been analysed. Each one differs from the other in the feeding technique. Two of them

are based on the microstrip feeding techniques as depicted in Figure 4.1(a) and 4.1(b) and the last one in the aperture coupling method. The two cases based on the microstrip feeding have already analysed and published in [GON 99d and GON 00a], hence they will not be repeated here. Only the study of the antenna with the aperture coupling feeding method will be presented.

This feeding method provides several advantages in relation with other feeding methods; the patch antenna can be completely surrounded by the Photonic Crystal substrate, the fields around the microstrip line are not affected by the Photonic Crystal configuration and the feeding transmission line can be built on a thinner substrate avoiding surface wave effects and its undesired radiation.

In all the cases the dimensions of the substrate will be relatively large compared to the patch antenna size. This has been done to allow a direct comparison of the results, as the input return losses, far field radiation patterns and the surface wave representation, obtained by analysing the conventional patch antenna or the patch antenna on the Photonic Crystal substrate.

To analyse the performance of the patch antenna configurations with the conventional or with the Photonic Crystal substrate, the commercial software package HP-HFSS has been used [5]. The simulation technique used to calculate the full three-dimensional electromagnetic field inside a structure is based on the finite element method. The method divides the full problem space into thousands of smaller regions and represents the field in each sub-region. Convergence and minimisation of errors were obtained in all the studied cases by ensuring that enough iterations were used.

The results obtained under using a conventional substrate will be contrasted with the Photonic Crystal case. Two different cases have been developed. These cases correspond with two Photonic Crystal substrates, one designed for two rows of holes and the other one for three rows of holes around the patch antenna. A comparison between the features of each case is presented.

An aperture coupled patch antenna working at around 14. GHz has been designed. The geometry of the reference patch antenna for both cases is shown in Figure 4.8. The selected rectangular patch antenna has a 4.6mm width and 1.5mm length. The antenna substrate is 1.27mm thick and the microstrip one 0.635mm. The transmission line designed to feed the patch antenna is 0.635 in width and a 2.286mm stub in length from the middle point of the patch antenna to match the input impedance of the antenna. The slot in the ground plane to couple the power from the transmission line to the patch antenna has an H shape. The dielectric

constant is of 10.2 ± 0.2 for both substrates. The antenna will be placed at the central position of the substrate.

Following the indications given in [JAM 79], the surface wave excitation becomes appreciable when the $h/\lambda_0 > 0.03$ for $\varepsilon_r \approx 10$. Applying this approach, for the microstrip substrate, the h/λ_0 ratio has a 0.03 value and for the antenna substrate a 0.06 value. This leads to avoid the surface wave excitation for the microstrip substrate and not for the antenna one as it was desired.

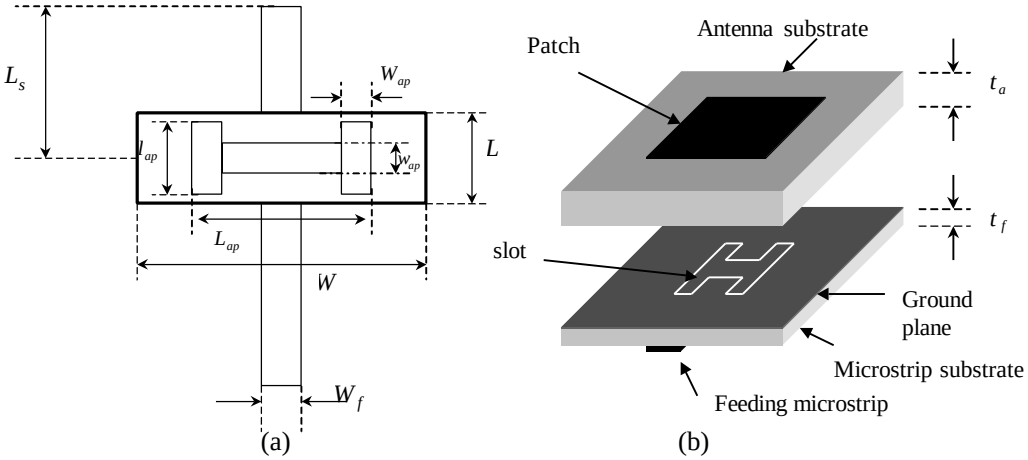

Figure 4.8: Geometry of the reference aperture coupling fed patch antenna. The feeding line is a standard 50- Ω microstrip line on a dielectric substrate with thickness $t_f = 0.635mm$ and a relative permitivity $e_r = 10.2$. Other dimensions are: $W = 4.6mm, L = 1.5mm, L_{ap} = 2.159mm, l_{ap} = 1.143mm, W_{ap} = 0.381mm$, $L_s = 2.286mm$, $w_{ap} = 0.381mm$ and $W_f = 0.635mm$.

4.3.1 Patch antenna in the case of two surrounding rows of holes.

4.3.1.1 Conventional patch antenna

In this case, the selected substrate has a size given by 40x40x1.27mm, which corresponds to the value necessary to form a Photonic Crystal substrate with two rows of holes.

Figure 4.9 shows the calculated return loss (S_{11}) of the patch antenna. The point of resonance corresponds to 14.44 GHz, so this will be fixed as the working frequency. The far field radiation patterns obtained at this frequency are shown in Figure 4.10. The maximum directivity is 5.2 dB. It can be observed that there is an appreciable amount of radiated power along the substrate direction (90 and 270º) and in the back direction (180º) coming from the radiation of the surface wave modes at the edge of the substrate.

The E-plane pattern shows a deeper ripple than the H-plane, which is caused by a stronger excitation of the surface wave modes produced in this plane as it can be seen from Figure 4.11. This figure, which shows the magnitude of the electric field in a transverse cut of the patch antenna at the frequency of operation of 14.44 GHz, plots the propagation of the substrate wave modes, which will contribute to the final radiation pattern from the patch antenna .

The different cuts present the addition of the fields from the surface waves originating at the edges of the substrate with the direct pattern from the patch antenna. In this case this effect can be attributed to the TM_0 surface mode since this mode has no cut-off. Using the equation $f_c = \frac{nc}{4 \cdot h \cdot \sqrt{e-1}}$, defined in Appendix A, where h is the antenna substrate thickness, ε is the substrate dielectric constant and with n=1, the cut-off frequency for the first TE_1 surface mode is 19.7 GHz. This value is safely away from the working frequency, so the assumption that only the TM_0 mode is propagating is justified.

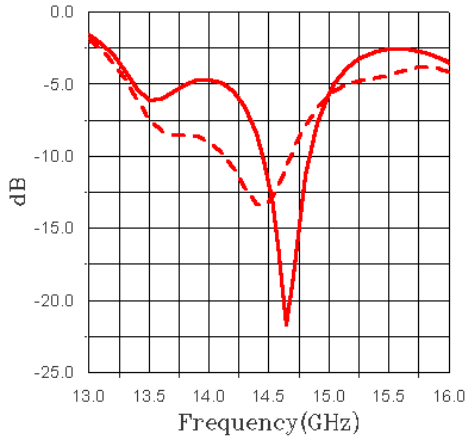

Figure 4.9: Computed input return loss (S_{11}) for the conventional patch antenna (dashed line) and Photonic Crystal antenna (solid line).

4.3.1.2 Patch antenna on a Photonic Crystal substrate

Now, the results obtained from the patch antenna on the Photonic Crystal structure will be shown. Knowing that the working frequency of the conventional patch antenna is 14.44 GHz, the design of the Photonic Crystal substrate can be performed. Using the dispersion relation from Figure 4.6(a) and fixing as normalised working frequency 0.32, the lattice size for the Photonic Crystal structure was found to be 6.53mm and the column radius 3.14mm.

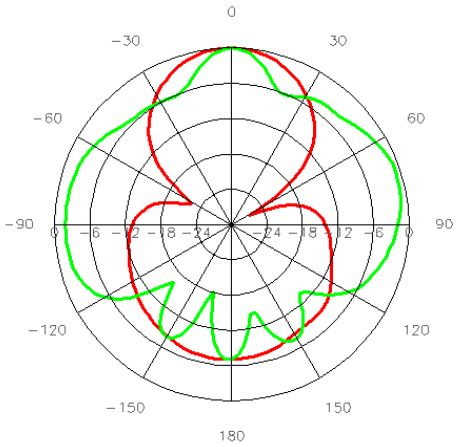

Figure 4.10: Radiation patterns for E (green line) and H (red line) planes at 14.44 GHz for the conventional patch antenna. Maximum directivity is 5.2 dB.

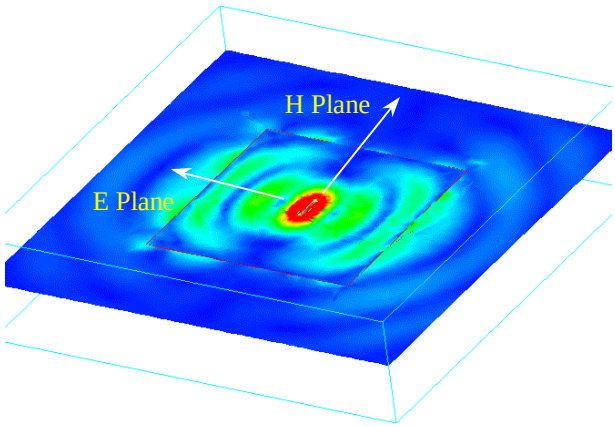

Figure 4.11: Surface plot of the Electric field magnitude for the conventional patch antenna. The scale of colours goes from red (maximum) to dark blue (minimum).

Figure 4.12 shows the structure to be studied , two columns of holes have been added in order to suppress the surface wave mode. The calculated input return loss for this design has already been plotted in Figure 4.9. The resonance frequency has shifted to 14.64 GHz due to the variation in the effective dielectric constant. It can be seen that the S_{11} at this frequency has improved with respect to that of the conventional patch antenna case.

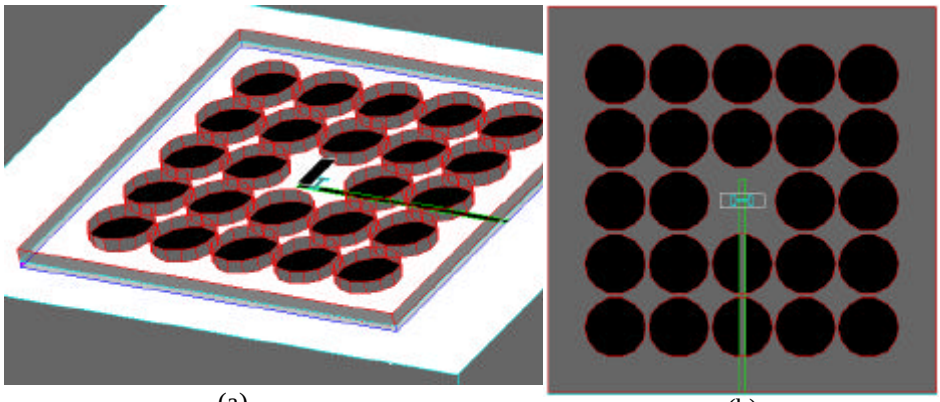

(a) (b)

Figure 4.12: Patch antenna configuration on a Photonic Crystal substrate formed by 2 rows of holes. (a) Side view. (b) Top view.

The radiation patterns obtained at 14.64 GHz are shown in Figure 4.13. The maximum directivity value is 5.3 dB. It can be observed that the different cuts do not present such as influence of the surface wave mode as for the conventional case. This is indicating that the contribution of the surface wave mode has been reduced. In order to verify this claim , Figure 4.14 shows the surface plot of the electric field magnitude, which can be compared with Figure 4.11. Both plots have been normalised at the same scale.

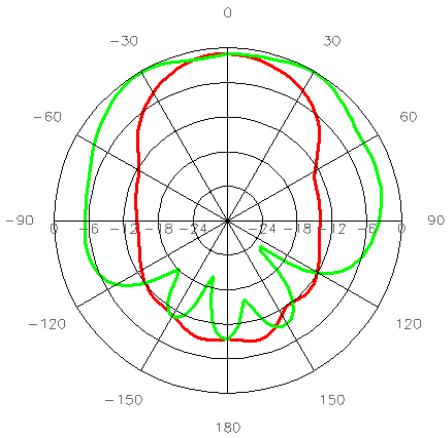

Figure 4.13: Radiation patterns for E (green line) and H (red line) planes at 14.64 GHz for the patch antenna on Photonic Crystal substrate designed with two rows of holes. Maximum directivity is 5.3 dB.

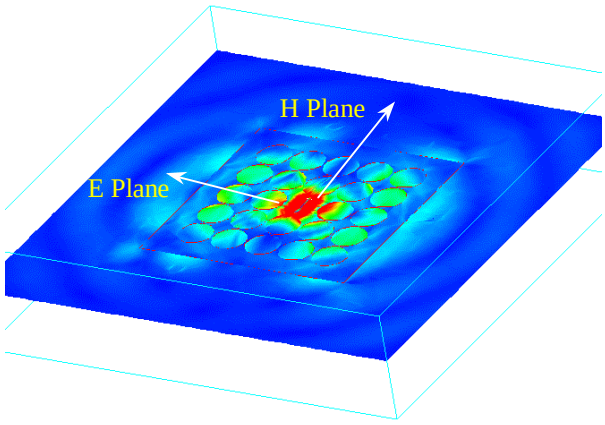

Figure 4.14: Surface plot of the Electric field for the Photonic Crystal patch antenna. Red means maximum power and dark blue is minimum power.

4.3.1.3 Comparison of the results

In this section a comparison between the previous results will be performed. The minimum in the input return losses of the Photonic Crystal substrate has slightly shifted with respect to that of the conventional case, but it presents a very good behaviour, the bandwidth ($S_{11} < -10\,dB$) is 2.2% versus the 3.4% of the conventional antenna. Looking at the E-plane radiation pattern of Figure 4.15(a), it can be clearly seen that the pattern for the Photonic Crystal

substrate case presents an improvements of 3 dB in the front-back ratio and of 2 dB in the radiation at -90 degrees. In general, the reduction in the power levels in the radiation regions that can be affected by surface wave modes is significant.

In the E-plane, the reduction of the surface wave contribution is more important as it can be observed in Figure 4.14. A smoother pattern at boresight direction is obtained, with an additional reduction of the 3 dB at 90 and –90 degrees, and a front-back ratio improvement of 3 dB, see Figure 4.15(b). The cross-polarisation has also been improved, as it can be checked in Figure 4.15(c).

The improvements in the E-plane are more remarkable than for the H-plane, but this is due to the stronger excitation of the surface wave mode in that direction of propagation than for the other one, see Figure 4.11.

The results are indicating that the Photonic Crystal substrate is indeed working as surface wave suppresser but it is still unclear if its performances could be improved by adding more periods.

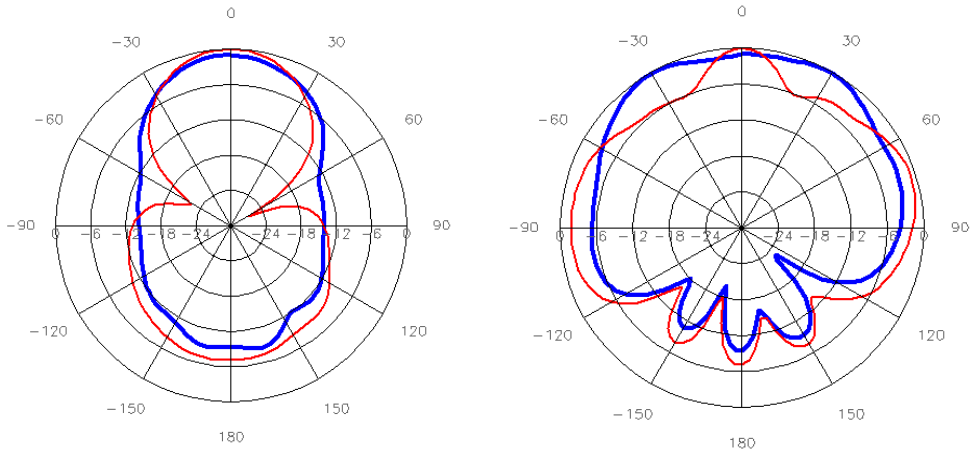

(a) (b)

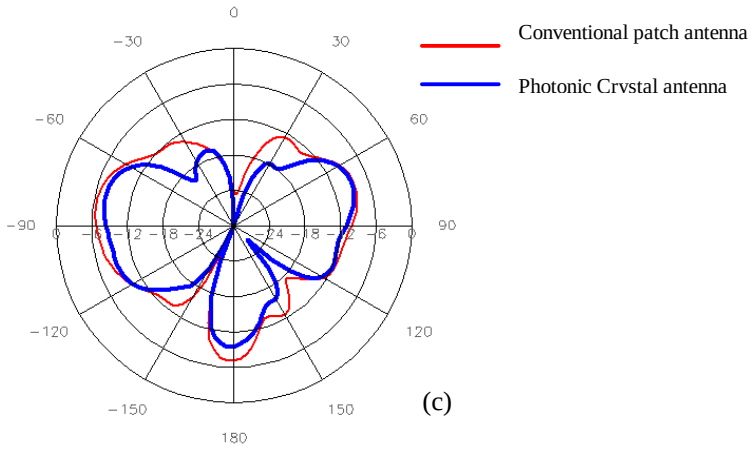

Figure 4.15: Comparison of the radiation patterns for the conventional a Photonic Crystal substrate patch antenna. (a) H-plane. (b) E-plane. (c) Cross-polar component at 45º plane.

4.3.2 Patch antenna in the case of three surrounding rows of holes

4.3.2.1 Conventional patch antenna

In this case, the substrate for the conventional patch antenna has a size of 50x50mm, with the same configuration than in the case of two holes.

The input return loss is shown in Figure 4.16. The S_{11} presents a reflection coefficient of –30dB at 14 GHz. The obtained radiation patterns are plotted in Figure 4.17. As in the previous case, the E-plane is more affected by the surface wave modes showing a high amount of radiated power at 90º, 270º and all the surrounding radiation directions. At the same time, a deep peak of 13 dB has appeared at 30º and the front-back ratio has been decreased up to 6 dB. The H-plane shows lesser effect of the surface wave modes but still, the presence of this contribution can be seen in the radiation from –90º through 180º to 90º. The propagation of the surface wave mode is visualised in Figure 4.18.

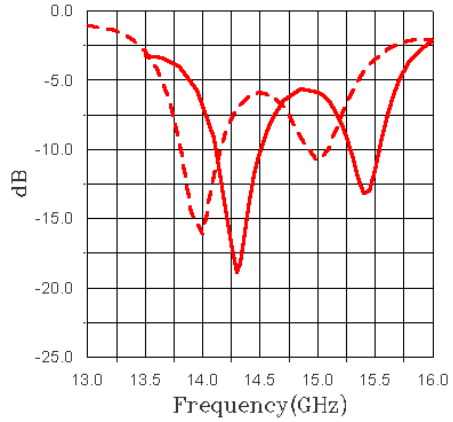

Figure 4.16: Computed input return loss (S_{11}) for the conventional patch antenna (dashed line) and Photonic Crystal antenna (solid line).

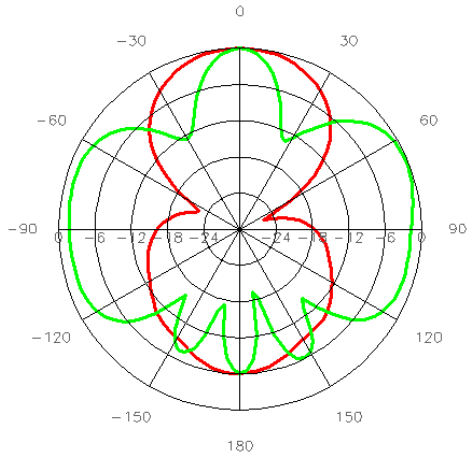

Figure 4.17: Radiation patterns for E (green line) and H (red line) planes at 14 GHz for the conventional patch antenna. Maximum directivity is 5.7 dB.

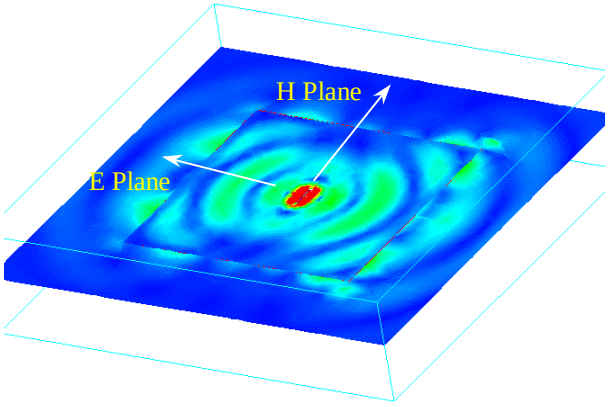

Figure 4.18: Surface plot of the Electric field magnitude for the conventional patch antenna. Red means maximum power and dark blue minimum power.

4.3.2.2 Patch antenna on a Photonic Crystal substrate

This case is similar to the previous case but now an extra row of holes around the patch antenna has been added. In principle, by doing this the reflection from the Photonic Crystal structure should be augmented which leads to decrease the surface wave contribution. As a consequence, the whole Photonic Crystal structure is larger than the previous case. Looking at Figure 4.16, the resonant frequency can be established at 14.3 GHz with a value of –18.5 dB. As this value is pretty close to the 14.44 GHz for the case of two rows of holes, the Photonic Crystal design parameters have been left to the same values (lattice period 6.53mm and radius of the holes 3.14mm).

The results from this configuration are shown in Figures 4.20 and 4.21. The radiation patterns show that the Photonic Crystal substrate configuration is working adequately to reduce the level of the surface wave mode added to the radiation from the antenna. A qualitative way to check this effect is presented in Figure 4.18, where it is seen how the surface wave mode is stopped by the Photonic Crystal configuration.

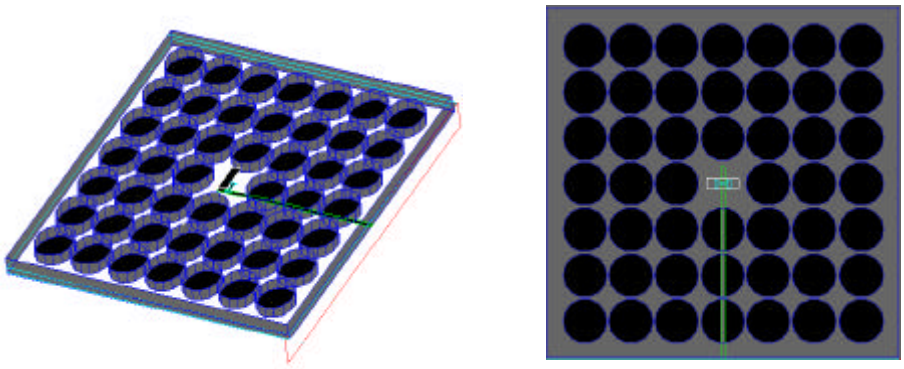

(a) (b)

Figure 4.19: Patch antenna configuration on a Photonic Crystal substrate formed by three rows of holes. (a) Side view. (b) Top view.

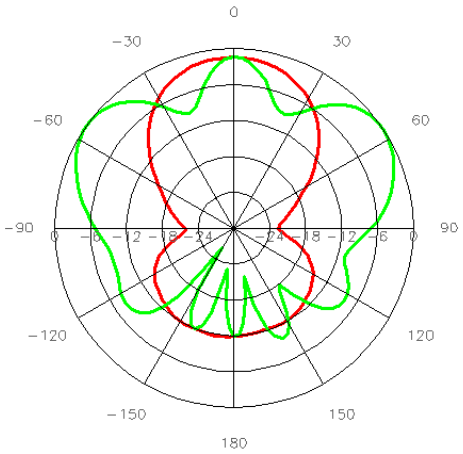

Figure 4.20: Radiation patterns for E (green line) and H (red line) planes at 14.3 GHz for the patch antenna on Photonic Crystal substrate designed with three rows of holes. Maximum directivity is 7.4 dB.

4.3.2.3 Comparison of the results

The first detail that can be observed from the Figure 4.16 is the shift of the resonant frequency of the Photonic Crystal substrate configuration in relation with the conventional patch antenna. This effect was expected, because as it has already commented, the effective dielectric constant for the Photonic Crystal case has been decreased, which will be translated into an increase in the resonant frequency. The bandwidth ($S_{11} < -10\ dB$) is 5.6% versus the 7.1% of the conventional antenna. As the previous case, the bandwidth has decreased somewhat, but it still remains acceptable.

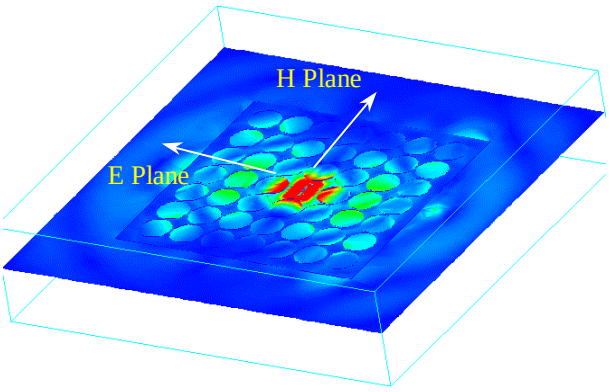

Figure 4.21: Surface plot of the Electric field magnitude for the Photonic Crystal patch antenna. Red means maximum power and dark blue is minimum power .

The radiation patterns of the Photonic Crystal case shown in Figure 4.22 exhibit a reduction in the radiation levels produced by the surface wave mode in all the back radiation direction as well as for the E-plane as for the H-plane. More in detail, the reduction at 90º and –90º is approximately of 6dB for both planes and another 4.5dB in the front-back ratio. The cross-polarisation pattern shows also an improvement of 6dB. The front-back ratio can not be improved much more because the limitation imposed by the radiation of the feeding line placed at the backside of the structure.

Although the function of the Photonic Crystal substrate as suppresser of the surface wave modes has been clearly proven, a ripple in the E-plane still persists despite the fact that this ripple looks smoother. It is already known [YAN 97a and YAN 97b] that this kind of Photonic Crystal structures can excite leaky-wave modes (see Appendix B). Therefore, the lobe at 50º could be thought to be caused by a leaky-wave excitation. But to excite the first spatial harmonic, the following condition has to be satisfied, $b_0/k_0 \geq \frac{l_0}{a} - 1$ [OLI 63]. Basically, this condition is only satisfied at high frequencies values. For the case under study, $b_0/k_0 = 1.955$ and $\frac{l_0}{a} - 1 = 2.2128$. In order to excite these leaky-wave modes for a structure like the one used, the working frequency should be fixed at a value larger than 15.035 GHz (see Figure 4.23). Hence, initially, the coherent excitation of the leaky-wave modes as explanation of this ripple is rejected.

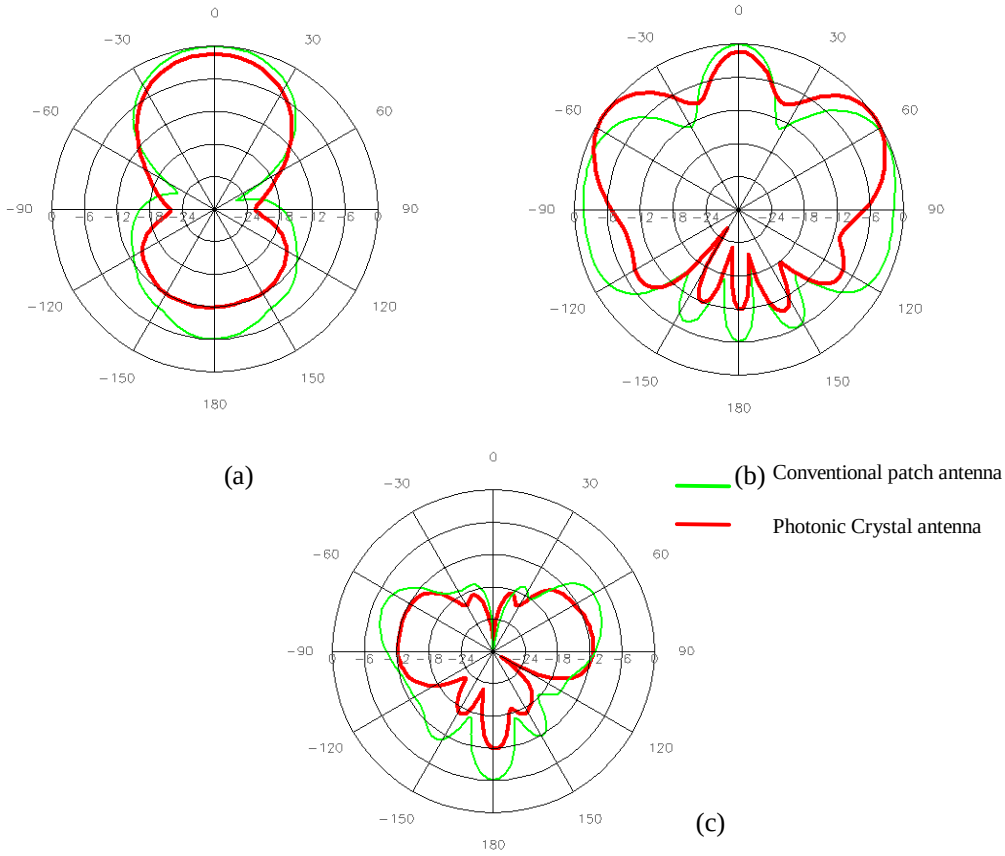

Figure 4.22: Comparison[1] of the radiation patterns for the conventional a Photonic Crystal substrate patch antenna. (a) H-plane. (b) E-plane. (c) Cross-polar component at 45º plane.

In reality, the peak is produced by two undesired radiations. The first one is the radiation of the surface wave mode, which is added in counter-phase just at the 50º zone of the radiation direction. Besides, the power level of the surface wave mode is very important being comparable to the main beam. This fact can be checked looking at Figure 4.22(b), the radiation at 90º is 2 dB less than the radiation at 0º. Therefore, the addition of this power in counter-phase with the power coming from the patch antenna can produce a minimum in some radiation direction like the one that can be seen at 30º in Figure 4.22(b) for the conventional antenna case. By changing the dimensions of the substrate the radiation pattern is also modified, and other peaks appear at different radiation directions (the pattern

[1] Note that the normalisation factor for the conventional patch antenna is 5.7 dB, meanwhile for the Photonic Crystal substrate case is 7.4 dB.

in Figure 4.10 is different to the one in Figure 4.17). When the Photonic Crystal substrate is introduced, a reduction of this level is detected due to the working of the Photonic Crystal structure as suppresser of the surface wave mode. This effect can be seen in Figure 4.22b, where the minimum at 30º has been reduced but it still persists on the radiation pattern.

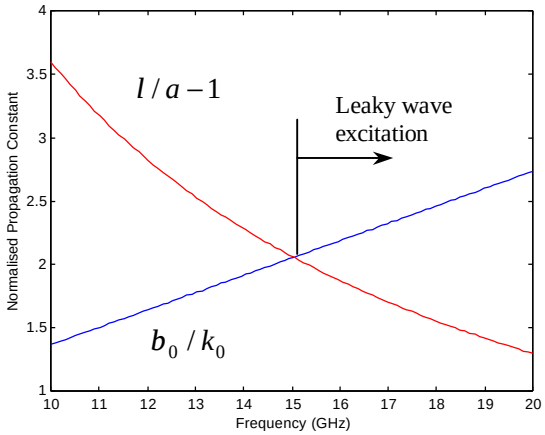

Figure 4.23: Normalised propagation constant (b_0 / k_0) as function of the frequency for the Photonic Crystal substrate and for the first harmonic spatial.

Furthermore, the radiation coming from the radiating modes excited due to the Photonic Crystal substrate does not exhibit a complete band gap is the responsible for the existence of these peaks. This radiation will be always added in the forward direction to the radiation pattern and it will be not possible to suppress it. This effect can be corroborated looking at the case of Photonic Crystal structure in Figure 4.22b, the radiation peak values at $\pm 50^{o}$ are higher than the radiation at 0º, meanwhile this is not happening in the conventional case.

Anyway this effect could be overcome in the case of working with array configurations, because the influence of this radiation modes in comparison with the addition of the radiation from the antennas will be less important.

4.3.3 Patch antenna in the case of four surroundings rows of holes

In this case, only the comparison between both results will be presented. The input return loss is shown in Figure 4.24. Both behaviours are quite similar, exhibiting two resonant frequencies, which are quite close, less than 1 GHz. As in

the previous cases, a small shift in the resonant frequency for the Photonic Crystal substrate is found. Focusing only in the resonant peak at 15 GHz, the obtained bandwidth is about 2% for both cases, nevertheless, the antenna could be used in the range between both peaks, presenting for this case an approximate bandwidth of 7%.

The radiation pattern is depicted in Figure 4.25. The selected frequency was 15 GHz, due to both antennas have the same S_{11} parameter. At this frequency the directivity values is 5.8 dB in both cases. The improvements by using the Photonic Crystal substrate are impressive.

Just for this substrate size, the surface wave mode is added in counter-phase for the conventional patch antenna showing a very low value in boresight direction. This effect is reduced in the Photonic Crystal antenna offering a smooth radiation pattern without such as deep peaks. The directivity value is increased in 10dB. The back and side radiation is also reduced as in the previous cases.

Finally, the electric field representation is shown in Figure 4.26, the reduction in the surface wave mode levels are very important as it was expected from seeing the radiation pattern.

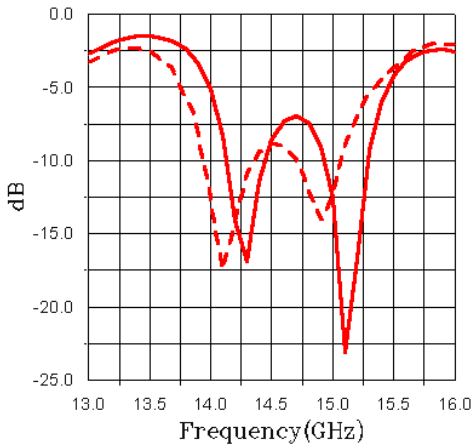

Figure 4.24: Computed input return loss (S_{11}) for the conventional patch antenna (dashed line) and Photonic Crystal antenna (solid line).

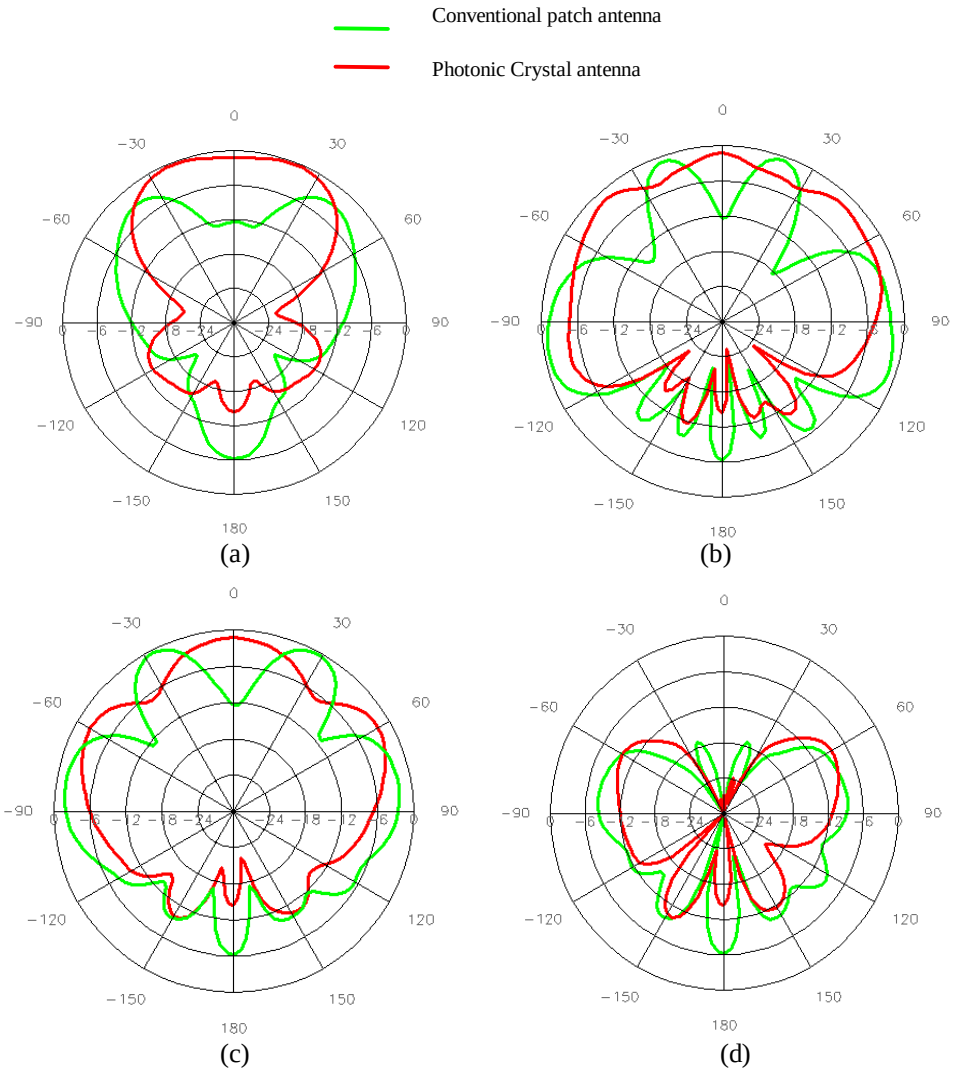

Figure 4.25: Comparison of the radiation patterns for the conventional a Photonic Crystal substrate patch antenna. (a) H-plane. (b) E-plane. (c) 45º plane and (d) Cross-polar component at 45º plane. The directivity value is 5.8 for all results.

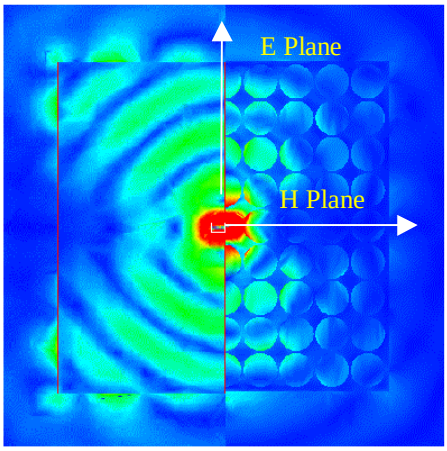

Figure 4.26: Surface plot of the Electric field magnitude for the conventional and for the Photonic Crystal patch antenna. Red means maximum power and dark blue is minimum power.

4.3.4 General Remarks

Summarising the results obtained for the patch antenna presented here as well as for the already ones studied [GON 99d and GON 00a], some conclusions can be extracted. The first one is the shift produced in the resonant frequency for the Photonic Crystal substrate versus the conventional substrate. This behaviour is common for the cases studied and it can be explained by the variation in the dielectric constant around the patch antenna.

Comparisons between the results f rom a conventional patch antenna to a patch antenna on a Photonic Crystal substrate show that the reduction in the surface mode level is remarkable. This can be observed in the radiation pattern (reduction of the radiated powers at -90^{o} and 90^{o}), and also in the surface plots (the levels have been reduced). This will lead of course to an increase in the antenna efficiency.

Also the back radiation and the cross-polarisation are reduced. The minimum back radiation is limited by the radiation from the microstrip feeding line placed on the microstrip substrate.

On the other hand, as the number of periods is increased the influence of the radiation modes appears in the pattern as a ripple. For the case of two holes there are not appreciable peaks in the E plane becoming more important when the number of holes is increased to three or four.

A graphical representation of the improvements obtained in this analysis can be seen in Figure 4.27. Here, the results obtained for all the configurations studied in this dissertation are plotted.

Finally, taking as example the four rows of holes, the E plane radiation patterns, the most restrictive plane, for different frequencies are presented in Figure 4.28. The frequencies go from 13.5 GHz to 16 GHz in steps of 0.5 GHz. Looking at the results for the conventional case (Figure 4.28.a), it possible to observe that the pattern (from 60º to º50º) is changing because the contribution of the surface wave mode depends on the propagation constant. Besides, around 120º the amount of radiated power is quite high. Instead, by using the Photonic Crystal substrate, these patterns are quite similar and smooth, indicating that the surface wave mode has been mitigated in the frequency range of operation (about 13.5 to 15.5 GHz) and offering a high stable radiation pattern as function of the frequency. It should be noted that the cut at 16 GHz (thick dark blue line) shows a deep ripple due to the non-existence of gap at that frequency.

It is clear that Photonic Crystal substrates have potential for array configurations, increasing the antenna efficiency together with the suppression of its mutual coupling through the substrate material. Some initial results about this improvement are analysed in the next section.

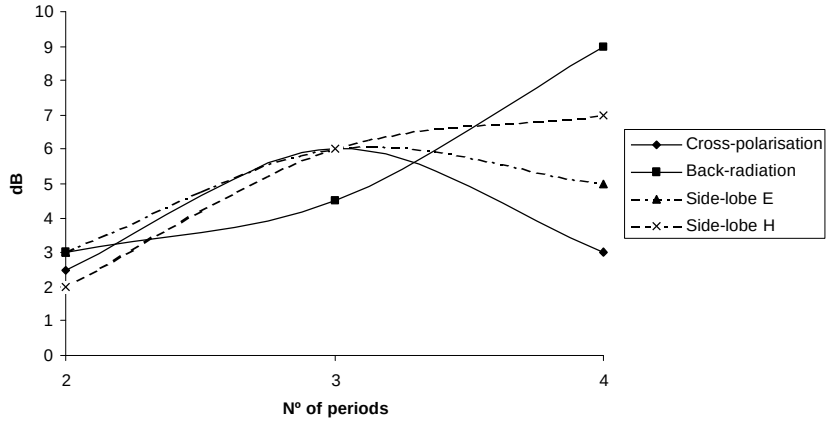

Figure 4.27: Improvements on the main parameters of the Photonic Crystal substrate radiation patterns along with the conventional ones as function of the number of periods in the Photonic Crystal structure.

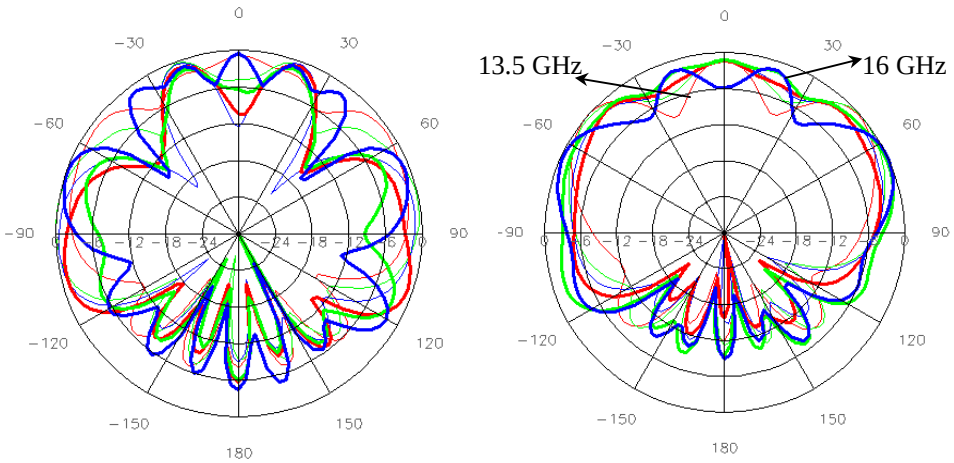

Figure 4.28: E plane radiation patterns for the conventional patch antenna (a) and for the four rows of holes case (b) working at different frequencies (from 13.5 to 16 GHz each 0.5 GHz). Each colour shows a different frequency value.

4.4 Mutual Coupling Between Patch Antennas

In this section an analysis of the front (E plane) and side (H plane) coupling between two patch antennas on a conventional substrate and on a Photonic Crystal substrate has been developed. The front coupling is the most restrictive one as it has been proven in the previous section, the excitation of surface wave mode at that direction is more significant.

Following the previous developments, the selected frequencies to prove the behaviour of this structure will be in the range of 15 GHz. A new patch antenna configuration has been designed. The selected one corresponds to Figure 4.1(b). The reason to perform this change it is based on fabrication issues. The aperture coupling patch antennas are more difficult to fabricate than the patch antennas using microstrip feeding techniques. Besides, by using the aperture coupling method to feed the patch antenna, a similar excitation of the surface wave mode for each side of the antenna is found, as it can be seen in Figure 4.11 and 4.18. Meanwhile by using microstrip techniques the excitation becomes more important in the direction in which the other patch antenna is placed. For the behaviour that is desired to check this configuration (see Figure 4.29) is adequate.

4.4.1 E-plane coupling

The designed patch antenna has the resonant frequency at 15.5 GHz. The selected Photonic Crystal structure is the square array of drilled holes with a period lattice (*a*) of 6.32mm and a hole radius of 3.03mm. This lattice has been calculated to suppress the surface wave propagation at the operational frequency range of the patch antenna following the rules given in previous sections. The distance between antennas is 23.8mm ($=1.23\lambda_0$) in order to be able to place three rows of holes in between.

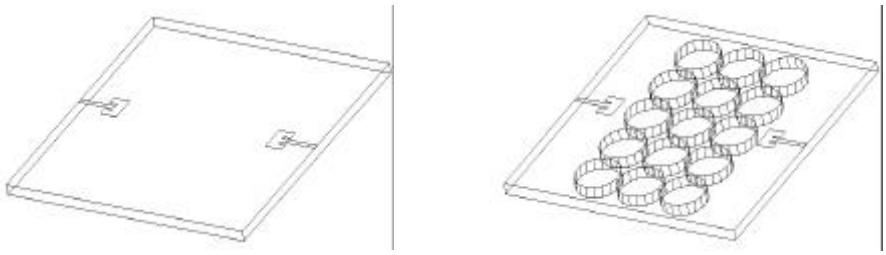

(a) (b)

Figure 4.29: Patch antenna configuration selected to characterise the coupling between antennas. (a) Patch antennas on a conventional substrate. (b) Patch antennas on a Photonic Crystal substrate formed by three rows of drilled holes.

A comparison between the coupling of two patch antennas on a conventional substrate and on a Photonic Crystal substrate with one, two and three rows of holes has been performed. Figure 4.30 presents the results of the S_{11} and S_{21} for all configurations. A reduction on the S_{21} parameter is obtained as the number of holes is increased. The results from the no hole and one hole cases are quite similar. For the two holes case, the difference begins to become appreciable and, as it would be expected, the three holes case presents the highest rejection values. Comparing the no holes with the three holes case, it can be pointed out that in the frequency band from 15 GHz to 15.7 GHz, an improvement in the rejection larger than 15 dB has been obtained, getting coupling values less than 30 dB. Out of this band, the S_{21} of the conventional case is decreased but this is due to the deterioration of the S_{11} performance, which means that less power can arrive at the other patch antenna. On the other hand, the S_{21} of the Photonic Crystal antenna remains rather constant with values less than 30 dB. This can be expected because looking at Figure 4.6(a) and performing the appropriate operations, the bandwidth of the Photonic Crystal structure will go approximately from 13 GHz to 16 GHz. From the upper edge of this band (16 GHz) the S_{21} does not go up because the transmitted power from the antenna is very low.

Another two relevant remarks can be extracted from Figure 4.30. The first one is the fact that the S_{11} curve of the conventional antenna does not go up for lower frequencies as fast as the S_{11} curve of the Photonic Crystal antenna. This is indicating that the conventional patch antenna has more losses, which are produced by the excitation of the surface wave mode. This effect is avoided in the Photonic Crystal substrate. Anyway, this effect would be more appreciable if instead of placing holes just in front of the antennas, the holes were surrounding the antenna, as in a real case, but here only the examination of the behaviour was desired. For higher frequencies all the plots are quite similar because the Photonic Crystal is out of band.

The second remark comes from the radiation of the receiving antenna. Some of the power transferred to this antenna through the surface wave mode is radiated to the free space before reaching the output port, which means that it is not affecting to the S_{21} value. Therefore, indeed the amount of power coupled between antennas should still be higher for the no holes case, whether the previous effect could be taken into account. In order to present a confirmation of this issue, the Figure 4.31 presents the electric field magnitude on the antenna plane for the conventional and Photonic Crystal substrates.

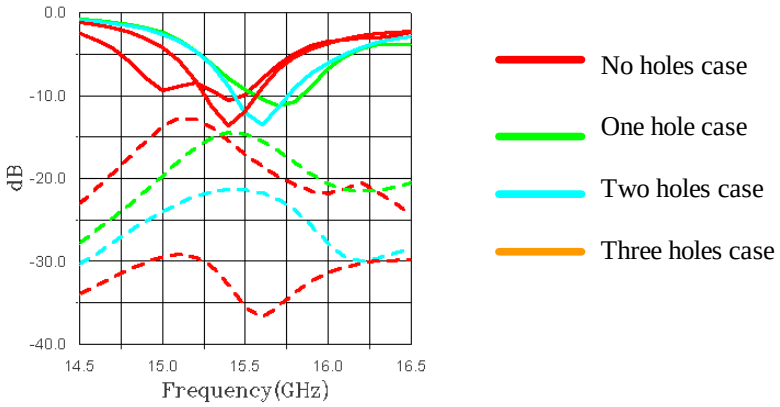

Figure 4.30: Comparison of the S_{11} (solid lines) and S_{21} (dashed lines) of the configuration shown in Figure 4.29 for the conventional substrate and the Photonic Crystal substrate with one, two and three rows of holes.

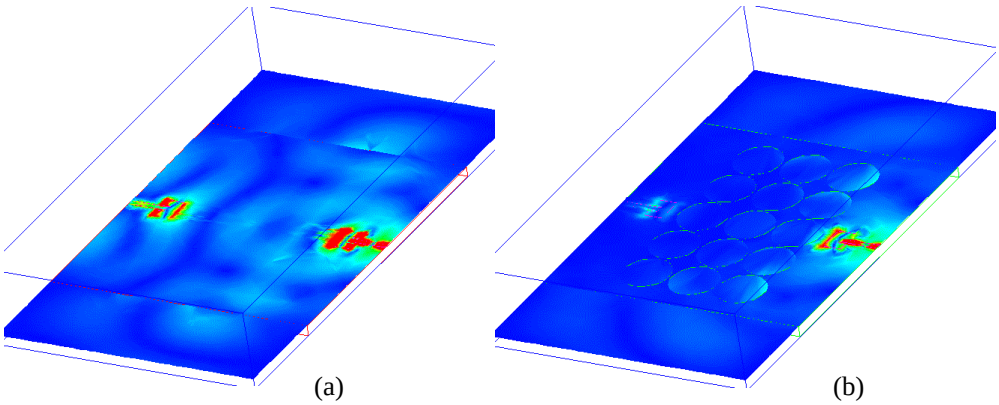

(a) (b)

Figure 4.31: Graphical representation of the electric field magnitude at the antenna plane for the conventional patch antenna (a) and the Photonic Crystal substrate antenna formed by three drilled holes (b). Both plots have been normalised to the same scale.

4.4.2 H-plane coupling

The antenna parameters are the same that those described in the previous section. In this case the coupling between two adjacent antennas will be calculated. The selected distance between antennas is 31.6mm ($=1.62\ l_0$) in order to be able to place four rows of holes in between as it is shown in Figure 4.32.

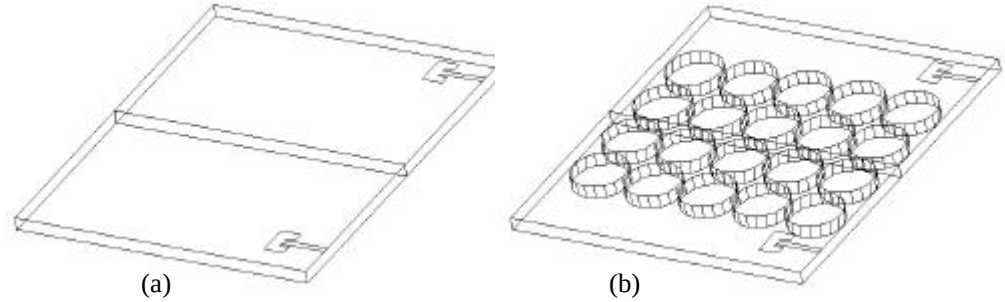

(a) (b)

Figure 4.32: Patch antenna configuration selected to analyse the coupling between antennas. (a) Patch antennas on a conventional substrate. (b) Patch antennas on a Photonic Crystal substrate formed by four rows of drilled holes in between.

The S_{11} and S_{21} parameters are depicted in Figure 4.33. It is clear that as the number of rows is increased, the coupling factor decreases. The rejection factor increases from 2 dB to 15dB, and as it can be seen the variation is not linear.

All the comments done in t he previous section are applicable here. For this case, as it was expected, the coupling factor is smaller due to the most of the surface wave mode is propagating in the E-plane direction. Besides, this fact does that the S_{11} behaviour looks quite close for all the studied configurations. Finally, and as illustrative example, Figure 4.34 shows the electric field representation, where it can be observed that the power received has been minimised by the Photonic Crystal substrate.

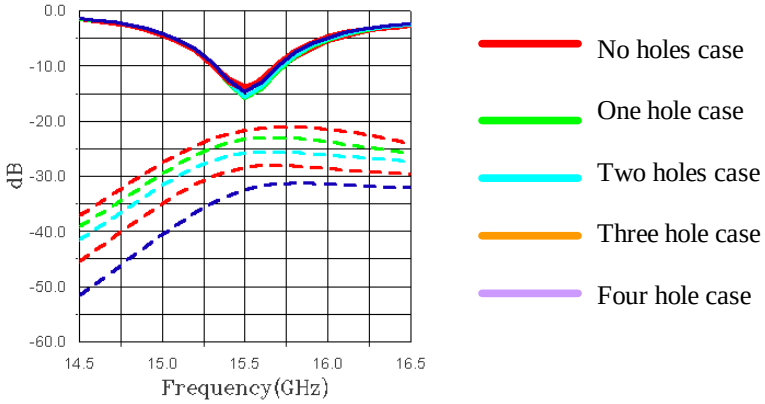

Figure 4.33: Comparison of the S_{11} (solid line) and S_{21} (dashed lines) of the configuration shown in Figure 4.32 for the conventional substrate and the Photonic Crystal substrate with different drilled holes in between antennas.

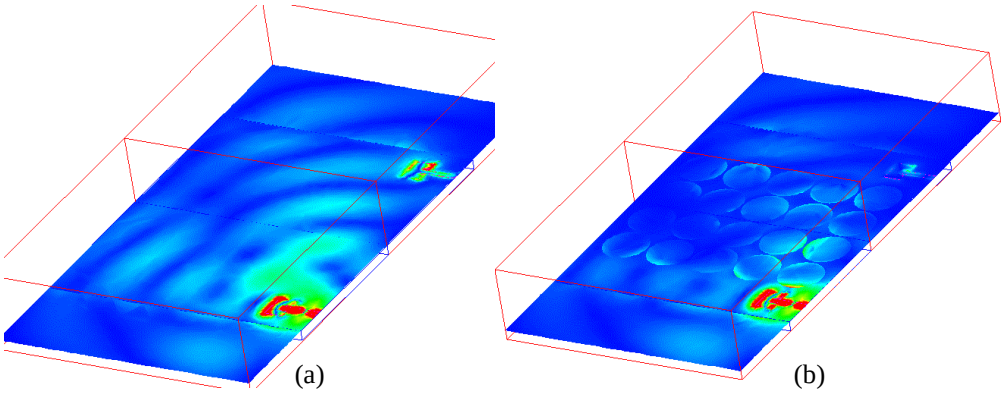

Figure 4.34: Graphical representation of the electric field magnitude at the antenna plane for the conventional patch antenna (a) and the Photonic Crystal substrate antenna formed by four drilled holes (b). Both plots have been normalised to the same scale.

CHAPTER 5

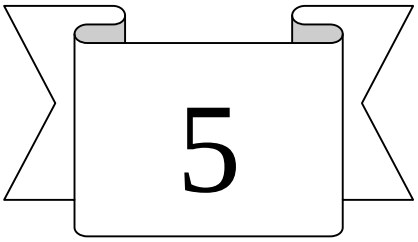

WOODPILE PHOTONIC CRYSTAL STRUCTURE FOR DIPOLE ANTENNA CONFIGURATION

A new generation of scientific space borne instruments, included in both Earth observation and scientific missions, is under consideration at millimetre and sub-millimetre wavelengths. In the present ESA (European Space Agency) Earth observation studies millimetre and sub-millimetre limbsounding instruments (e. g. MASTER, SOPRANO, PHYRAMID) are already using frequencies up to 1THz. Also projected in this frequency band are astronomy missions (e. g. FIRST, PLANK) the frequency range of which may even extend above 3THz [DEM 00].

As the frequency increases, a planar structure which integrates the antenna, mixer, local oscillator and a peripheral circuitry onto one single substrate becomes an attractive option.

While conceptually simple, in practice it is challenging to develop and test an integrated planar antenna on a semiconductor substrate (high dielectric constant) which has a good radiation efficiency and pattern and can be easily integrated with the active circuit.

One of the problems that has been encountered, is the fact that planar antennas on dielectric substrates couple power into substrates modes, and since these do not contribute to the primary radiation pattern, substrate mode coupling is considered as a loss mechanism.

Research on integrated lens antennas has already shown that the radiation characteristics are very promising and the integrated lens designs have already reached some level of maturity. But they still suffer loss and some problems in the impedance matching.

Due to this, a Photonic Crystal structure is proposed to reduce the loss mechanism based on the surface wave propagation, improve the impedance matching and obtain good efficiency and radiation pattern features.

The technology used in the previous chapter was microstrip , therefore, two-dimensional structures seemed more appropriate to suppress the surface wave propagation. For others kinds of antennas as dipoles, monopoles, double–slots, it seems most appropriate to utilise a three-dimensional Photonic Crystal as substrate. In this chapter, a three-dimensional structure will be employed to prevent the back and side radiation from a dipole antenna. The selected three-dimensional structure will be the woodpile Photonic Crystal designed. The design, analysis, fabrication and measurements at 500 GHz of this structure will be presented. A new fabrication technique has been used to manufacture the woodpile structure.

In addition , the design of the dipole will be performed. The simulated radiation patterns of the dipole on top of the woodpile structure will be shown. A reduction in the back radiation, a high symmetric beam and an increase of the directivity values have been reported.

5.1 Design of the Woodpile Photonic Crystal

A complete analysis of the woodpile structure has already been performed in section 3.3.2. A plot with the structural configuration of this Photonic Crystal can be seen in Figure 3.37 and 3.38.

In this chapter, a structure is proposed where an angle of 60 degrees is formed (see Figure 5.1) between bars of different layers in the same stacking

direction. By using this configuration, a triangular-hexagonal structure of bars is obtained. In this case, the configuration has a centre-to-centre distance (width) between bars of a (normalised value) and a unit cell height of $\sqrt{3}a$. As the structure is formed by squares bars touching each others, the diameter of each bars will be *0.433a*. The selected material for the fabrication was Silicon, which, based on the manufacturer specifications, has a dielectric constant of 11.7.

The method used to analyse the structure's behaviour was the plane wave analysis described in the Chapter 2. This method starts with the Maxwell's equations in a generalised eigenvalue form. The plane wave expansion allows this set of equations to be solved by converting them into a Hermitian eigenvalue problem.

As explained before, the method requires the definition of the unit cell and the Brillouin zone of the structure. These parameters were described in a general way in Chapter 3. Here, the specific values for the case under study will be presented. The vectors defining the minimal unit cell are the following:

$$\begin{aligned} \hat{a}_1 &= a \cdot \hat{x} \\ \hat{a}_2 &= a \cdot \hat{y} \\ \hat{a}_3 &= \frac{a}{2}\left(\hat{x} + \hat{y} + \sqrt{3}\hat{z}\right) \end{aligned} \tag{5.1}$$

where, a is the normalised unit cell value.

From these values, the reciprocal lattice vectors can be directly determined,

$$\begin{aligned} \hat{b}_1 &= \frac{2p}{a}\left(\hat{x} - \frac{1}{\sqrt{3}}\hat{z}\right) \\ \hat{b}_2 &= \frac{2p}{a}\left(\hat{y} - \frac{1}{\sqrt{3}}\hat{z}\right) \\ \hat{b}_3 &= \frac{2p}{a}\frac{2}{\sqrt{3}}\hat{z} \end{aligned} \tag{5.2}$$

Using these vectors in the plane wave analysis, the resulting band structure is shown in Figure 5.2. A total of 5488 plane waves were used in the calculations. A complete gap has been obtained for a normalised frequency range from 0.2954 to 0.3307. The plot shows the dispersion relation for the woodpile structure in the

Irreducible Brillouin zone. The corresponding k components for each point in Figure 5.2 are shown in table 5.1.

Point	k_x	k_y	k_z
0	0	0	0
1	p/a	p/a	0
2	p/a	p/a	$p/\sqrt{3}a$
3	$2p/3a$	$2p/3a$	$2p/\sqrt{3}a$
4	0	0	$2p/\sqrt{3}a$
5	0	$4p/3a$	0
6	0	$2p/3a$	$2p/3a$

Table 5.1: Values of the k components for each point plotted in Figure 5.2.

The gap-midgap ratio for this woodpile structure is about 11.3 % as full gap and 32.3 % for normal incidence case. The normal incidence case corresponds to point 4 in Figure 5.2. In this case, the gap extends from 0.2388 to 0.3307 value of the normalised frequency.

The desired working frequency for the Photonic Crystal is 500 GHz. Using this data and taking into account that the dispersion relation plots are normalised, the dimensions can be easily obtained.

By fixing $\frac{fa}{c} = 0.3$ and $f = 500\,GHz$, a value of $a = 180\,mm$ is obtained as periodic lattice constant (see Figure 5.1). As the selected woodpile structure is a triangular one, the angle between bars should be 60 degrees, which implies a height in the unit cell of $\sqrt{3}a$. At the same time, this value should be equal to $8r$, being r the square bar radius. As result, a radius value of $r = 0.2165a$ is obtained which leads to $r = 39\,mm$.

Using the obtained lattice value, the frequency gap for normal incidence can be calculated. This predicted gap would go from 395 GHz to 550 GHz.

To verify these results, another software package, HFSS (High Frequency Structure Simulator) was used. Due to memory restrictions on the PC, only a mesh formed by 4x4x4 cells was analysed (see Figure 5.3). Absorbing boundary conditions were applied to all the faces in which the woodpile structure is enclosed. The input port is placed on top and the output port on the bottom. The S_{21} parameters for the two incident perpendicular polarisations are shown in Figure 5.4(a). For normal incidence, the obtained results show that the two polarisations

(TE and TM) are degenerate exhibiting the same S_{21} parameter behaviour, as it is was expected from the plane wave analysis. For this case, the gap edges (-12.5dB point) go from 375 GHz to 530 GHz, very close to the previous predicted results with the plane wave analysis. The small difference is probably coming from the finite analysis performed with this software. In conclusion, this result is in good agreement with the plane wave analysis performances. Figure 5.4(b) shows the results for perpendicular incidence. In this case, a different behaviour as function of the incident polarisation is expected (point 5 in Figure 5.2). The results are also in good agreement with the plane wave analysis. A shift between calculation methods is also obtained.

The frequency response for other incidence *k* directions can not be checked easily with this commercial software.

Various studies concerning the gap width sensitivity to parameter variations (variation of the layer thickness, variation of the stripe width, misalignment of stripe position) have been performed. The end conclusion is that this structure is very robust achieving wide band gaps (about 10%) even with variations of 10% in the main parameters indicated previously [CHU 99].

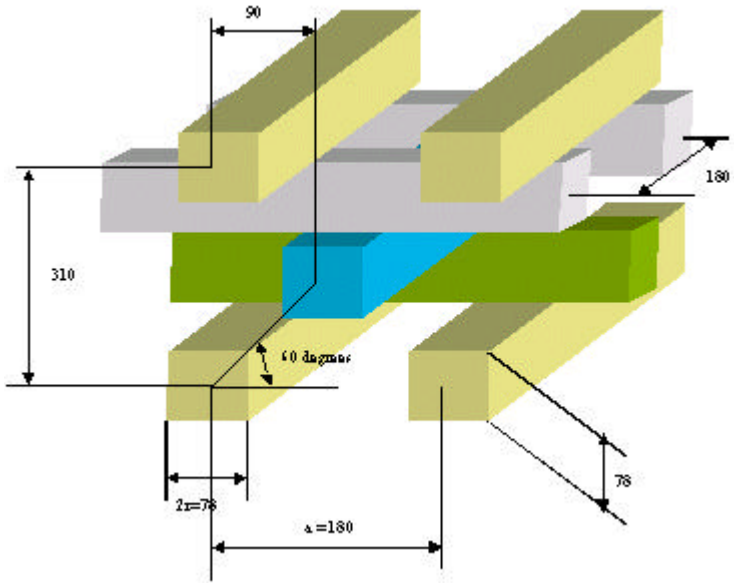

Figure 5.1: Woodpile dimensions (μm) used as input for the fabrication process.

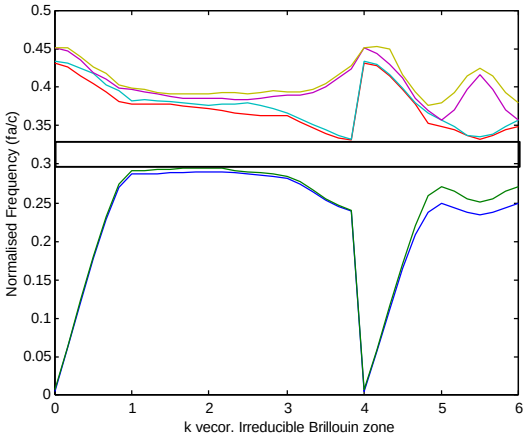

Figure 5.2: Dispersion relation for the designed triangular-hexagonal woodpile crystal.

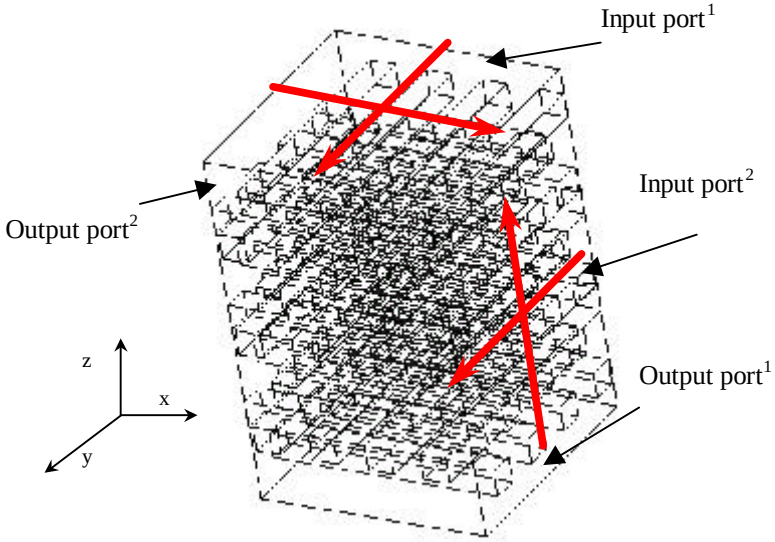

Figure 5.3: Plot of the woodpile crystal structure used in the HFSS software to calculate the transmission parameters under normal [1] and perpendicular [2] incidence. The structure is formed by 4 periods in the x-y plane and 4 in the stacking direction (z). The red lines show the two different polarisations.

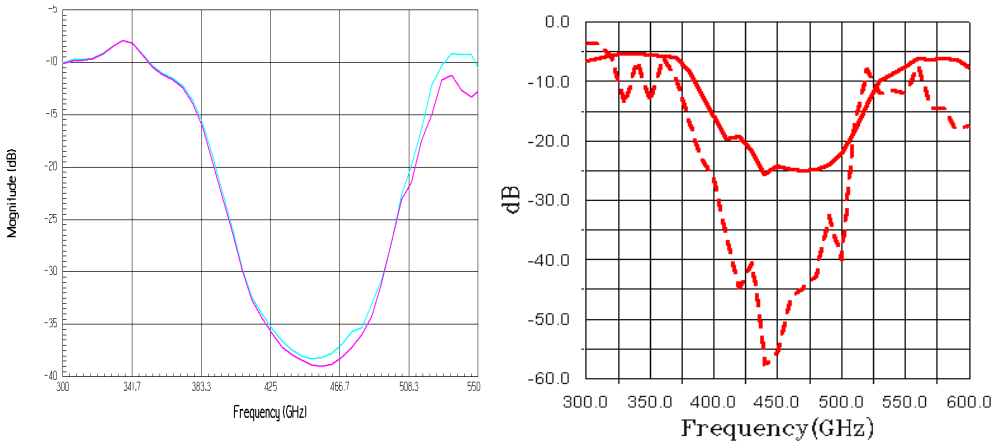

(a) (b)

Figure 5.4: S_{21} parameter for the two orthogonal polarisations (TE and TM). (a) Normal incidence and (b) perpendicular incidence.

5.2 Woodpile Fabrication Process

Once the woodpile Photonic Crystal has been theoretically analysed, the fabrication process was carried out. Whilst anisotropic wet etching of silicon [OZB 94a, OZB 94d and CHE 95] can be used with success for the formation of channel with vertical walls, the process has its limitations, i.e. process control, alignment to crystal planes, sufficient aspect ratio, fabrication time and structure robustness.

An alternative approach for the fabrication has been developed. This is based on the formation of such grid arrays by using mechanical dicing via the use of a high-speed diamond-cutting wheel of the sort used as standard in the silicon industry.

The silicon wafer could have a series of grooves cut into the front face and alternatively, a series of grooves could be placed in the backside of the wafer that open up windows but leave the array joined at the crossing points of the groove (see Figure 5.4).

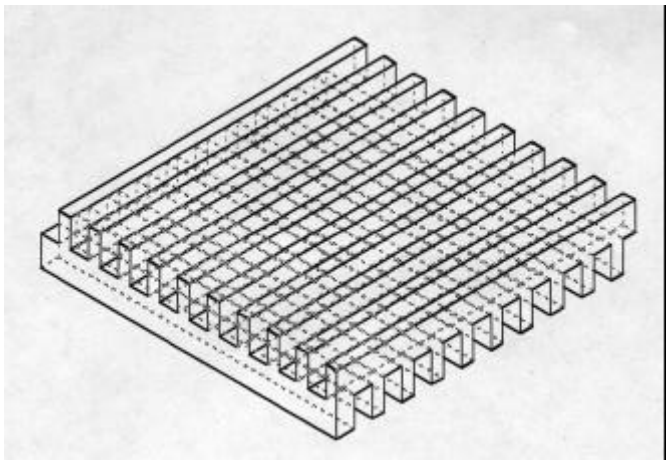

Figure 5.4: Drawing explaining how the fabrication process is performed. Two arrays of grooves joined at the crossing point. This picture is depicting a half period of the woodpile structure.

This process has a number of advantages, namely the manufacturing time, the robustness and that the spacing and depth of the grooves can in principle be set very accurately due to the micron level precision available. The limits of the precision in the machine are defined by the following values ; the repetition spacing 60μm, the bar thickness 30 μm and the maximum bar depth 90 μm.

The selected material for the fabrication was Silicon wafers (11.7 as dielectric constant) with the following specifications,

Growth Method: Fz
Quality: prime
Diameter: 3.00" (76 .20 ± 0.30 mm)
Orientation: <100> ± 0.5°
Type/Dopant: n/Phosphorous
Resistivity: greater/equal 1000 ohm cm
Primary flat: <110> ± 0.5°
Secondary flat: optional
Thickness: 155 ±2 μm.

The high resistivity of the wafers leads to a minimisation in the absorption loss in the silicon, as the loss tangent is directly proportional to the conductivity, which is inversely proportional to the resistivity. The selected thickness corresponds to the half of the thickness periodicity, which contains two layers of bars. It was selected in this way in order to apply the fabrication process indicated previously (see Figure 5.4).

The machine used in the fabrication process is a high precision dicing machine. Control over periodicity, height and cut size is easily handled by a numerical display (see Figure 5.5).

Figure 5.5: Dicing machine.

Because the silicon wafers are circular, the wafers were previously cut into square shapes (see Figure 5.6). The size of these pieces depends on the desired final size of the woodpile Photonic Crystal. By working with smaller pieces, breakage during the fabrication process is reduced and the manipulation eased. Also as the Silicon crystal orientation is <100>, the cutting process was performed along the <110> crystal plane orientation to reduce the tending for the fabricated bars to break and increase the final robustness of the end woodpile.

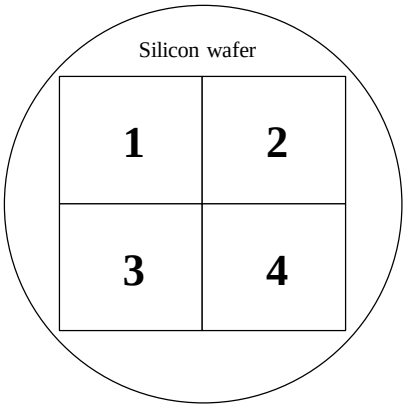

Figure 5.6: Circular silicon wafer transformed into smaller square pieces

Once the square silicon pieces have been generated, the dicing process is performed. The first step is to open up the grooves in one of the sides (see Figure 5.7). The selected cutting depth was 80 μm (approximately the half of the total silicon thickness). Before proceeding with the cutting on the other side, the square silicon wafer is fixed by using wax to a bigger glass wafer in order to avoid fragility and breakage problems (see Figure 5.8).

At this point, it should be noted that the blade path and the metallic table were not parallel. Due to this, when the dicing process on the other side was carried out, the cutting depth had to be increased in order to guaranty that during the process, at least, half of the silicon was removed. In order to achieve this, a depth of about 90μm in thickness was selected.

This process leads to create two kinds of bars, which have different thickness as function of the orientation. In addition, due to the stacking procedure employed (see Figure 5.10), all the bars with the same thickness were aligned in the same direction.

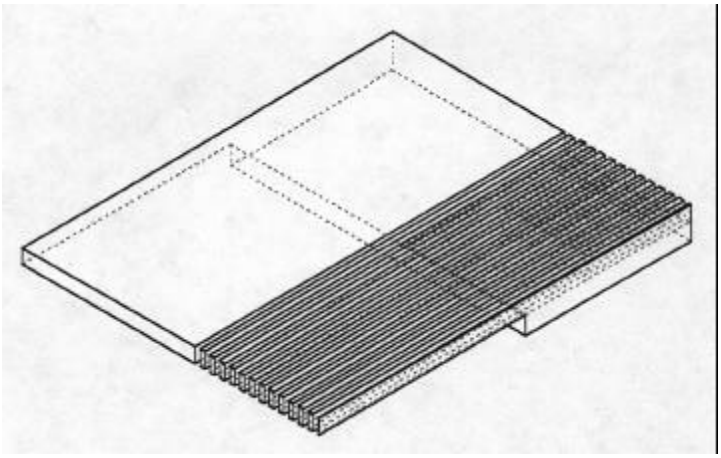

Figure 5.7: Drawing showing the dicing results in one of the sides.

When the square silicon wafer has been completely diced (both sides), half of a complete period of the woodpile structure is obtained. As this piece was big enough, it could be cut creating smaller pieces, which, by stacking, generate the entire woodpile structure (see Figure 5.9). From one big piece, 10 smaller sections were obtained. Each of the smaller pieces still consisted of 50 periods in the x-y plane and half a period in the stacking direction (z).

Figure 5.8: Silicon wafer glued to a crystal wafer.

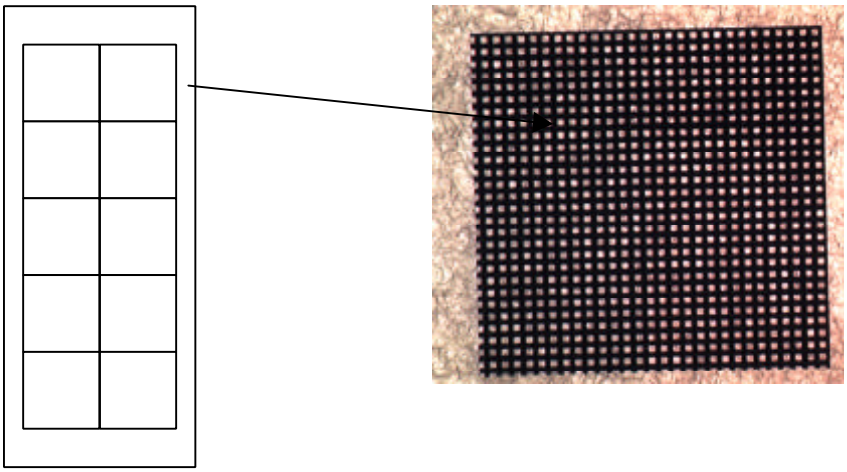

Figure 5.9: Splitting of the silicon wafer into the final woodpile pieces.

Automatic alignment and *0.5a* period offset of successive layers is achieved by cutting the segments of woodpile in a particular way. This is shown in Figure 5.10. Essentially, the bars are cut in half such that opposite corners form either the centre of a high dielectric region of the woodpile or low dielectric. These are designated dielectric-dielectric or air-air corners. By stacking dielectric-dielectric corner on top of air-air corner whilst maintaining the same direction for the top silicon bars, the desired shifting and alignment between layers is automatically obtained.

After stacking all the pieces, the woodpile Photonic Crystal was obtained (see Figure 5.11). The final size was 9x9x1.55 mm. In order to be able to handle the complete structure, an epoxy glue is used to fix together all the pieces forming the whole structure. Three different lateral faces of the woodpile crystal structure were glued to guaranty the robustness of the woodpile (see Figure 5.12a).

A completely gallery of pictures of the woodpile Photonic Crystal is presented in Figure 5.12.

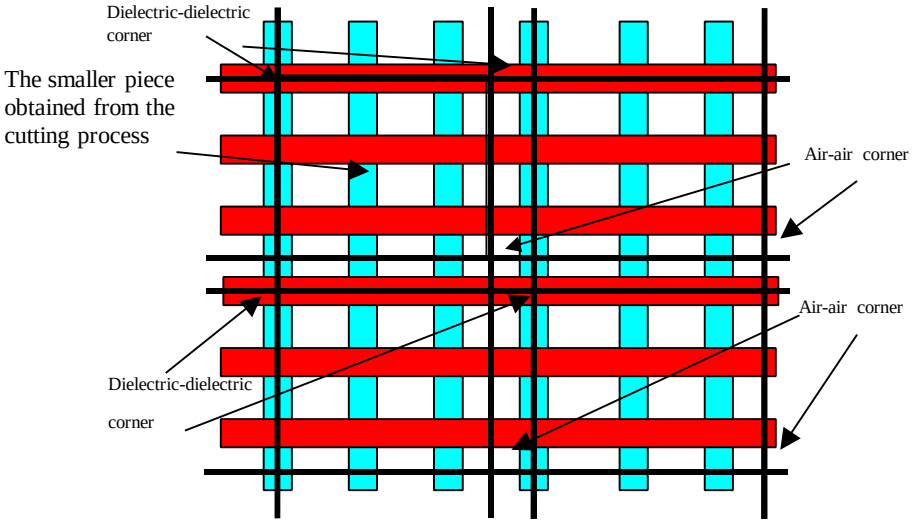

Figure 5.10: Picture showing the cutting way to get directly the correct stacking of the different pieces forming the woodpile Photonic Crystal. Each colour means a different layer. Black lines show the positions where the cuttings of the piece have to be performed.

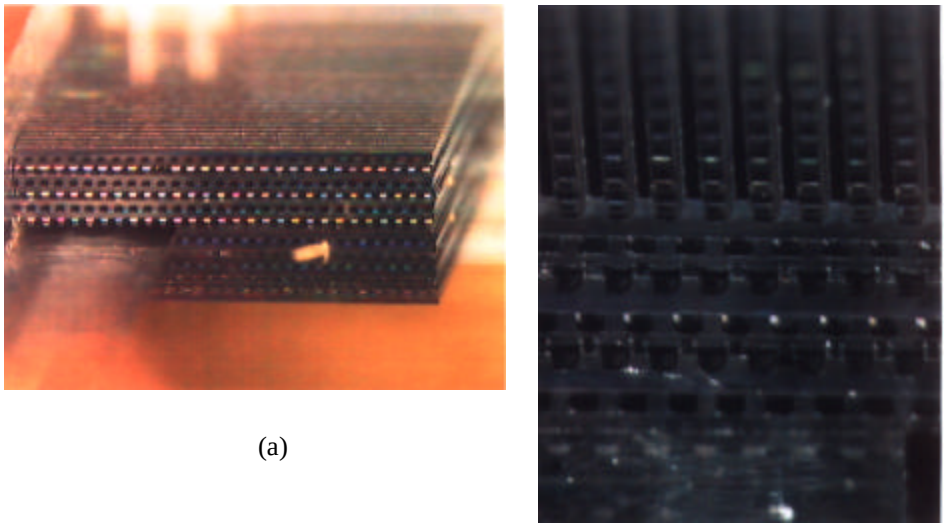

(a) (b)

Figure 5.11: Stacking of the Silicon wafer pieces. The shift between layers can be observed in b.

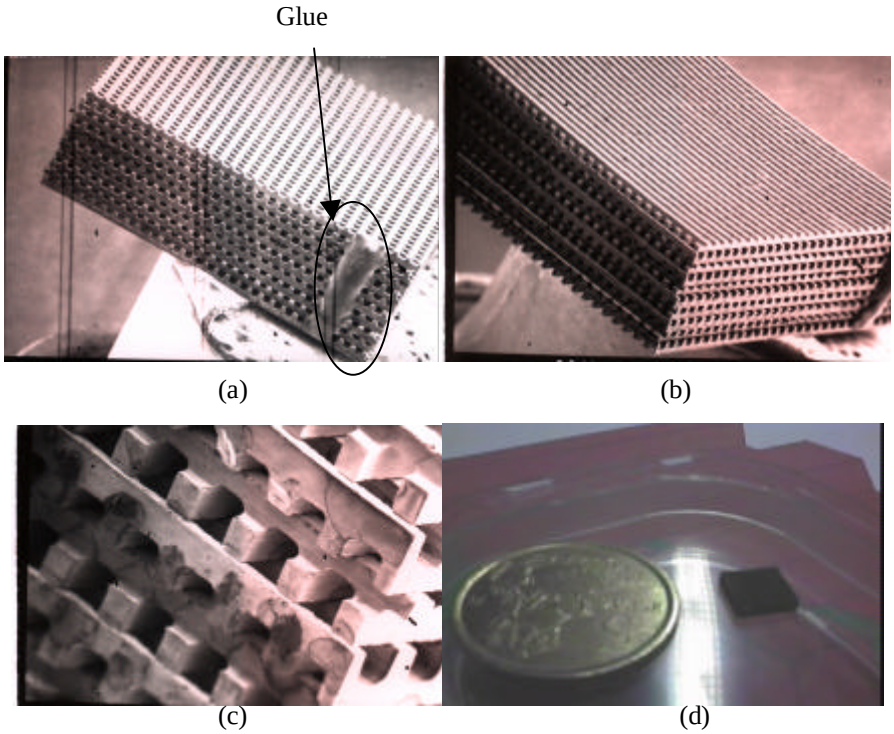

Figure 5.12: Gallery of pictures showing the fabricated woodpile Photonic Crystal.

5.3 Measurements of the Woodpile Photonic Crystal

There are various ways of determining the fabricated woodpile crystal structure's RF properties around 500 GHz. The simplest configuration could be formed by a broadband source emitting in the millimetre-wave range and a spectrum analyser with a frequency span up to around 600 GHz. In this case, direct measurements of the transmission parameter (S_{21}) of the woodpile could be carried out. Such a spectrum analyser presently does not exist so another measurement technique had to be considered. The terahertz free-space spectroscopy set-up, which uses frequency synthesisers, mixers and a simpler spectrum analyser has been already used with success [OZB 94b and OZB 94c]. However, at the Rutherford Laboratory, where the measurements were performed, an Interferometric technique was used to obtain the transmission features of the fabricated woodpile.

This technique was selected as a relatively simple system can be implemented which achieves the necessary bandwidth , however, signal to noise can be limited.

Different Interferometric systems can be used [LES 90], the Michelson Interferomer is a basic version. It consists only of a pair of plane mirrors and a semi-reflector used as a beam-splitter. Commonly, they are used in the ultraviolet and far-infrared regions as part of the spectrometers to measure the power frequency spectrum of the input signals.

This type of interferometer presents some limitations, which are solved by a Martin-Pupplet Interferometer, which consequently has been selected for measurements. The approach will be to use this Interferometer as Fourier Transform Spectrometer.

In this section, the selected configuration to perform the measurement s will be described. Moreover, the measured results using this configuration with a broadband source and a single frequency source will be presented. This section will be divided into the following sub-sections,

5.3.1) System configuration
5.3.2) Broadband measurements
5.3.3) Single frequency measurements

5.3.1 System configuration

The selected configuration is the Martin- Puplett Interferometer (M.P.I.). This configuration avoids the problems related to the use of conventional beam splitters where the reflectivity and transmissivity depend on the frequency of operation. Replacing the semi-reflector [LES 90] used in the Michelson configuration by a polarizer and the plane mirror by a modified reflector, called *roof mirror,* this problem is avoided.

Systems of this type are easy to analyse, and as a consequence, its performance can be predicted with confidence. They are also simple to build and are available covering a wide range of frequencies.

These systems have many applications, but here it will be used as Fourier Transform spectrometer. Basically, this two-beam interferometer produces a variation in the output detected power as a function of the path difference between

the two beams, which is produced in a controlled manner. The measured variation can then be Fourier transformed to obtain a measure of the signal power-frequency spectrum.

The building blocks of the MPI system are polarising grids and roof mirrors. The polarising grids are made of spaced parallel freestanding metal wires (usually made from stainless steel or tungsten). The diameters of the wires are arranged to be much smaller than the working wavelength while the spacing of the wires should be significantly less than a half of the working wavelength.

The roof mirror consists of two plane metal reflectors, placed so as to touch along one edge at an angle of 90º. The roof mirror is used instead of the conventional plane mirror to reflect the signal because it has the extra property of being able to rotate the plane of polarisation through an angle $2q$. Consider a plane polarised signal beam incident upon one of the mirror surfaces of the roof mirror with its electric vector aligned at an angle q to the roof line. Provided that the input is incident from a direction normal to the roof line, then the output will move away in the direction parallel to the incident beam with its electric vector realigns at an angle $-q$ to the roof line (see Figure 5.13).

In the configuration used, the electric field to the roof mirror has an incident plane of polarisation at an angle θ=45º with the roof mirror. The reflected field will thus have a plane of polarisation, which has been rotated to θ=-45º. The incident and reflected fields are orthogonally polarised. With this configuration, the entire signal moves towards the detectors, none of the input power is returned back towards the source (see Figure 5.14).

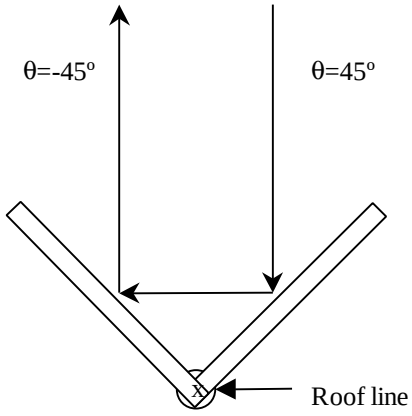

Figure 5.13: Change in the polarisation produced upon reflection by a pair of plane mirrors located in a "roof-mirror" arrangement.

The working of the MPI system is illustrated in Figure 5.14, in brief is as follows. The incoming signal is split into two equal components, which are recombined after being directed along paths of different lengths. The resulting output signal is modified in a way, which depends upon the path difference and the signal wavelength.

Any field incident to the polarizer can be considered as composed of two orthogonally polarised components, one with its electric vector parallel to the wires, and the other perpendicular to them. The perpendicular component will be transmitted through the polarizer, while the parallel one will be reflected.

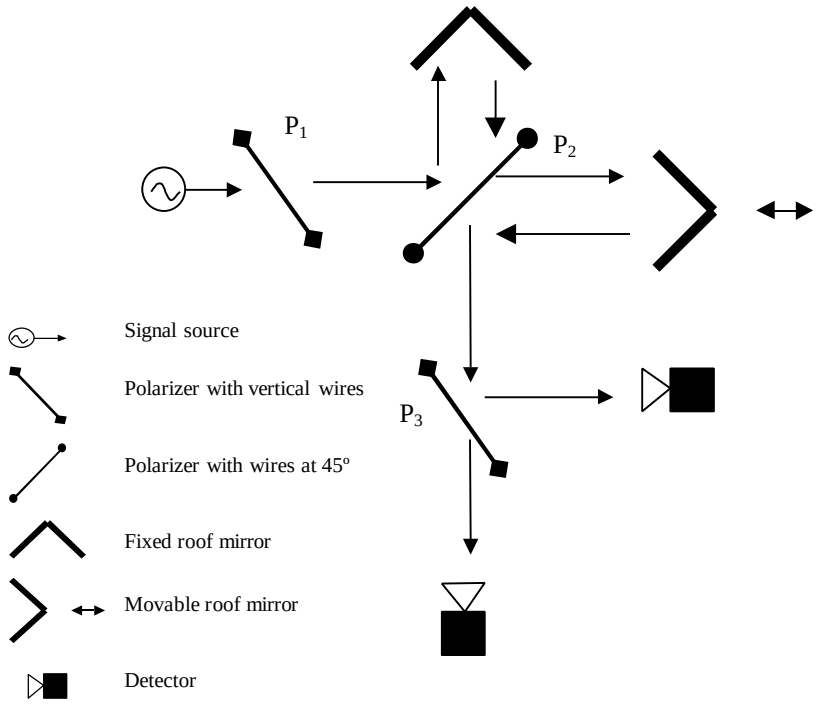

Figure 5.14: Diagram of a Martin-Pupplett polarising Interferometer.

Either a broadband or a single frequency can be considered. The two-beam interferometer seems more appropriate to be used in a broadband configuration. One can think that for the case of a simple system formed by the source, a polarizer, the DUT[1] and the detector would suffice. Nevertheless, it should be taken into account that the detector has a broadband response and that the source is

[1] D.U.T. : Device under test.

not pure as it is produced by harmonic multiplication from the fundamental oscillator. Therefore, in the case of single frequency configuration, contributions from higher harmonics from the source are detected reducing the signal to noise ratio of the system. To avoid this problem, the two-beam system will be also used in this case. This phenomenon will be described later.

Some modifications to the basic MPI configuration have been made in the selected measurements system. The most important one was to include two lenses in order to focus the beam in a smaller area. At the same time a 45º polarizer was included at the input point to obtain a reference value from the source to check if the signal level changed during the measurement process. Figure 5.15 illustrates the final configuration used. Some photographs of the system are presented in Figure 5.16.

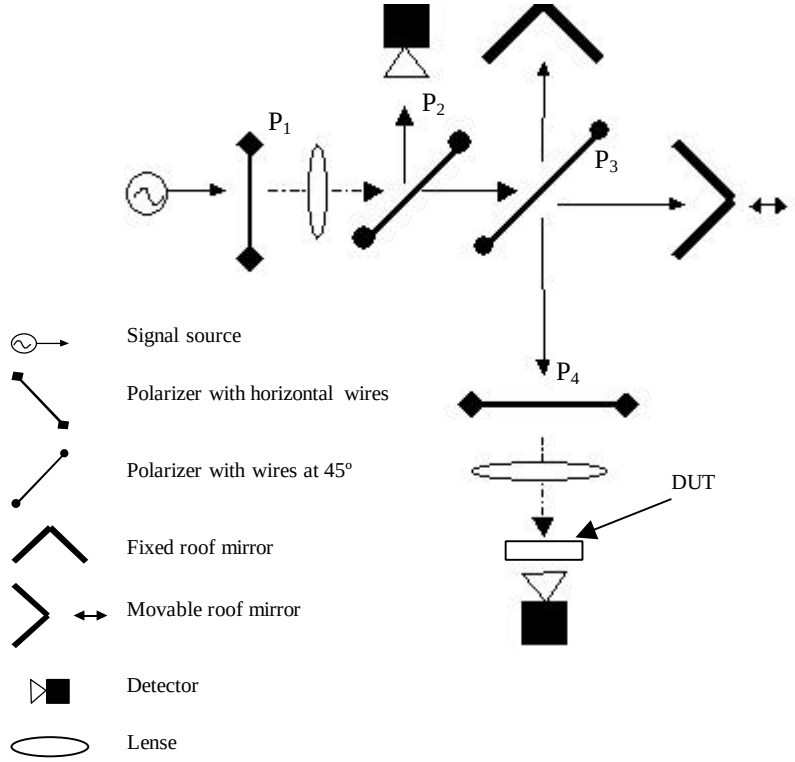

Figure 5.15: Diagram of the MPI configuration used in the measurements.

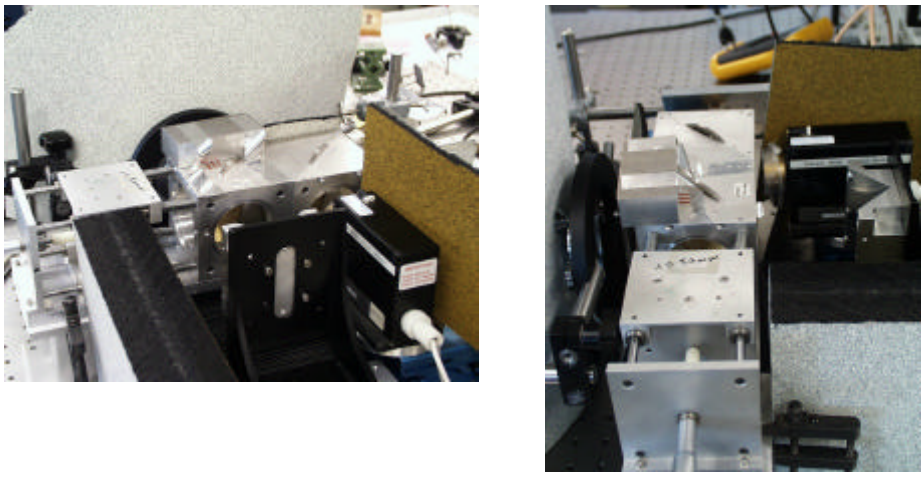

Figure 5.16: M.P.I. configuration used for the measurements.

As detectors, two different types were used. The first one was a *Golay detector*, which is a bolometric detector working at room temperature and the second one was a *HEB*[2] *bolometer*. Initially and according to the available resources, the Golay cell was used as detector, but due to its limitations it was necessary to finally use the HEB bolometer.

The Golay cell consists of an absorbing film placed inside a pressure cell. Signal power absorbed by the film is transferred by conduction to the gas inside the cell. The gas pressure inside the cell will alter in response to a change in the input signal power level. By measuring this change, the signal power is obtained.

The main disadvantages of the Golay cell are its poor response time and its sensitivity to mechanical vibration. A typical Golay detector needs about one second to respond correctly to the change in the input power. These devices are useful when high sensitivity is not required. The typical responsivity of a Golay detector is of $10^3 - 10^6\ V \cdot W^{-1}$ and a NEP[3] of around $10^{-10}\ W \cdot H^{-1/2}$. They can be used to measure power fluctuations down to a few tens of nanowatts at modulation frequencies up to 10-20 Hz.

[2] HEB: Hot-electron Bolometer

[3]Noise equivalent power (N.E.P.): this is the input signal power which is equal to the mean apparent fluctuation in the input power produced by noise (usually defined for a standard bandwidth of 1Hz).

The frequency response range of the Golay detectors goes from visible to the millimetre-wave regions, so care has to be taken to ensure the incident optical power is filtered out.

Due to the commented disadvantages of these detectors, a more sensitive and faster detector was also used, a cooled Indium Antimonide (InSb) Hot Electron Bolometer (HEB).

In a cooled InSb sample many of the electrons are weakly coupled to the crystal lattice, so they are able to move fairly easily around the crystal. Thus, any energy absorbed by the InSb will tend to change its electrical resistance, which allows the crystal to be used as bolometer.

The hot-electron effect means th e electrons act as if the crystal were hotter than its actual physical temperature because the input signal power raises the mean energy of these electrons just as if the crystal lattice temperature had been increased. These effects lead to this crystal to have a small conductance and thermal capacity of the electron gas. The combination of both produces a bolometer which has a high responsivity and a short response time.

The performance parameters of the InSb bolometer used in the measurements are ;

- Detector Electrical Responsivity >5000 V/W
- Detector Electrical N.E.P. $<5 \times 10^{-13}$ $WHz^{-1/2}$
- Spectral Bandwidth 60 GHz to 3 THz
- Typical Operating Resistance 5 to 10 kΩ
- Operating Temperature 4.2 K or below.

The N.E.P. and the responsivity parameters are referred to a 4.2 K detector exposed to a 300 GHz signal modulated at 1 kHz.

Calculating the N.E.P. ratio between the Golay cell and the HEB bolometer, an improvement of 23 dB is obtained using the HEB bolometer, working under the same measurement conditions.

The cryogenic details of the detector are given below,

- Liquid Helium Hold-time >80 hours
- Liquid Nitrogen Hold-time >24 hours

The set-up used to measure the woodpile Photonic Crystal features is as depicted in Figure 5.17. The MPI system is fed using a broadband or single frequency chopped signal. A digital positioning system (DPS) controls the movement of the movable roof mirror. A lock-in amplifier retrieves the output power of the system. A computer, via GPIB, is controlling the DPS and reads the output power from the lock-in amplifier. Figure 5.18 shows a photograph of this set-up. In this computer, a code developed under the Labview environment was implemented to process the input data and obtain the Fourier Transform.

The chopper system was used in order to increase the signal to noise ratio by engaging in phase the lock-in amplifier and the chopper.

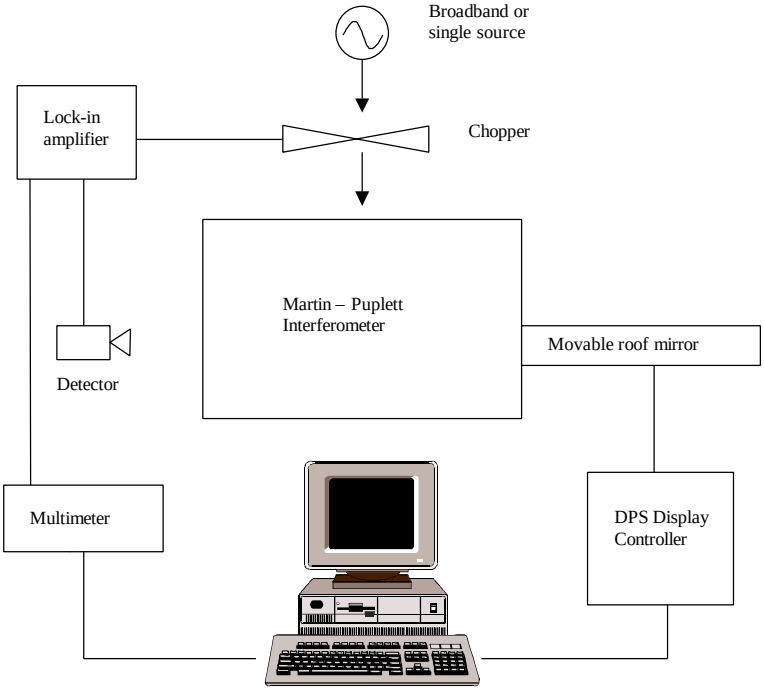

Figure 5.17: Set-up configuration used in the measurement procedure.

Figure 5.18: Photograph of the set-up used in the measurement process.

5.3.2 Broadband Measurements

After defining the configuration of the system and its performance, the results obtained by using a broadband source will be presented. The idea of using a broadband source was to reasonably characterise the complete performance of the woodpile Photonic Crystal by only doing one measurement. The advantage is the short period of time required to obtain the woodpile crystal structure behaviour.

Ideally, a thermal source radiates as a black body which radiation intensity S, obeys the Planck equation,

$$S = \frac{2hn^3 / c^2}{\exp(hn / kT) - 1} \tag{5.3}$$

where S is in $W \cdot m^2 \cdot Hz \cdot \Omega^2$, T is the physical temperature of the source in Kelvin's, k is the Boltzmann's constant, h is the Planck's constant, ν is the signal frequency and c is the velocity of the light.

Two possible broadband sources were considered. A hot load which source was a lamp (about 1000K) and a cold load which source was by liquid-nitrogen at

77K. The hot source presented the problem that the radiating peak was close to infrared frequencies with very low power in the millimetre-wave frequency range and was not considered any further. So, only measurements with the cold source were performed.

The set-up used for these measu rements was presented in Figure 5.17. In this case, a polarizer is used after the source in order to select only one polarisation (the source is not polarised). The MPI configuration is the same than the one shown in Figure 5.15.

The procedure consists, first of all, of making the measurement without the woodpile structure in order to characterise the system (reference "background"), and, after that, to proceed with the measurement in transmission through the woodpile Photonic Crystal. The ratio between the two measurements is the insertion loss of the structure.

The woodpile Photonic Crystal sample was placed just in front of the detector. As the sample size was fixed to 9x9mm, and the input radius of the detector window was bigger, a metallic plate with a 6mm hole was placed between the detector and the last polarizer (see Figure 5.19). The input signal to the detector propagates through this small aperture (6mm). Via use of the lenses in the M.P.I., the beam was focused to a beam waist of 6mm. With this configuration, a direct comparison between the power with and without the woodpile was carried out.

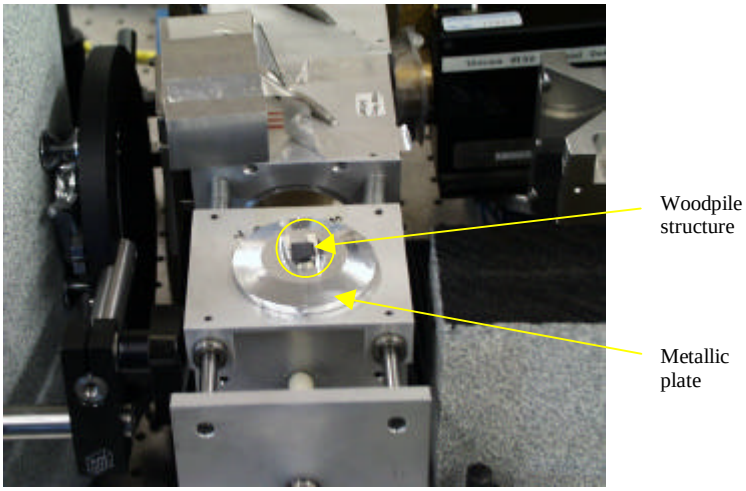

Figure 5.19: Woodpile crystal structure on the 6mm metallic plate.

The interferometer results are shown in Figures 5.20 and 5.21. Note that the maximum power in the detector is obtained when the path through the two roof

mirrors is the same, because, for this case, all the frequency components are added in phase. This will be the starting point to initialise the interferometric process. To obtain the spectral information of the DUT, the selected resolution was fixed to 4 GHz and the span to 2 THz. The span defines the maximum distance to be moved for the movable roof mirror and the resolution determines the step between measurement points (see Appendix C).

It should be noted that during the measurement process, the orientation between the first layer of bars in the woodpile and the polarisation direction of the incident electric field was not noted because a degenerate behaviour was expected from the theoretical results. Nevertheless, as it will be shown in the single source measurements, a different behaviour as a function of the orientation was obtained.

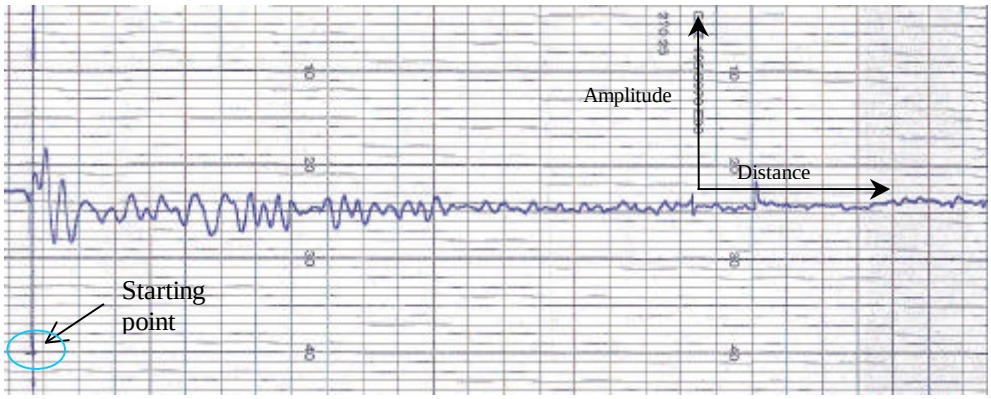

Figure 5.20: Interferometer result for the broadband source emission (Liquid Nitrogen). The starting point of the interferometric process is shown. The scales of the plot are 1V/div (amplitude) and 3cm/min (distance).

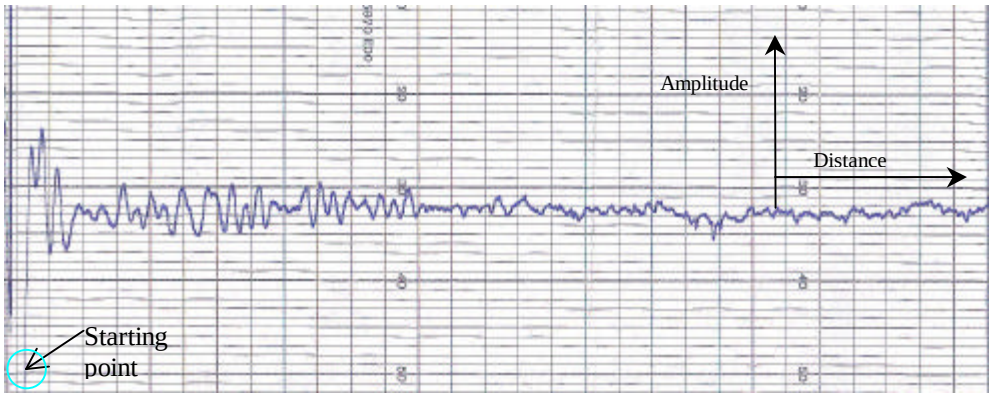

Figure 5.21: Broadband interferometer result when the woodpile crystal structure is placed at the detector input. The scales of the plot are 1V/div (amplitude) and 3cm/min (distance).

Applying the FTS[4] over the previous interferometer data, the emission frequency spectrums with and without woodpile are obtained (see Figures 5.22 and 5.23).

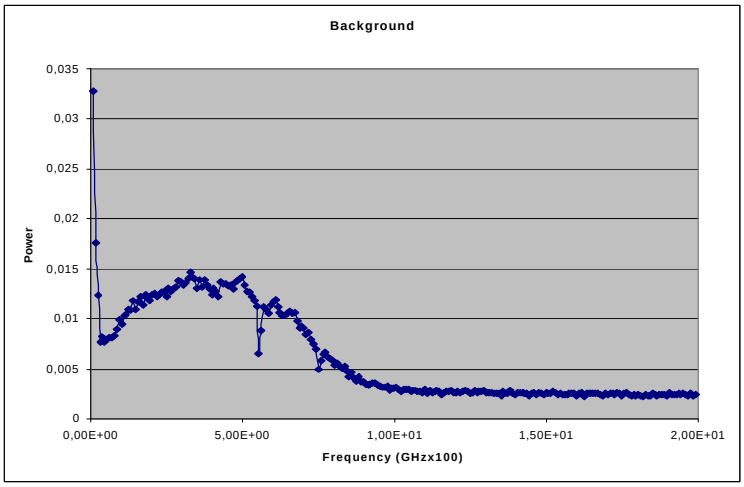

Figure 5.22: FTS of the broadband source (liquid Nitrogen) using as detector the Golay cell.

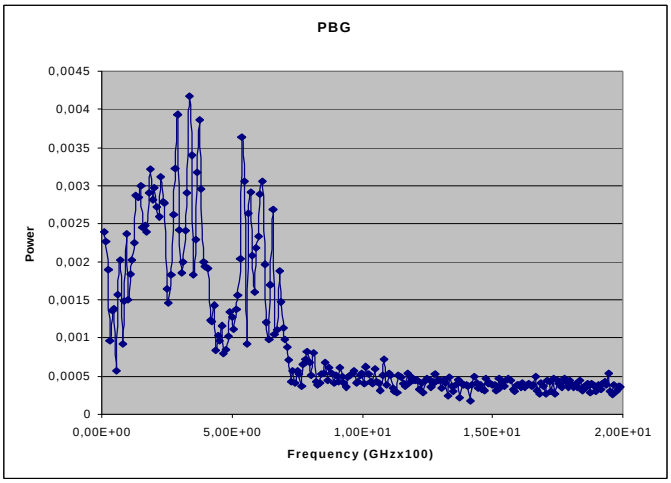

Figure 5.23: FTS of the broadband source (liquid Nitrogen) with the Photonic Crystal structure using as detector the Golay cell.

[4] Fourier Transform Spectrometer

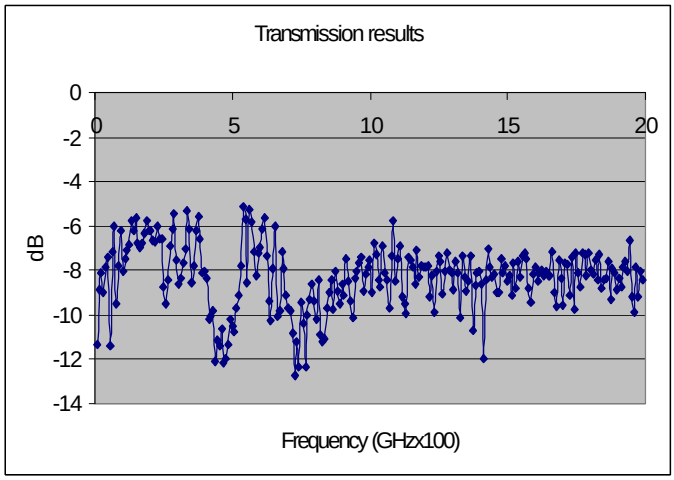

Figure 5.24: Insertion loss of the woodpile structure when the detector is the Golay cell.

Only the results obtained with the Golay cell as detector are shown because the noise of the system and the low power emitted by the broadband source were such that the HEB bolometer detector did not offer better performances. In conclusion, the transmission plot (see Figure 5.24) displays a band gap around 500 GHz, as expected indicating that the woodpile crystal is properly designed. The main problem is the dynamic range, which is very poor, because the transmission power from the source was very low, limiting the possibility to obtain a very good signal to noise performance.

Although the dynamic range is limited, thi s initial measurement provides a useful verification of the performance of the woodpile. A full spectral measurement can be carried out in a short period of time and information about the gap region can be quickly extracted.

5.3.3 Single frequency measurements

Due to the dynamic range limitations of the broadband frequency measurements, a single frequency source was used. The main advantage of this technique is the dynamic range achieved. The main disadvantage is the measurement time required. A measure of the background and the woodpile Photonic Crystal has to be performed for each frequency value.

As input source a Backward-Wave Oscillator (BWO) was employed, which operating frequency range goes from 75 to 110GHz . In order to cover all the desired measuring frequency range (300-600 GHz), different harmonics of a

multiplier were used. In this case, the chopping of the signal was performed electronically. (Two photographs of this configuration are shown in Figure 5.25 and 5.26). This electronic chopper increases the signal to noise ratio by reducing the noise of the system.

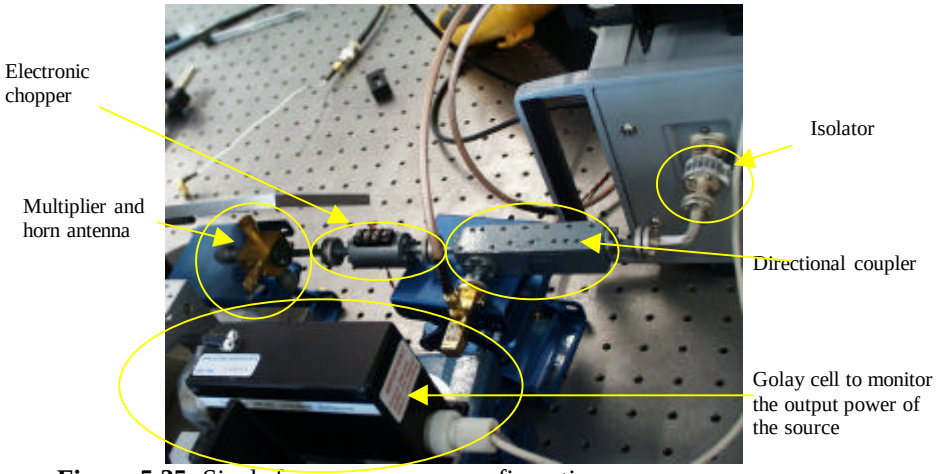

Figure 5.25: Single frequency source configuration.

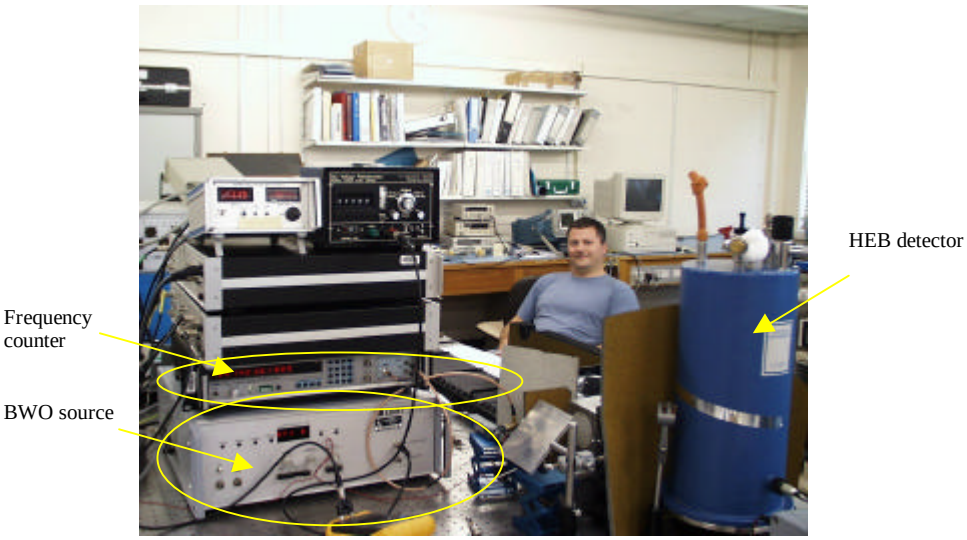

Figure 5.26: Feeding system for the single frequency source configuration.

All the measurements were obtained using the HEB bolometer as detector. At the same time, a configuration to check any variation on the source output power was implemented during the entire duration of the measurements (see Figure 5.15). The objective was to check if the source was affected by reflected power through the MPI system. To perform this control operation, the Golay cell detector was used to monitor the source output power (see Figure 5.25). Apart from this, the measurement set-up was the same as the broadband case.

The woodpile structure was placed either with the stacking direction parallel to the incident plane wave (parallel PBG), or perpendicular to the direction of the incident electric field (perpendicular PBG). By rotating the woodpile crystal an angle of 90º on the measurement system, the parallel PBG configuration is converted into the perpendicular PBG configuration.

As example the performance of a single source emitting 500 GHz will be developed. The interferometer results as function of the roof mirror movement are shown in Figures 5.27 (reference background), 5.28 (parallel PBG) and 5.29 (perpendicular PBG). The selected span and the frequency resolution used in Figures 5.27 to 5.29 were 800 GHz and 1 GHz respectively. As it was expected from theoretical predictions (see Appendix C), for a single frequency source, a sinusoidal behaviour is obtained as interferometric result (see Figure 5.27). Due to the attenuation in free space, the detected power is reduced when the distance of the movable roof mirror is increased.

Using a program developed in Labview, the Fourier Transform of these interferometric results was obtained. The FTS results for each case are shown in Figures 5.30, 5.31 and 5.32.

Looking at the spectrum plot, besides the main frequency component (in this case 500 GHz), the following harmonics, which are placed at 600 GHz, 700 GHz, appear. By using these harmonic components, more than one frequency point can be calculated at the same time .

With these results, it is easy to calculate the insertion loss by performing the ratio between the background result and the parallel or perpendicular PBG result, for the working frequency and its main harmonics (see table 5.2 and 5.3).

Frequency (GHz)	Background (1mVx2)	Par. PBG (1mVx2).	Perp. PBG (10mVx5)
500	6.85	0.147	0.654
600	0.381	3.63	4.57

Table 5.2: Harmonic power values with its respective scales for the background, parallel PBG and perpendicular PBG configurations.

Frequency (GHz)	Parallel PBG	Perpendicular PBG
500	-46.7	-26.2
600	-20.2	-5

Table 5.3: Insertion Losses (dB) for the woodpile Photonic Crystal as function of the first layer orientation.

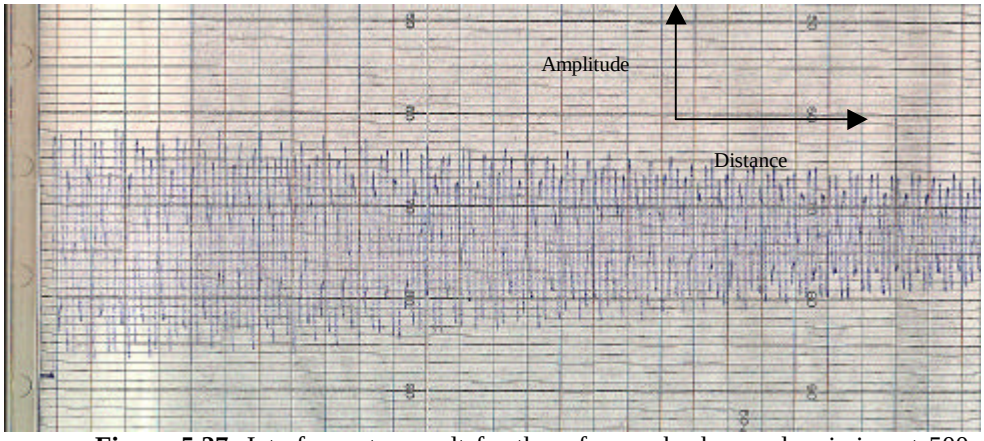

Figure 5.27: Interferometer result for the reference background emission at 500 GHz. The plot scales are 1V/div in amplitude and 3cm/min in distance.

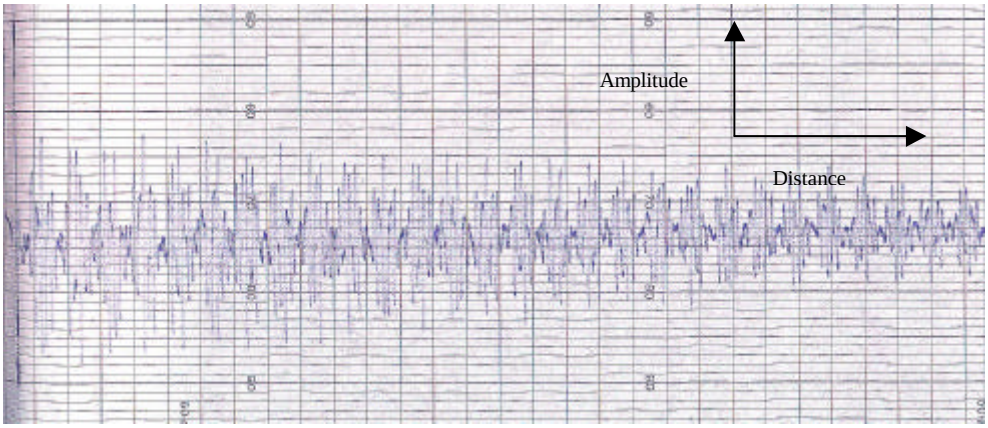

Figure 5.28: Interferometer result for the parallel PBG at 500 GHz. The plot scales are 1V/div in amplitude and 3cm/min in distance.

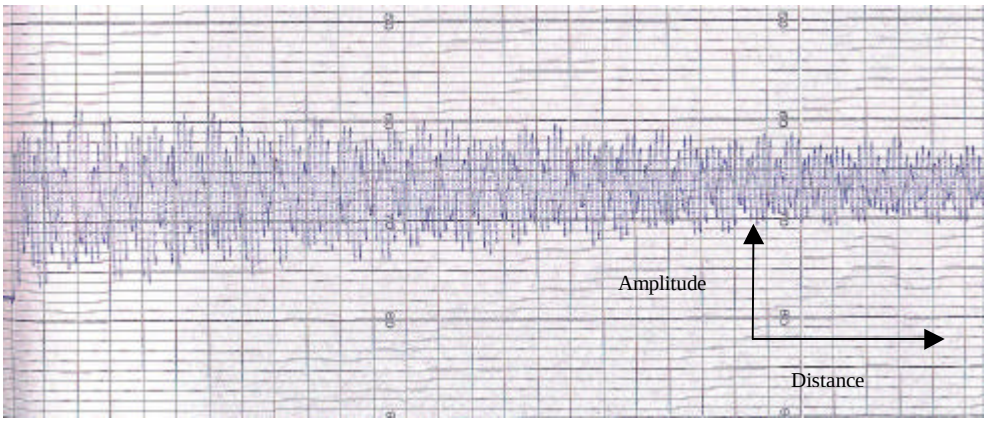

Figure 5.29: Interferometer result for the perpendicular PBG at 500 GHz. The plot scales are 1V/div in amplitude and 3cm/min in distance.

From the previous figures, a lack of the high purity sinusoidal behaviour for the parallel and perpendicular PBG interferometric cases is observed, indicating that the majority of the signal has been filtered out by the woodpile structure. In addition, it can be seen that the sinusoidal periodicity of the trace is lower with the woodpile Photonic Crystal present in the beam than without, indicating that more high frequency components are reaching to the detector. This behaviour is readily observed from the Fourier transform of the spectrograph.

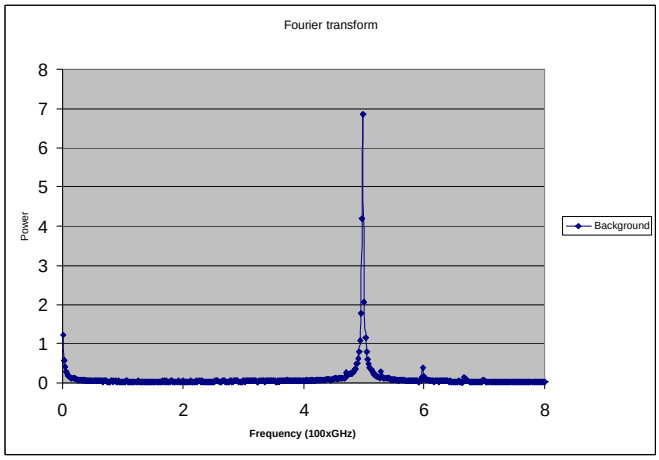

Figure 5.30: FTS of the background interferometer result at 500 GHz. Scale, 1mVx2.

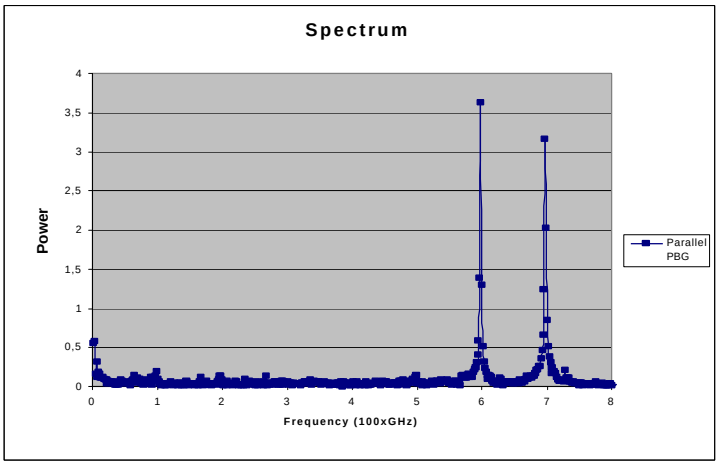

Figure 5.31: FTS of the parallel PBG interferometer result at 500 GHz. Scale, 1μVx2.

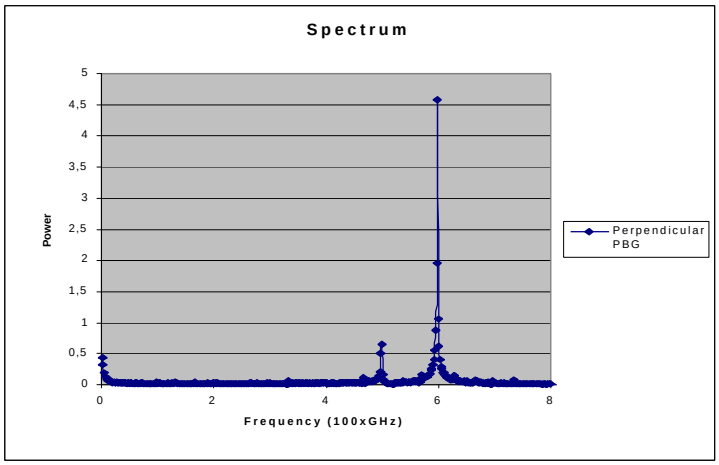

Figure 5.32: FTS of the perpendicular PBG interferometer result at 500 GHz. Scale, 10μVx5.

Figure 5.30 shows a clear peak at 500 GHz, the main component of the source, together with two smaller ones at 600 GHz and 700 GHz, which correspond to the source harmonics. Figure 5.31 shows only the 600 GHz and 700 GHz components because the Photonic Crystal is reflecting almost completely the 500 GHz component. In Figure 5.32, the main component at 500 GHz remains with some power, indicating that the Photonic Crystal behaviour for the perpendicular orientation at that frequency is not as good as for the parallel one.

These results clearly show the necessity of using a spectrum analyser as implemented by the MPI to calculate correctly the insertion loss for each single frequency value.

Repeating this process for all the points in the frequency range under study, a plot of the insertion loss as function of frequency for each PBG orientation was determined. The result is depicted in Figure 5.33.

It should be noted that the acquisition of frequency points between 450 GHz and 600 GHz was relatively easy by using the same multiplier, while obtaining values for other frequency points was more difficult. Different harmonics of the multiplier were used in the calculation of the remaining frequency points.

From 380 GHz to 450 GHz, no frequency points were measured. This was because of limited measurement time available. Also, unfortunately after three days working with the HEB bolometer, the Helium was depleted, and it was impossible to cool the HEB again in order to continue with the rest of the points.

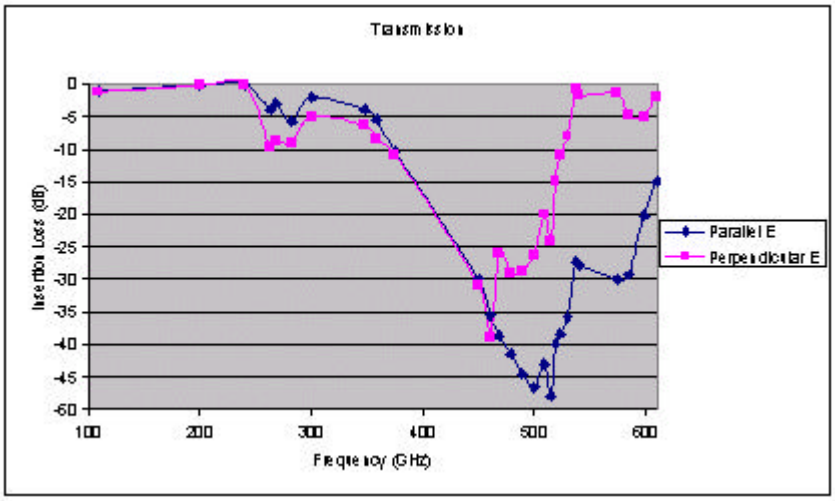

Figure 5.33: Transmission results for normal incidence to the woodpile crystal structure. The parallel and perpendicular orientations results are shown.

From Figure 5.33, it can be observed that the transmission results depend on the incidence polarisation. As it was explained in the woodpile design section (see Figure 5.3), the behaviour as function of the incidence polarisation should be the same. This discrepancy between theoretical predictions and measurements is due to the fact, as it was commented in the fabrication section, the bar height is different for each incidence polarisation. One polarisation encounters bars of 75

μm height, and the other one of 65 μm. This is producing a shift in the transmission parameter S_{21} of one polarisation in relation to the other one. The bars with lower height lead to a higher frequency response.

In order to demonstrate this behaviour, a n analysis of the actual manufactured structure has been performed. Figure 5.34 shows the woodpile structure in which the fabrication defects have been included and Figure 5.35 shows the transmission results for each one of the polarisations obtained using the HFSS program. These theoretical results are confirming the measurements. So, it can be concluded that the difference as function of the incidence polarisation is due to the fabrication process error.

The structure simulated tries to reproduce the fa bricated errors, but as the inclination angle on the table is unknown, for the simulation, a smooth cut of 90 μm and another one of 80 μm generating bars of 65 and 75 μm in height have been assumed. These values of the bars correspond with a 17% and 3% deviation respectively on the theoretical dimensions.

Now, the behaviour of this "new" woodpile structure should be confirmed for all the angles of incidence. By using the plane wave program and taking into account the fabrication process, the analysis was performed, obtaining the results shown in Figure 5.36. In this figure, a reduction in the band gap width is reported. The total band gap is about 3 % in comparison with the 11% of the initial design. This feature will have to be taken into account for the antenna design.

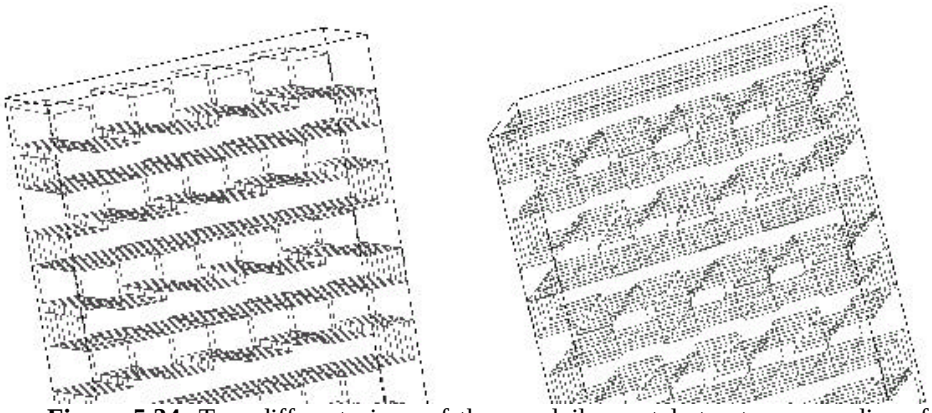

Figure 5.34: Two different views of the woodpile crystal structure as replica of the fabricated one.

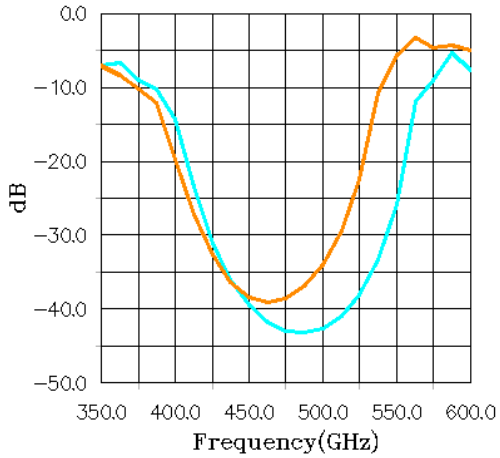

Figure 5.35: Transmission parameters S_{21} of the woodpile structure depicted in the previous figure. The blue line is the perpendicular polarisation and the orange is the parallel one.

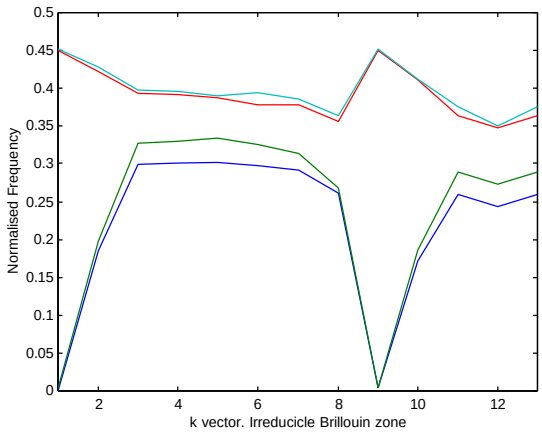

Figure 5.36: Dispersion relation for the manufactured woodpile structure. A total of 3456 plane waves were analysed.

5.4 Dipole Configuration and results

In this section the design of a dipole to place it on top of the woodpile designed in the previous sections will be presented. In addition, the simulated radiation pattern of this configuration will be shown. The fabrication of the dipole has been also performed at RAL , some pictures with the fabricated configuration will be shown.

There are several works about the radiation of a dipole on top of a woodpile Photonic Crystal structure, these can be found in [CHE 95, SIG 96, SIG 97, SMI 99 and SIG 99], however all of them have been carried out at much lower frequencies. Here, the goal is to design and fabricate the dipole on top of the woodpile structure working in the millimetre wave region. It should be noted that new configurations based on using resonant cavities to obtain high directivity dipole antennas with values of 23 dB has been recently proposed [OZB 00].

The selected fabrication method was determined by the lithographic facilities at RAL. As the selected working frequency was 500 GHz, the design dimensions were limited by the minimum lithographic resolution to generate the mask. This resolution is defined by the UV (ultraviolet) spot, which has a minimum value of 10x10 μm.

The design of the dipole is influenced by the measurement technique. As the availability of measurement equipment at 500 GHz is quite complicated, another solution had to be used. Here, it is proposed to place a detector in the dipole antenna to convert the incoming signal at 500GHz to a DC value, which can be easily measured. The DC value will change as function of the detected power.

There are different devices to be used as detectors on the antenna , in this case, a Schottky diode was selected due to its very good performances (high sensibility values) at high frequencies. The Virginia University via RAL has provided the Schottky diode.

The dipole feeding is made by using a transmission line. A low pass filter has to be put between the dipole antenna and the DC detector in order to isolate the RF from the DC. A dielectric membrane will support the feeding line. This membrane has to be manufactured as thin as possible to avoid surface wave mode propagation. It should be noted that this membrane is not placed under the dipole, remaining this on air.

With all these requirements the final design is depicted in Figure 5.37(a). The end blocks have been designed to collect the DC power. The fabricated dipole has been manufactured in gold on a membrane (see Figure 5.37(b)).

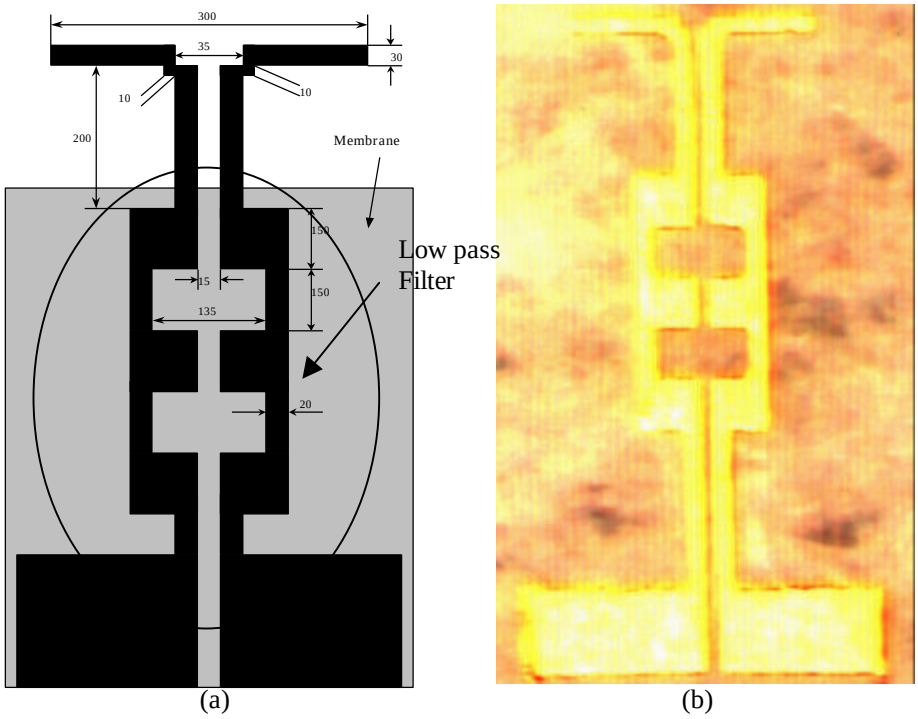

Figure 5.37: (a) Schematic drawing of the dipole and filter. All the values are in μm. (b) Fabricated dipole on a membrane.

Simulations using the HFSS software were performed. As this code does not allow implementation of an active element, the simulations were carried out without considering the diode. The filter was neither taken into account because the transmission line is feed at 500 GHz, and the filter would not allow the propagation of this signal. The simulated configuration is displayed in Figure 5.38. Four periods in the *x-y* plane and four periods in the stacking direction (*z*) were used for the woodpile structure.

There are two high symmetry positions in the unit cell corresponding to the antenna: (a) in a solid position on top of the bar, that is, intersection of the first and second layer of bars, or (b) in the void position with no dielectric bar directly beneath it, but above the third and fourth layers of bars. For each of these two surface positions there are two orientations, corresponding to the dipole parallel or

perpendicular to the first layer of bars. This implies a total of four different configurations for the antenna in the unit cell.

From the developments carried out in [SIG 97] it is concluded that the parallel configuration offers better performances than the perpendicular one. For this configuration, there are still two options, the solid and the void one. Finally, the dipole was simulated placed on top using the void configuration (see Figure 5.38) because, it is expected from [SIG 97] that both of them give the same trends.

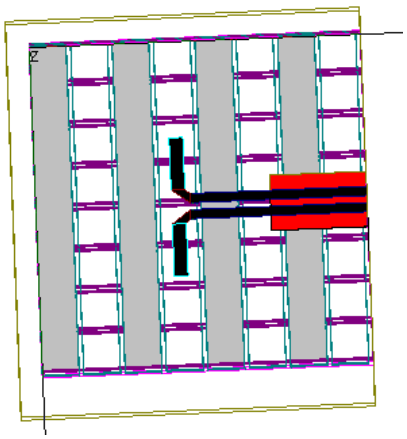

Figure 5.38: Dipole structure on top of the woodpile Photonic Crystal. The red part shows the membrane. The grey colour represents the first layer of bars.

The radiation patterns are presented in Figures 5.39 and 5.40. The th ree-dimensional pattern shows a high rotationally symmetry with low back radiation levels, which can be confirmed from the E and H plane cuts. The front-back ratio has been reduced by 20 dB and the symmetry of the beam is maintained $\pm 30^{\circ}$. These results are very promising to obtain very good radiation performances from a dipole.

A comparison between the radiation patterns from a dipole in air and the previous results were performed, the idea was to prove the advantages of this configuration. The results are depicted in Figure 5.41 and the improvements are impressive. The directivity has increased in 6 dB and a clear reduction in the back radiation has been obtained.

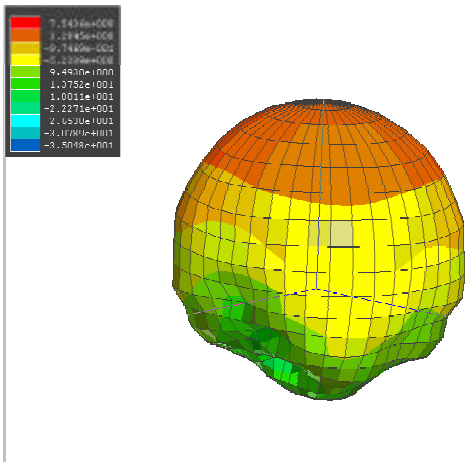

Figure 5.39: Three-dimensional radiation pattern of the dipole on top of the woodpile Photonic Crystal.

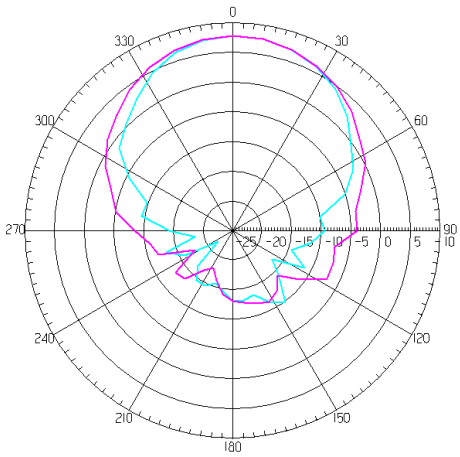

Figure 5.40: Radiation pattern for the E (pink) and H (blue) planes.

After the simulations, the dipole antenna was fabricated , the Schottky diode was soldered to the dipole (see Figure 5.42). The diode is mounted on a Gallium Arsenide (GaAs) membrane, which, as it can be seen from Figure 5.42, is quite large. As this structure can alter the behaviour of the radiation patterns from the dipole, new simulations were performed taking into account this membrane. The results are displayed in Figure 5.43. The general behaviour of the pattern is not modified. The symmetry of the beam is still maintained, only the H plane seems a little bit deteriorated. The front-back ratio is about 20 dB and the directivity has reached a value of 5 dB (1 dB less than the previous case). In general, the performances of the patterns are quite similar.

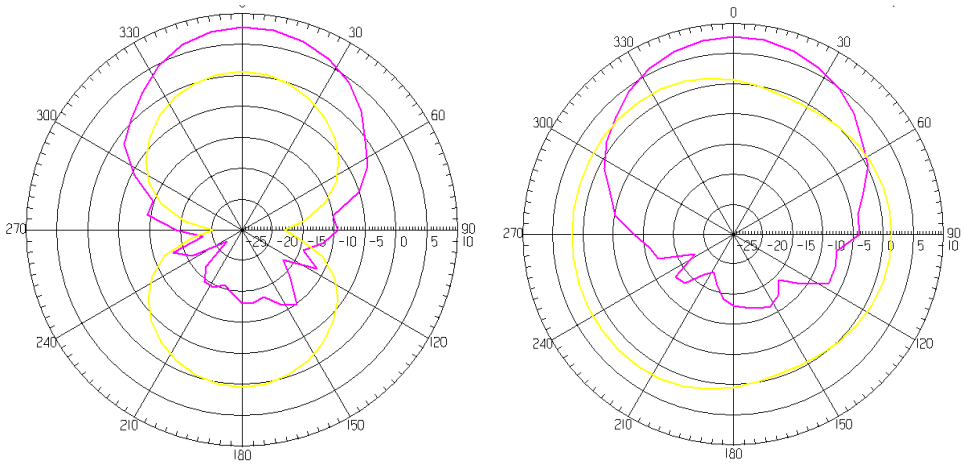

(a) (b)

Figure 5.41: Comparison between the radiation pattern of the dipole on air and the dipole on top of the woodpile Photonic Crystal for the E (a) and H (b) planes.

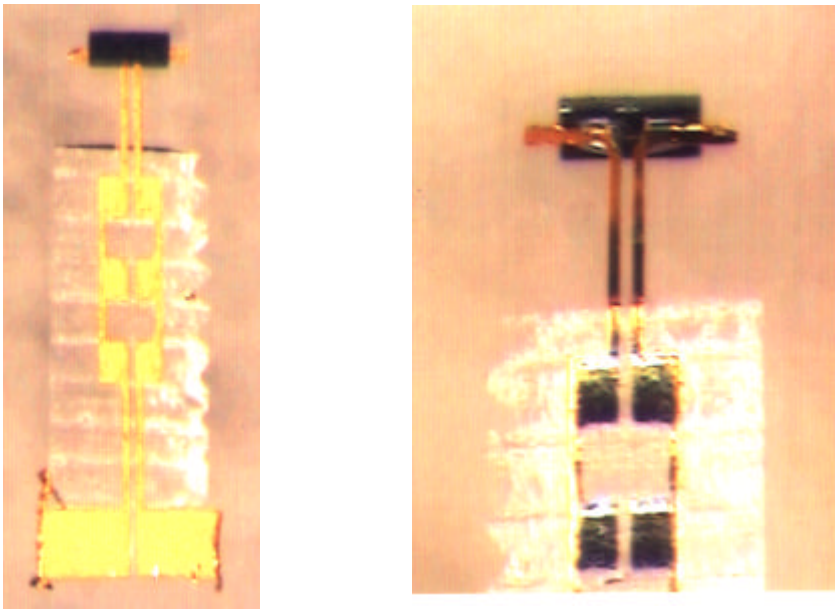

Figure 5.42: Dipole antenna with the Schottky diode.

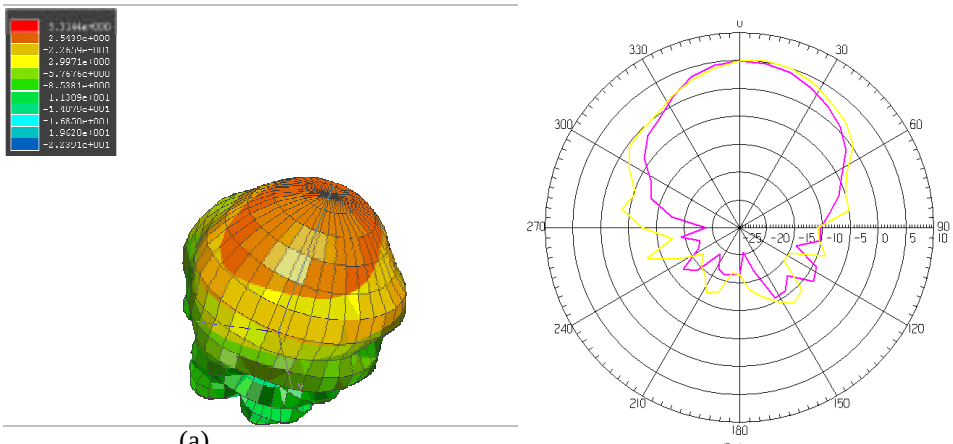

(a) (b)

Figure 5.43: (a) Three dimensional radiation pattern of the dipole antenna on top of the woodpile Photonic Crystal taking into account the diode membrane. (b) E (pink) and H (yellow) plane cuts.

Finally, in Figure 5.44 the fabricated structure of the dipole on top of the woodpile Photonic Crystal is presented. The photographs were taken using an electron microscope. The woodpile, the antenna, the filter, the membrane to support the feeding line and the Schottky diode are clearly visible.

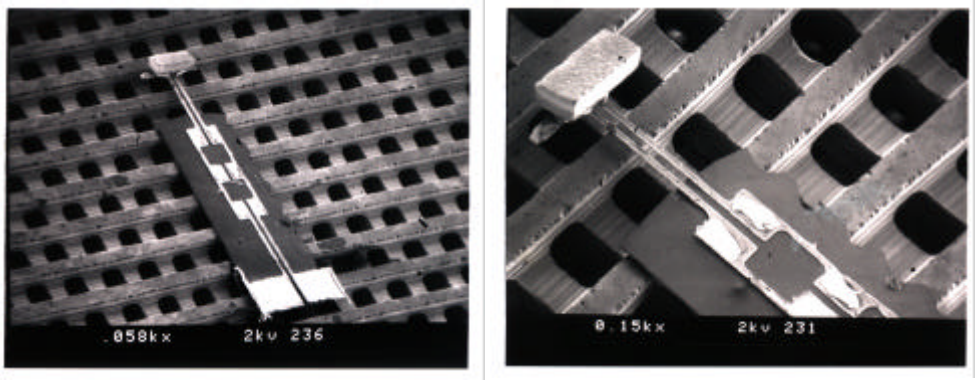

Figure 5.44: Photographs taken with the electron microscope showing the fabricated dipole on top of the woodpile Photonic Crystal.

It should be pointed out that the fabrication was performed without studying the impedance matching among the dipole, the filter and the Schottky diode, which will be translated in a low receiving efficiency and low Gain value.

CHAPTER 6

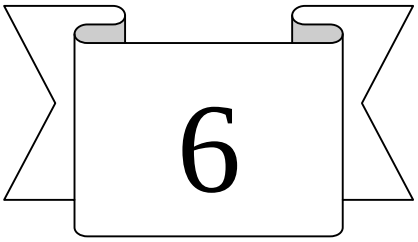

GENERAL REMARKS AND FUTURE RESEARCH

In this final chapter, the most relevant results derived from the research contained in this dissertation will be summarised. Some recommendations for future research will be provided subsequently.

6.1 General remarks

The main goal of this dissertation has been to use the new concept of "Photonic Crystal" structures as substrates in antenna configurations at microwave and millimetre wave in order to suppress or reduce the surface wave mode propagation. This fact has lead to a decrease of the loss mechanism, an increase in the antenna efficiency and an improvement of the radiation pattern of the antennas.

First the Maxwell's equations for dielectric period structures have been presented in Chapter 2. With these equations, an eigensystem has been formulated to solve for the eigenvalues and eigenmodes of any Photonic Crystal in one, two or

three-dimensions. The solutions offer the dispersion relation of the periodic structure, which characterise completely the behaviour of any Photonic Crystal. These dispersion relations provide the information to determine a full or a partial band gap.

A code to solve the eigensystem has been implemented. Using this software a complete study of different Photonic Crystal configurations in one, two and three-dimensions has been performed in Chapter 3. Initially, the study of the one-dimensional Photonic Crystals performances helps to understand the appearance of the band gap in periodic structures. Later, the features of two well-known different arrangements of two-dimensional lattices, a square and a triangular-hexagonal ones, have been analysed in terms of the dispersion relations, eigenmodes, energy distributions, gap maps and the dependence of the gap on the dielectric constant value.

Two three-dimensional Photonic Crystals have been presented in Chapter 3. The first one is the layer by layer or woodpile structure. A study of the gap as function of the parameters of the unit cell has been performed. Besides, a new three-dimensional structure has been proposed, this presents the advantage of being very easy to manufacture although up to now the obtained gaps are quite small. This structure has been patented.

After the extensive analysis carried out in Chapter 3, Chapter 4 and 5 focus on using Photonic Crystal to avoid the propagation of the surface wave mode in antenna configurations replacing the conventional substrates for Photonic Crystal substrates. Initially, a two-dimensional configuration is employed in microstrip technology. In this technology, a patch antenna is analysed, comparing the conventional substrate features versus the Photonic Crystal substrate ones. The effect of the finite thickness of the substrate has been analysed. As conclusion, it is not possible to obtain a complete gap, because of the appearance of radiating modes. Nevertheless, in the different cases studied, the effect of these radiating modes does not alter too much the radiation pattern, only a small peak appears in the E-plane.

In general, improvements of the radiation patterns have been obtained by reducing the surface wave mode excitation. The back and the end-fire radiation are clearly improved and the primary radiation is smoother. The first step towards array configurations has been made. The E and H coupling between two patch antennas has been analysed. Improvements of 18 dB and 15 dB reductions in mutual coupling respectively have been obtained. For all the cases, surface wave plots with the electric field distribution have been displayed, these plots provide an easy way to demonstrate how the surface wave mode propagation is filtered out.

Due to the increment of space projects at millimetre wave regions, a new configuration based on using Photonic Crystals structures as an alternative to the integrated antennas is proposed and analysed in Chapter 5. The selected antenna was a dipole, therefore a three-dimensional Photonic Crystal seems the best option as substrate. In this Chapter, the woodpile structure was analysed. A new fabrication method has been employed to manufacture the structure at 500 GHz. The normal incidence transmission measurements of the structure are in good agreement with the simulations. Nevertheless, a different behaviour as function of the polarisation (TE or TM) of the incoming wave has been obtained as a result of a fabrication problem. This problem has been solved for the manufacturing of future structures.

In addition, a dipole to be placed on top of the woodpile Photonic Crystal has been designed and fabricated. The simulated radiation patterns have been calculated. A high symmetry beam with very low back radiation has resulted indicating that the structure works quite well as surface wave suppresser. These results show that this technology could be a good alternative to the conventional horn antennas and the integrated lenses as front-end for millimetre wave applications.

As final conclusion, the potential of these Photonic Crystal structures as suppresser of surface wave modes in different technologies has been proven. Improvements in all the main radiation parameters (efficiency, directivity values, front-back ratios, mutual coupling) have been reported. These structures offer very good performances with very low technological efforts. The obtained results for microwave and millimetre wave antennas indicate that this technology is one of the most exciting fields of research in the next future with many potential applications.

6.2 Guidelines for future research

After validating the working of a Photonic Crystal substrate as suppresser of surface wave modes with a single antenna with different technologies (patch and dipole antennas), a logical next step is now to go to array configurations. The future research should be oriented to analyse, design and fabricate array of patches with low loss, high efficiency and higher directivity values. Now that the effect of surface wave mode can be minimised, the use of high dielectric materials will not be a problem. Using high dielectric materials a great number of periods can be placed between adjacent antennas, leading to very low coupling values.

New configurations based on slot antennas to avoid the radiating modes could also be studied as an alternative to patch antennas. In addition, this configuration allows the use of other two-dimensional Photonic Crystals, which could minimise the lattice period.

The use of resonant cavities in patch antenna configurations to obtain high directivity antennas and reduce the mutual coupling is another area of interest to be studied in the future.

Arrays of dipoles on three-dimensional Photonic Crystals are proposed as a possibility to design and fabricate imaging cameras. A more complete study of the new three-dimensional structure showed in Chapter 3 should be performed in order to replace the woodpile Photonic Crystal employed in Chapter 5.

REFERENCES

[AGI 94] Agi, K., Brown, E. R., McMahon, O. B., Dill, C., and M., Malloy, K., J., "*Design of ultrawideband photonic crystals for broadband antenna applications*", Electronics Letters, Vol. 30, No. 25, pp. 2166-2167, 8th December, 1994.

[AGI 96] Agi, K., Doreland, L. D., Schamiloglu, E., Mojahedi, M., Malloy, K., J., and Brown, E. R., "*Photonic Crystal: A new Quasi-Optical component for High-Power Microwaves*", IEEE Transactions on Plasma Science, Vol. 24, No. 3, pp. 1067-1070, June 1996.

[AGI 99] Agi, K., Malloy, J., Schamiloglu, E., Mojahedi, M., and Niver, E., "*Integration of Microstrip Patch Antenna with a Two-dimensional Photonic Crystal Substrate*", Electromagnetics. Special Issue: Theory and Applications of Photonic Band-Gap Materials. Vol. 19, No. 3, pp. 277-290, May-June 1999.

[BAB 95a] Baba, T., and Matsuzaky, T., "*Theoretical calculation of Photonic Gap in semiconductor 2-dimensional Photonic Crystals with various Shapes of Optical Atoms*", J. Appl. Phys., Vol. 34, pp. 4496-4498, August 1995.

[BAB 95b] Baba, T., and Matsuzaki, T., "*Polarisation changes in spontaneous emission from GaInAsP/InP two-dimensional photonic crystals*", Electronics Letters, Vol. 32, No. 20, pp. 1776-1778, 28th September 1995.

[BAH 80] Bahl, I. J., and Bhartia, P., "*Microstrip Antennas*", Artech House, 1980

[BAL 97] Balanis, C. A., "*Antenna Theory. Analysis and Design*", Second Edition, John Wiley & Sons, Inc. 1997

[BEL 95] Bell, P. M., Pendry, J. B., Martín Moreno, L., and Ward, A. J., "*A program for calculating photonic band structures and transmission coefficients of complex structures*", Computer Physics Communications 85, pp. 306-322, 1995.

[BOW 92] Bowden, C. M., Dowling, J. P., and Everitt, H. O., "*Special Issue: Development and Applications of Materials Exhibiting Photonic Band Gap*", J. Opt. Soc. Am. B, Vol. 10, no. 2, February 1992.

[BRI 46] Brillouin, L., "*Wave Propagation in Periodic Structures*", 2nd Edition (New York:Dover), 1946.

[BRO 93] Brown, E. R., Parker, C. D., and Yablonovitch, E., "*Radiation properties of a planar antenna on a Photonic-Crystal substrate*", Journal of Optic Soc. Am. B., Vol. 10, No. 2, pp. 404-407, February 1993.

[CAS 96] Casagne, D., Jouanin, C., and Bertho, D., "*Hexagonal photonic-band-gap structures*", Physical Review B, Vol. 53, No. 11, pp. 7134-7142, 15 March 1996.

[CHE 95] Cheng, C. C., and Scherer, A., "*Fabrication of photonic band-gap crystals*", J. Vac. Sci. Technol. B, Vol. 13, No. 6, pp. 2696-2700, Nov/Dec. 1995.

[CHI 99] Chigrin, D. N., Lavrinenko, A. V., Yarotsky, D. A., and Gaponenko, S. V., "*All-dielectric one-dimensional Periodic Structure for Total Omnidirectional Reflection and Partial Spontaneous Emission Control*", Journal of Lightwave Technology, Vol. 17, Nº 11, pp. 2018-2015, November 1999.

[CHU 99] Chutinan, A., and Noda, S., "*Effects of structural fluctuations on the photonic bandgap during fabrication on a photonic crystal*", J. Opt. Soc. Am. B, Vol. 16, No. 2, February 1999

[CLE 92] Clery, D., "*Reflections of a forbidden photon*", New Scientist, 5 December 1992.

[COL 99] Colburn, J. S., and Rahmat-Samii, Y., "*Patch Antennas on Externally Perforated High Dielectric Constant Substrates*", IEEE Transactions on Antennas and Propagation, Vol. 47, No. 12, pp. 1785-1794, December 1999.

[COL 99a] Collin, R., E., "Field Theory of Guided Waves", Second Edition. IEEE Press, 1999.

[DEM 99a] de Maagt, P. J. I., Gonzalo, R., and Crone, G., "*A novel 3-D photonic bandgap structure*" French Patent. Number 99 06013. 11 May 1999.

[DEM 99b] de Maagt, P. J. I. , Gonzalo, R., Reynolds, A., and Crone, G., "*Photonic Crystal Antennas*", E11 News, pp. 5-7, Summer 1999.

[DEM 99c] de Maagt, P. J. I. , Gonzalo, R. and Reynolds, A., "*PBG Crystals: periodic dielectric materials that control EM wave propagation*", Microwave Engineering Europe, pp. 35-43, October 1999.

[DEM 00] de Maagt, P. J: I. and Crone, G., "*(Sub)Millimetre Wave Antenna Technology for Upcoming ESA Misions*", Millennium Conference on Antennas & Propagation, Davos, Switzerland, 9-14 April, 2000.

[DOW 93] Dowling, J. P. And Bowden, C. M., "*Beat radiation from dipoles near a photonic band edge*", J. Opt. Soc. Am. B, Vol. 10, No. 2, pp. 353-355, February 1993.

[DUR 98] D'Urso, B., Painter, O., O'Briend, J., Tombrello, T., Yariv, A., and Scherer, A., "*Modal reflectivity in finite-depth two-dimensional photonic-crystal microcavities*", J. Opt., Soc., Am., B, Vol. 15, No. 3, pp. 1155-1159, March 1998.

[ELL 96] Ellis, T. J., and Rebeiz, G. M., "*MM-wave Tapered Slot antennas on Micromachined Photonic BandGap dielectrics*", IEEE MTT-S Digest, pp. 1157-1160, 1996.

[FAN 94] Fan, S., Villenueve, P. R., Meade, R. D., and Joannopoulos, J. D., "*Design of three-dimensional photonic crystal at submicron lengthscales*", Appl. Phys. Lett., Vol. 65, No. 11, pp. 1466-1468, 12 September 1994.

[FLE 99] Fleming, J. G., and Lin S. Y., "*Three-dimensional photonic crystal with a stop band from 1.35 to 1.95mm*", Optics Letters, Vol. 24, No. 1, pp. 49-51, January 1999.

[GRA 98] Grayden, O., "*Nature's nanostructures colour wings and stones"*, Opto & Laser Europe, Issue 51, pp. 31-26, June 1998.

[GON 98a] Gonzalo, R., Vázquez, J., de Maagt, P. y Sorolla. M., "*Full 2D Photonic Band Gap*", XIII National Symposium URSI98, Pamplona, Spain, pp. 279-281, September 1998.

[GON 98b] Gonzalo, R., Vázquez, J., Reynolds, A., de Maagt, P. and Sorolla, M., "*2D and 3D Photonic Band Gap Structures for Antennas Applications*", 10th International Symposium on Antennas, JINA'98, pp. 129-132, Nice, France, 17-19 November 1998.

[GON 98c] Gonzalo, R., "*Modelling of Photonic Band Gap Structures*". ESTEC Working Paper no 2008. December 1998.

[GON 99a] Gonzalo, R., Martinez, B., De Maagt, P. J. I., and Sorolla, M., "*Analysis of Photonic BandGap Patch Antennas*" Proceedings of ICEAA99. pp. 407-411, Torino. Italy, September 13-17, 1999.

[GON 99b] Gonzalo, R., Martinez, B., De Maagt, P. J. I., and Sorolla, M., "*Patch Antennas on Photonic Crystal Structures*", Antenna Application Symposium, pp. 195-202, Allerton, Illinois, EEUU, September 1999.

[GON 99c] Gonzalo, R., Martinez, B. and De Maagt, P. J. I., "*The effect of Dielectric Permitivity on the Properties of Photonic BandGap Devices*", Microwave and Optical Technology Letters, Vol. 23, No. 2, pp. 92-95, October 20, 1999.

[GON 99d] Gonzalo, R., De Maagt, P. J. I., and Sorolla, M., "*Enhanced patch antenna performance by suppressing surface waves using Photonic Band-Gap structures*". IEEE Transactions on Microwave Theory and Techniques, Mini-Special Issue on Electromagnetic Crystal Structure, Design, Synthesis, And Applications, Vol. 47, No. 11, pp. 2131-2138, November 1999.

[GON 00a] Gonzalo, R., Martinez, B., De Maagt, P. J. I., and Sorolla, M., "*Improved Patch antenna Performance by Using Photonic BandGap Substrates*", Microwave and Optical Technology Letters, Vol. 24, No. 4, pp. 213-215, February 20, 2000.

[GON 00b] Gonzalo, R., Sorolla, M., and De Maagt, P. J. I., "*Improvements in Antennas Using Photonic Bandgap Structures as Substrates*", Millennium Conference on Antennas & Propagation, Davos, Switzerland, 9-14 April, 2000.

[HEC 74] Hecht and Zajac, "*Optics*", Adisson-Wesley Reading, Mass. 1974.

[HO 90] Ho, K. M., Chan, C. T., and Soukoulis, C. M., "*Existence of Photonic Gap in periodic Dielectric Structures*", Physical Review Letters, Vol. 65, No. 25, pp. 3152-3155, 17 December 1990.

[HO 94] Ho, K. M., et al., "*Photonic band gaps in three dimensions: New layer-by-layer periodic structure*", Solid State Comm., Vol. 89, 413, 1994.

[HOR 99] Horii, Y., and Tsutsumi, M, "*Harmonic Control by Photonic Bandgap on Microstrip Patch antenna*", IEEE Microwave and Guided wave Letters, Vol. 9, No. 1, pp. 13-15, January 1999.

[HOW 72] Howell, J. Q., "*Microstrip Antennas*", IEEE-AP-S Int. Symp. Digest, pp. 177-180, 1972.

[JAM 79] James, J. R. and Henderson, A., "*High-Frequency Behaviour of Microstrip Open-Circuit Terminations*", IEE J. Microwaves, Optics and Acoustics, Vol. 3, pp. 205-218, 1979.

[JAM 81] James, J. R., Hall, P. S. and Wood, C., "*Microstrip Antenna. Theory and Design*", Peter Peregrinus Ltd., 1981

[JAM 89] James, J. R. and Hall, P. S., "*Handbook of Microstrip Antennas*", IEE Peter Peregrinus Ltd., 1989

[JOA 95] Joannopoulus, J. D., Meade, R. D., and Winn, J. N., "*Photonic Crystals. Molding the flow of light*", Princeton University Press. 1995.

[JOH 87] John, S., "*Strong localization of photons in certain disordered dielectric superlattices*", Phy. Rev. Letters, Vol. 58, pp. 2486-2489, 1987.

[JOH 99] Johnson, S. G., Fan, S., Villeneuve, P. R. and Joannopoulos, J. D., "*Guided modes in photonic crystal slabs*". Physical Review B, Vol. 60, No. 8, pp. 5751-5758, 15 August 1999.

[KAR 94] Karathanos, v., Stefanou, N., and Modinos, A., "*Planar defects in Photonic Crystals*", J. Phys.: Condens. Matter, Vol. 6, pp. 6257-6264, 1994.

[KAR 95] Karathanos, V., Stefanou, N., and Modinos, A., "*Optical activity of photonic crystals*", Journal of Modern Optics, Vol. 42, No. 3, pp. 619-626, 1995.

[KES 96] Kesler, M. P., Maloney, J. G., Shirley, B. L. And Smith, G. S., "*Antenna Design with the use of Photonic Band-Gap Materials as all-dielectric Planar Reflectors*", Microwave and Optical Technology Letters, Vol. 11, No. 4, pp. 169-174, March 1996.

[KNI 98] Knight, J. C., Birks, T. A., Cregan, R. F., Russell, P. St. J., and Sandro J. P., "*Large area photonic crystal fibre*", Electronic Letters, Vol. 34, No. 13, pp. 1347-1348, 21th June 1998.

[KRA 96] Krauss, T. F., De la Rue, R. M., and Brand, S., "*Two-dimensional photonic-bandgap structures operating at near-infrared wavelengths*", Letters to nature, Vol. 383, pp. 699-702, 24 October 1996.

[KUR 94] Kurizki, G., Haus, W. J., "*Photonic Band Structures*", Special Issue, Journal of Modern Optics, Vol. 41, No. 2, February 1994.

[KWE 95] Kweon, G. And Lawandy, N. M., "*Quantum electrodynamics in Photonic Crystals*", Optics Communications 118, pp. 388-411, 15 July 1995.

[LES 90] Lesurf, J., "*Millimetre-wave Optics, Devices and Systems*", Adam Hilger, 1990.

[LEU 97] Leung, K. Y., Biswas, R., Cheng, S-D., Sigalas, M. M., McCalmont, J. S., Tuttle, G., and Ho, K. M., "*Slot antennas on Photonic Band Gap Crystals*", IEEE Transactions on Antennas and Propagation, Vol. 45, No. 10, pp. 1569-1570, October 1997.

[LIN 93] Lin, S.Y., and Arjovalingam, G., "*Tunneling of electromagnetic waves in two-dimensional photonic cystals*", Optics Letter, Vol. 18, No. 19, pp. 1666-1668, October 1993.

[MAR 93] Marududin, A. A., and Mc Gurn, A. R., "*Photonic band structure of a truncated, two-dimensional periodic dielectric medium*", J. Opt. Soc. Am. B, Vol. 10, No. 2, pp. 307-313, February 1993.

[MAR 94] Maradudin, A. A., and McGurn, A. R., "*Out of plane propagation of electromagnetic waves in a two-dimensional periodic dielectric medium*", Journal of Modern Optics, Vol. 41, No. 2, pp. 275-284, 1994.

[MEA 93a] Meade, R. D., Rappe, A. M., Brommer, K. D., and Joannopoulos, J. D., "*Nature of photonic band gap: some insights from a field analysis*", J. Opt. Soc. Am. B, Vol. 10, No. 2, February 1993.

[MEA 93b] Meade, R.D., Rappe, A.M., Brommer, K. D., and Joannopoulos, J. D., "*Accurate theoretical analysis of photonic band-gap materials*", Physical Review B, Vol. 48, No. 11, pp. 8434-8437, 15 September 1993.

[MEA 94] Meade, R. D., Devenyi, A., Joannopoulos, D., Alerhand, O. L., Smith, D. A., and Kash, K., "*Novel applications of photonic band gap materials: Low-loss bends and high Q cavities*", J. Appl. Phys., Vol. 75, No. 9, pp. 4753-4755, 1 May 1994.

[MUN 74] Munson, R. E., "*Conformal Microstrip Antennas and Microstrip Phased Arrays*", IEEE Trans. on Antennas and Propagation, Vol. AP-22, pp 74-78, 1974.

[OLI 63] Oliner, A. A., "*Radiating Periodic Structures: Analysis in Terms of k vs b Diagrams*", Short Course on Microwave Field and Network Techniques, Polytechnic Institute of Brooklyn, June 1963.

[OLI 99] Oliner, A.A. Private communication.

[OLI 00] Oliner, A.A. Private communication.

[OZB 94a] Ozbay, E., Michel, E., Tutlle, G., Biswas, R., Sigalas, M., and Ho, K. M., "*Micromachined millimeter-wave photonic band-gap crystals*", Appl. Phys. Lett., Vol. 64, No. 16, pp. 2059-2061, April 1994.

[OZB 94b] Ozbay, E., Abeyta, A., Tutlle, G., Tringides, M., Biswas, R., Chan, C. T., Soukoulis, C. M., and Ho, K. M., "*Measurement of a three-dimensional photonic band gap in a crystal structure made of dielectric rods*", Physical Review B, Vol. 50, No. 3, pp. 1945-1948, 15 July 1994.

[OZB 94c] Ozbay, E., Michel, E., Tuttle, G., Biswas, R., and Ho, K. M., "*Terahertz spectroscopy of three-dimensional photonic band gap crystals*", Optics Letters, Vol. 19, No. 15, August 1, 1994.

[OZB 94d] Ozbay, E., Michel, E., Tutlle, G., Biswas, R., Ho, K. M., Bostak, J., and Bloom, D. M., "*Double-etch geometry for millimeter-wave photonic band crystals*", Appl. Phys. Lett., Vol. 65, No. 13, pp. 1617-1619, 26 September 1994.

[OZB 95] Ozbay, E., Tuttle, G., McCalmant, J. S., Sigalas, M., Biswas, R., Soukoulis, C. M., and Ho, K. M., "*Laser-micromachined millimeter-wave photonic band-gap cavity structures*", Appl. Phys. Lett., Vol. 67, No. 14, pp. 1969-1971, 2 October 1995.

[OZB 96] Ozbay, E., and Temelkuran, B., "*Reflection properties and defect formation in photonic crystals*", Appl. Phys. Lett., Vol. 69, No. 6, pp. 743-745, 5 August 1996.

[OZB 00] Ozbay, E., Temelkuran, B., Bayindir, M., Biswas, R., Sigalas, M., Tuttle, G., and Ho, K. M., "*Photonic Crystal Based Resonant Antenna With a Very High Directivity*", Millennium Conference on Antennas and Propagation, APS 2000, Davos, Switzerland, 9-14 April 2000,

[PAI 99] Painter, O., Vuckovic, J. and Scherer, A., "*Defect modes of a two-dimensional photonic crystal in an optically thin dielectric slabs*", J. Opt. Soc. Am. B, Vol. 16, No. 2, pp. 275-285, February 1999.

[PEN 96] Pendry, J. B., "*Photonic band structure*", J. Phys: Condens. Matter 8, pp. 1085-1108, 1996.

[PEN 98] Pendry, J. B., "*Can Sheared Surfaces Emit Light?*", Journal of Modern Optics, No. 45, pp. 2389-408, 1998.

[PIE 54] Pierce, J. R., "Coupling of Modes of Propagation", J. Appl. Physics, 25, pp 179-183, February 1954.

[POL 97] Pollagne, G., Lenormand, J., Poullguen, P., Mahdjoobi, K., Terret, C., and Gelin, Ph., "*Theoretical study of Interactions between Antennas and Metallic Photonic BanGap Materials*", Microwave and Optical Technoly Letters, Vol. 15, No. 6, pp. 384-389, August 20, 1997.

[QUI 99] Quian, Y., Coccioli, R., Sievenpiper, D., Radisic, V., Yablonovitch, E., and Itoh, T., "*A microstrip Patch Antenna Using Novel Photonic Band-Gap Structures*", Microwave Journal, pp. 66-76, January 1999.

[RAR 95] Rarity, J. and Weisbuch, C., "*Microcavities and Photonic Bandgaps: Physics and Applications*", Proceedings of the NATO Advanced Study Institute: Quantum Optics in Wavelenght-Scale Structures, Cargase, Corsica, August 26-September 2, 1995 (NATO ASI Series, Kluwer Academic Publishers, The Netherlands, 1996).

[RUS 86] Russell, P. St. J., ""*Interference of integrated Floquet-Bloquet waves*", Physical Review A., Vol. 33, No. 5, pp. 3232-3242, 1986.

[RUS 92] Russell, P. St. J., "*Photonic Band Gaps*", Physics World", pp. 37-42, August 1992.

[RUT 83] Rutledge, D. B., Neikirk, D. P., and Kasilingam, D. P., in Infrared ans Millimeter Waves Academic. Orlando, FL, Vol. 10, pp. 1, 1983.

[SAK 98] Sakoda, K., "*Numerical study on localized defect modes in two-dimensional triangular photonic crystals*", Journal of Applied Physics, Vol. 48, No. 3, pp. 1210-1214, 1 August 1998.

[SAK 99] Sakoda, K., Sasada, M., Fukushima, T., Yamanaka, A., Kawai, N., and Inove, K., "*Detailed analysis of transmission spectra and Bragg reflection spectra of a two-dimensional photonic crystal with a lattice constant of 1.15mm*", J. Opt. Soc. Am. B, Vol. 16, No. 3, pp. 361-365, March 1999.

[SCH 99a] Scherer, A., Doll, T., Yablonovitch, E., Everiit, H. O., and Higgins, J. A., "*Special Section on electromagnetic crystal Structures, Design, synthesis, and Applications*", Journal of Lightwave Technology, Vol. 17, No. 11, November 1999.

[SCH 99b] Scherer, A., Doll, T., Yablonovitch, E., Everiit, H. O., and Higgins, J. A., "*Mini-Special Issue on electromagnetic crystal Structures, Design, synthesis, and Applications*", IEEE Microwave Theory and Techniques, Vol. 47, No. 11, November 1999.

[SIE 96] Sievenpiper, D. F., Sickmiller, M. E., and Yablonovitch, E., "*3-D Wire Mesh Photonic Crystals*", Physical Review Letters, Vol. 76, No. 14, pp. 2480-2483, 1 April 1996.

[SIG 93] Sigalas, M. M., Soukoulis, C. M., Chan, C. T., and Ho, K. M., "*Photonic band gaps and defects in two dimensions: Studies of the transmission coefficient*", Physical Review B, Vol. 48, No. 19, pp. 14121-14126, 15 November 1993.

[SIG 96] Sigalas, M. M., Biswas, R., and Ho, K. M., "*Theoretical Study of Dipole Antennas on Photonic Band-Gap Materials*", Microwave and Optical Technology Letters, Vol. 13, No. 4, pp. 205-209, November 1996.

[SIG 97] Sigalas, M. M., Biswas, R., Li, Q., Crounch, D., Lleung, W., Jacobs-Woodbury, R., Lough, B., Nielsen, S., McCalmont S., Tuttle, G., and Ho, K. M., "*Dipole Antennas on Photonic Band-Gap Crystals – Experiment and Simulation*", Microwave and Optical Technology Letters, Vol. 15, No. 3, pp. 153-158, June 20, 1997.

[SIG 99] Sigalas, M. M., Biswas, R., Ho, K. M., Leung, W., Tuttle, G., Crounch, D. D., "*The Effect of Photonic Crystals on Dipole Antennas*", Electromagnetics, Special Issue: Theory and Applications of Photonic Band-Gap Materials, Vol. 19, No. 3, pp. 291-303, May June 1999.

[SMI 93] Smith, D. R., Dalichaouch, R., Kroll, N., Scholtz, S., McCall, S. L., and Platzman, P. M., "*Photonic band structure and defects in one and two dimensions*", J. Opt. Soc. Am. B, Vol. 10, No. 2, pp. 314-321, February 1993.

[SMI 99] Smith, S. G., Kesler, P. M., and Maloney, J. G., "*Dipole Antennas Used With All-Dielectric, Woodpile Photonic-BandGap Reflectors: Gain, Field Patterns, And Input Impedance*", Microwave and Optical Technology Letters, Vol. 21, No., 3, pp. 191-196, May 5 1999.

[SOU 95] Soukoulis, C. M., "*Photonic Band Gap Materials*", Proceedings of the NATO ASI onPhotonic Band Gap Materials, Elounda, Crete, Greece, June 18-30, 1995 (NATA ASI Series, Kluwer Academic Publishers, The Netherlands, 1996)

[SOZ 92] Sozuer, H. S., and Haus, J. W., "*Photonic bands: Convergence problems with the plane-wave method*", Physical Review B, Vol. 45, No. 24, pp. 13962-13972, 15 June, 1992.

[SOZ 94] Sozuer, H.S., and Dowling, J.P., "*Photonic band calculations for woodpile structure*", J. Mod. Opt., Vol. 41, 231, 1994.

[SUZ 95] Suzuer, H. S., and Haus, J. W., "*Photonic bands: Simple-cubic lattice*", J. Opt. Soc. Am. B, Vol. 12, No. 4, pp. 570-582, April 1995.

[SUZ 95a] Suzuki, T., and Yu, P. K. L., "*Emission power of an electric dipole in the photonic band structure of the fcc lattice*", J. Opt. Soc. Am. B, Vol. 12, No. 4, pp. 570-582, April 1995.

[SUZ 95b] Suzuki, T., and Yu, P. K. L., "*Dispersion relation at point L in the photonic band structure of the face-centered-cubic lattice with active or conductive dielectric media*", J. Opt. Soc. Am. B, Vol. 12, No. 4, pp. 583-591, April 1995.

[SUZ 95c] Suzuki, T., "*Photonic band structures and radiation in two or three dimensional periodic structures*", Ph. D. Dissertation, University of California, San Diego, 1995.

[WIN 98] Winn, J. N., Fink, Y., Fan, S., and Joannopoulos, J. D., "*Omnidirectional reflection from one dimensional photonic crystal*", Optics Letters, Vol. 23, No. 20, pp. 1573-1575, October 15, 1998.

[YAB 87] Yablonovitch, E., "*Inhibited spontaneous emission in solid state physics and electronics*", Phy. Rev. Letters, Vol. 58, pp. 2059-2062, 1987.

[YAB 89] Yablonovitch, E., and Gmitter, I. J., "*Photonic Band Structures: The face centered cubic case*", Phys. Rev. Let., Vol. 58, pp. 2059-2065, 1989.

[YAB 91] Yablonovitch, E., Gmitter, T. J., and Leung, K. M., "*Photonic band Structure: The face-centered-cubic case employing nonspherical atoms*", Phys. Rev. Lett., Vol. 67, pp. 2295-2300, 1991.

[YAB 94a] Yablonovitch, E., "*Photonic Band Gap Structures*", Journal Opt. Soc. Am. B, Vol. 10, No. 2, pp. 283-295, Feb. 1994.

[YAB 94b] Yablonovitch, E., "*Photonic Crystals*", Journal of Modern Optics, Vol. 41, No. 2, pp. 173-194, 1994.

[YAB 98] Yablonovitch, E., "*Engineered omnidirectional external reflectivity spectra from one-dimensional layered interference filters*", Optics Letters, Vol. 23, No. 21, pp. 1648-1649, November 1, 1998.

[YAN 97a] Yang, D., Alexopoulos, N. G., and Yablonovitch, E., "*Photonic Band-Gap Materials for High-Gain Printed Circuit Antennas*", IEEE Trans. on Antenna and Propagation, Vol. 45, No. 1, January 1997.

[YAN 97b] Yang, D., "*Characteristics of Guided and Leaky-Waves on Multilayer Thin-Film Structures with Planar Material Gratings*", IEEE Trans. on Microwave Theory and Techniques, Vol. 45, No. 3, March 1997.

[YAN 99] Yang, H. Y. D., "*Special Issue: Theory of Photonic Band-Gap Materials*", Electromagnetics, Vol. 19, No. 3, May-June, 1999.

[YAR 97] Yariv, A., "*Optical Electronics in Modern Communications*", Fifth Edition, Oxford University Press, Inc., 1997.

[1] IEE Proceedings, Optoelectronics, Special isuue on: Photonic Crystals and Photonic Microstructures, Vol. 145, No. 6, December 1998.

[2] http://home.earthlink.net/~jpdowling/pbgbib.html

[3] "Best Bets for 1999", SCIENCE, Vol. 282, pp. 2158, 18 December 1998.

[4] "*Science and Technology: New-age Crystals*", The Economist, Vol. 349, No. 8095, November 21st 1998.

[5] *HP High Frequency Structure Simulator*. User's Reference. September, 1997.

APPENDIX A

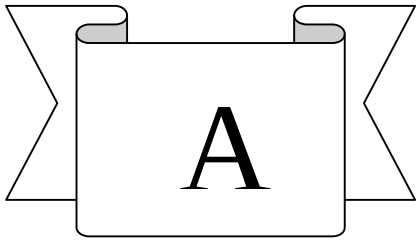

SURFACE WAVE MODES

There are a class of open-boundary structures which are able to guide electromagnetic waves. These structures support a mode which is intimately bound to the surface of the structure. The field is characterised by an exponential decay away from the surface and having the usual propagation function e^{-jbz} along the axis of the structure. For this reason, this discrete eigenvalue solution to the wave equation is called a *surface wave*, and the structure that guides this wave may be appropriately referred to as a *surface waveguide*.

Some of the most outstanding features of these kinds of waves are:

1. There always is a surface-wave mode with no low-frequency cut-off.
2. There are not an infinite number of discrete modes at a given frequency.
3. The existence of a finite number of discrete modes, together with an eigenfunction solution with a continuous eigenvalue spectrum.
4. The possibility of getting mode solutions with a phase velocity less than the light.

Although there are different kinds of surface wave structures (such as dielectric-coated plane, corrugated plane, corrugated cylinder), in this appendix,

the study of the surface wave modes along dielectric slabs will be developed (see Figure A.1).

Following the description given in [COL 99a], the equations that describe the surface wave for even TM modes are as follow,

$$\begin{aligned} e_r k_{xa} t &= k_{xd} t \cdot tan(k_{xd} t) \\ (k_{xa} t)^2 + (k_{xd} t)^2 &= (e_r - 1)(k_0 t)^2 \end{aligned} \tag{A.1}$$

where k_{xd} and k_{xa} are the propagation constant for $|x| \le t$ (dielectric substrate part) and $|x| \ge t$ (air part) respectively, k_0 is the free space wavenumber and t is the substrate thickness.

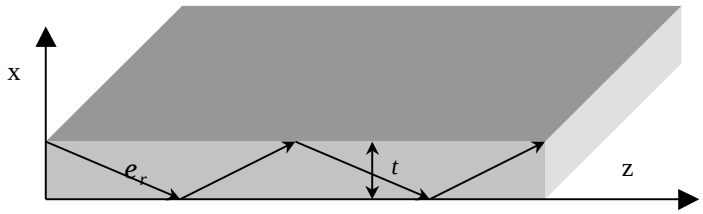

Figure A.1: Geometric representation of the dielectric slab.

The solution from these equations may be plotted on a $k_{xd}t$-$k_{xa}t$ plane. The points of intersection between the two curves determine the eigenvalues k_{xd} and k_{xa}. A typical plot for a dielectric constant of 2.56 is given in Figure A.2.

From Figure A.2, several conclusions can be extracted; the first even mode, which has been defined as TM_0 mode, has no cut-off frequency. Since k_{xa} must be positive for a surface mode, only those points that lie in the intervals $np \le k_{xd} t \le np + p/2$, where n is any integer, correspond to surface-wave solutions. There are different several modes in propagation when the t value is large enough. All the higher order modes will have a low-frequency cut-off. Points of intersection which occur in the range $np + p/2 \le k_{xd} t \le (n+1)p$ lead to solutions with negative values of k_{xa}. This means that these modes will increase exponentially away from the surface and correspond with no physical modes due to its amplitudes become infinite.

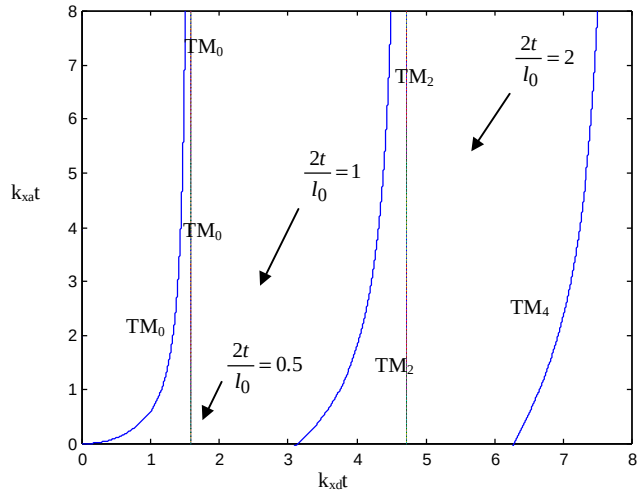

Figure A.2: Graphical solution for eigenvalues for even TM modes.

To get the cut-off frequencies of the higher order modes, the circle of value t / l_0 has to intersect the tangent curves along the $k_{xd}t$ axis (see Figure A.2 and equations A.1). The cut-off values are easy seen to be given by $k_{xd}t = np$, where the tangent value is zero, and, for the *n*th mode will be given by (substituting in equation A.1):

$$\left(\frac{t}{l_0}\right) = \frac{n}{2(e_r - 1)^{1/2}} \tag{A.2}$$

where *n* is an integer *n=0,1,2,.....*

Applying the same procedure for the case of odd TM surface wave modes, the following equations are inferred,

$$\begin{aligned} e_r k_{xa}t &= -k_{xd}t \cdot \cot(k_{xd}t) \\ (k_{xa}t)^2 + (k_{xd}t)^2 &= (e_r - 1)(k_0 t)^2 \end{aligned} \tag{A.3}$$

The proceeding way to solve these equations is similar to the even TM modes. A graphical solution as the plotted in Figure A.3 is obtained.

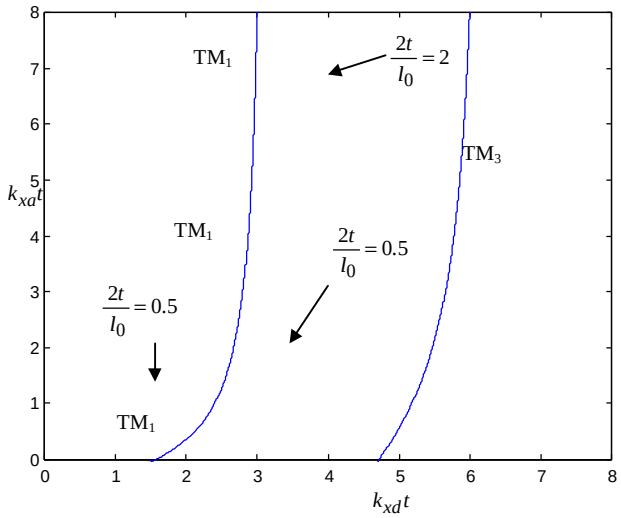

Figure A.3: Graphical solution for eigenvalues for odd TM modes.

For this case, only the points of intersection in the range intervals $np - p/2 \le k_{xd}t \le np$ produce surface wave modes with k_{xa} positive. The cut-off frequency points for the odd TM surface wave modes are given by:

$$\left(\frac{t}{l_0}\right) = \frac{2n+1}{4(e_r - 1)^{1/2}} \tag{A.4}$$

where *n* is an integer *n=0,1,2,.....*

Combining the cut-off frequencies equations for even and odd TM surface wave modes, the following general equation is obtained,

$$\left(\frac{2t}{l_0}\right) = \frac{n}{2(e_r - 1)^{1/2}} \tag{A.5}$$

where the even integers *n=0,2,4,....* are referred to the even modes and the odd integers *n=1,3,5, ...* to the odd modes.

Using the same developments, the equations for even and odd TE surface wave modes can be obtained. These are defined by,

$$k_{xa}t = k_{xd}t \cdot tan(k_{xd}t) \quad \text{even modes} \tag{A.6a}$$

$$k_{xa}t = -k_{xd}t \cdot \cot(k_{xd}t) \quad \text{odd modes} \tag{A.6b}$$

and

$$(k_{xa}t)^2 + (k_{xd}t)^2 = (e_r - 1)(k_0 t)^2 \tag{A.7}$$

The graphical solution from these equation systems is the same that was defined by TM modes.

As particular case of a dielectric slab of thickness *t* above a conducting plane, only odd solutions are possible, since E_z does not vanish at *x=0* for the even modes. As important, it should be noted that for the case of working with a grounded dielectric slab (microstrip structures), a TE surface wave mode with no low-frequency cut-off does not exist. Only the TM_0 surface wave mode will have not frequency cut-off and will always be in propagation.

As working key in microstrip structures, note that selecting adequately the t / l_0, only the TM_0 mode will be in propagation avoiding the excitation of other higher surface wave modes. This will be important to select the proper Photonic Band Gap structure to reject surface wave modes.

Normally, the surface wave modes along a dielectric slab are known as "trapped modes". The reason is because the surface wave mode incident into the dielectric-air interface is reflected back when the incident angle is greater than the critical angle q_c, where $sinq_c = e_r^{-1/2}$. The mode consists of a plane wave propagating along a zigzag path along the *z*-axis.

The dispersion relation for these surface wave modes, which informs about the propagation angle as function of the working frequency is plotted in Figure A.4. A grounded dielectric slab of $e_r = 10$ and $t = 1.27\,mm$ has been used to generate the plot. For this case, the critical angle value is $q = 18.44^o$, and $f = 71.56^o = 1.25\,rad$. From Figure A.4 it can be checked that the propagation of the surface wave mode is excited when the incident angle (q) is greater than the critical angle.

For any plane-dielectric sheet of given thickness, as it has been explained above, only a finite number of surface wave modes exist. These modes, obviously, do not form a complete eigensolution set in which the field from an arbitrary source can be expanded. This means that the surface wave modes do not represent the complete solution for a dielectric slab.

The results extracted following the description given in [COL 99a], are that; the complete solution for the physical field consists of one or more surface waves with $b > k_0$ (see Figure A.5), a continuous spectrum of waves with $0 < b < k_0$, and a continuous spectrum of evanescent waves with $b = -ja$ and $0 < a < \infty$. The field radiated by an arbitrary source will, in general, contribute to all three of the above types of fields.

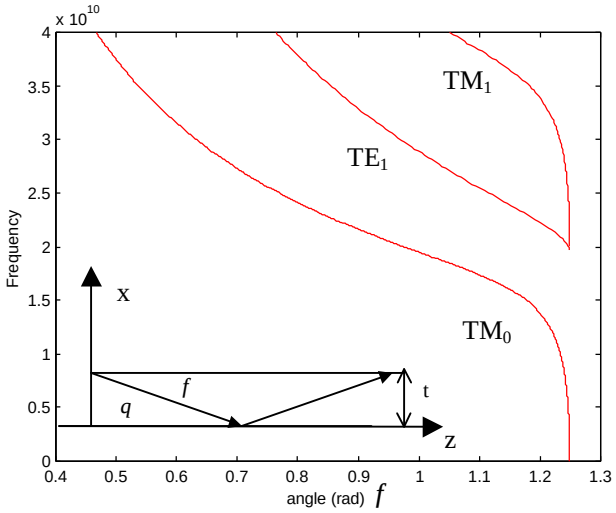

Figure A.4: Propagation angle as function of the frequency for the first surface wave modes.

In order to find the leaky wave modes, one has to search for solutions of k_{xa} that are not purely imaginary. To obtain these solutions, the $k_{xa}t$ and $k_{xd}t$ quantities have to be expressed as complex values,

$$\begin{aligned} k_{xa}t &= T + iU \\ k_{xd}t &= X + iY \end{aligned} \tag{A.8}$$

Substituting these quantities in the equation A.1, the leaky waves modes for even TM polarisation can be found,

$$e_r(T + iU) = (X + iY) \cdot tan(X + iY) \tag{A.9a}$$

$$(X + iY) = \frac{e_r \sqrt{(e_r - 1)}(k_0 t)}{\sqrt{e_r^2 + tan^2(X + iY)}} \tag{A.9b}$$

After separating the real and imaginary parts, T and U can be found as functions of X and Y from equation A.9a, and X and Y may be found as functions of X and Y from equation A.9b. By inspection of the two equations X(X,Y) and Y(X,Y) indicates that if (X1,Y1) is solution, then (X1,-Y1), (-X1,Y1) and (-X1,-Y1) are also solutions. Thus, it is sufficient to search only for the positive values of X and Y.

This procedure can be developed for each of the polarisations.

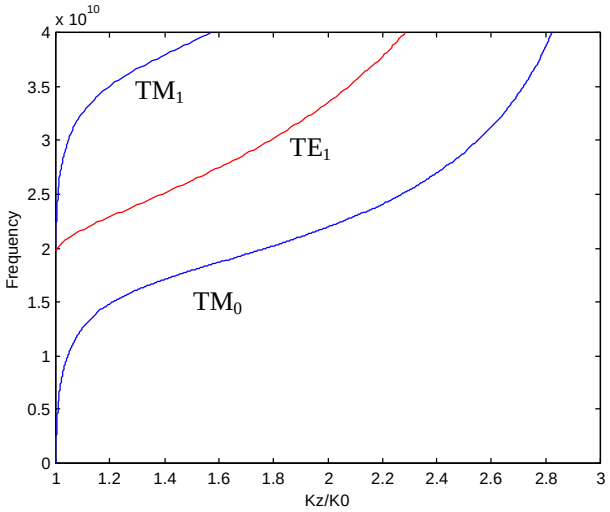

Figure A.5: Surface wave modes k_z / k_0 ratio as function of the frequency.

APPENDIX B

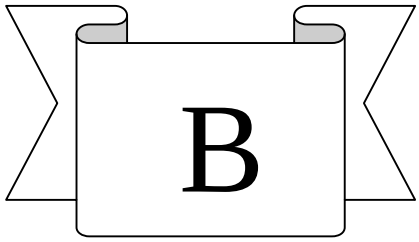

RADIATING PERIODIC STRUCTURES

The dispersion plots in the form of k versus β diagrams have been found useful for a long time for understanding the behaviour of electromagnetic periodic structures in closed waveguides. Most of the derivations in this appendix do find their origin from waveguide structures. Nevertheless, the theory may also be used to advantage in explaining the radiating periodic Photonic Crystal structures [OLI 63], which have appeared as real applications in Chapter 4.

B.1 Closed Waveguide Structures

Consider a typical periodically loaded waveguide of period d, which represents the length of a unit cell, and z is the transmission direction (see Figure B.1). If the time dependence is in the form e^{jwt}, and the cross-sectional dependence is suppressed, the Bloch theorem says,

$$\Psi(z) = e^{-j k_o z} P(z) \tag{B.1}$$

where

$$P(z) = P(z + d) \tag{B.2}$$

and where $\Psi(z)$ represents some field quantity. These equations explain that there is a fundamental travelling wave with propagation wavenumber k_0 and a standing wave, which is repeated each period d, which represents the local variations due to the periodicity itself .

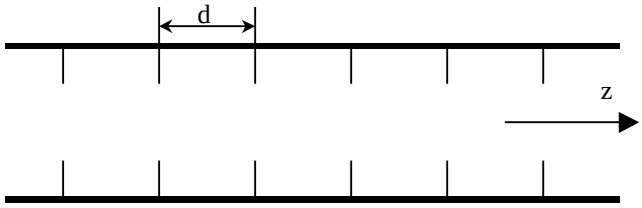

Figure B.1: A typical periodically loaded closed waveguide.

The standing wave can be represented by a summation of travelling waves, which can be written as a Fourier expansion as,

$$P(z) = \sum_{n=-\infty}^{\infty} P_n e^{-j\frac{2p}{d}nz} \tag{B.3}$$

This equation also satisfies the condition set in equation B.2, which leads to the next expression,

$$\Psi(z) = \sum_{n=-\infty}^{\infty} P_n e^{-j\left(k_0 + \frac{2p}{d}n\right)z} \tag{B.4}$$

or

$$\Psi(z) = \sum_{n=-\infty}^{\infty} P_n e^{-jk_n z} \tag{B.5}$$

with

$$k_n = k_0 + \frac{2p}{d}n, \qquad n = 0, \pm 1, \pm 2, ... \tag{B.6}$$

Relation B.5 states that the field can be expanded in terms of an infinite number of travelling wave components. One of each travelling wave component is called *space harmonic*. Therefore, the k_n values physically represent the propagation wavenumber of these space harmonic contributions to the total field. It should be noted that the space harmonics do not exist independently and are not modal solutions by themselves, they are part of the total solution which is composed of a combination of infinite space harmonics.

In order to show how the space harmonics influence on the dispersion diagrams, the simple case of only a travelling wave with its different propagation parameters is defined as follows, the quantity k is the free-space wave number with,

$$k = 2p / l \tag{B.7}$$

where λ is the free-space wavenumber, and it is related to w as,

$$k = \frac{w}{c} = w\sqrt{m_0 e_0} \tag{B.8}$$

where c is the velocity of light in the vacuum.

In a k versus β diagram, the phase and group velocity normalised to free space velocity can be written as,

$$\frac{v_f}{c} = \frac{k}{b} \tag{B.9}$$

$$\frac{v_g}{c} = \frac{dk}{db} \tag{B.10}$$

The dispersion curve normalised to the velocity of light of a travelling wave is plotted in Figure B.2, and consists on two straight lines at 45º since $b = \pm k$. The line with the negative slope refers to the wave travelling in the negative z direction.

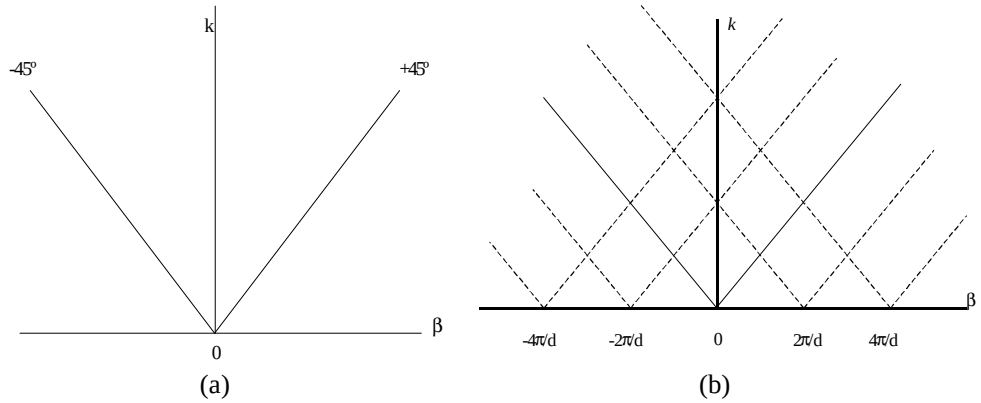

Figure B.2: k versus β diagram for (a) a travelling wave in an air filled waveguide and (b) the same but including all the space harmonics when infinitesimal periodic loading is introduced.

Now, if infinitesimally small periodic elements are introduced in such a way that the guiding structure remains unperturbed, an infinite number of space harmonics appear but leaving undisturbed the initial dispersion curve. Each of these space harmonics will also possess a dispersion curve of its own displaced by $2np/d$ from each other.

Following the explanation given in [PIE 54], in the real situation, a coupling between space harmonics appears. One of them is presented for modes with oppositely-directed group velocities, which results in a stop band (see Figure B.3). Within such stop band, κ is complex.

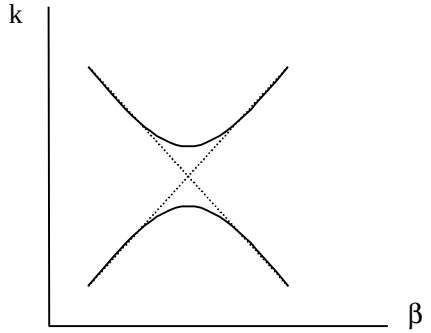

Figure B.3: Stop band behaviour due to mode-coupling effects.

The stop bands will result in a dispersion relation as pl otted in Figure B.4, although the shape will depend on the nature of the perturbing periodic elements. The branches of the curves are assigned to the different space harmonics.

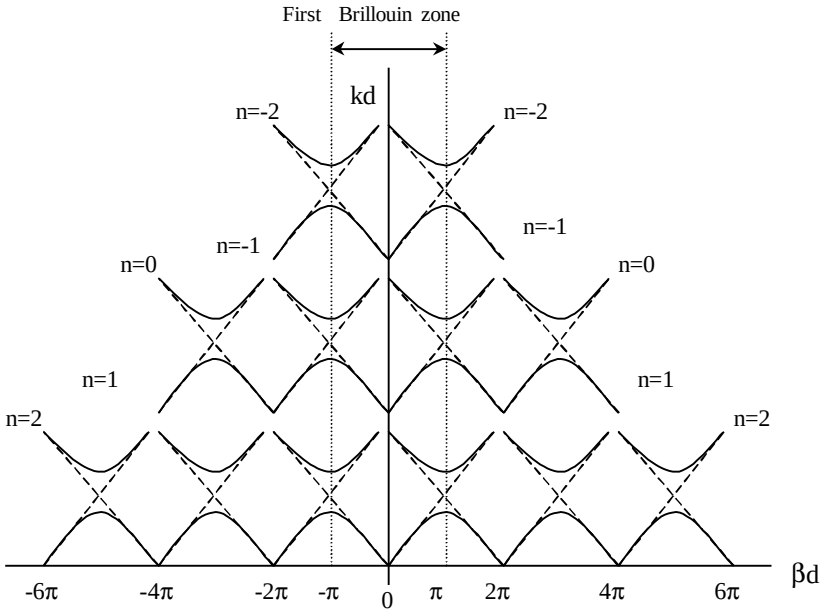

Figure B.4: *kd* versus *bd* dispersion diagram indicating the different space harmonics.

The dispersion curve is repeated every $bd = 2p$ along the abscissa axis, but the behaviour along the ordinate (*kd*) axis depends on the structure. The vertical strip from $bd = -p$ to $bd = p$ corresponds to the first Brillouin zone for these structures periodic in one dimension.

Figure B.4 also indicates that all the space harmonics corresponding to a given frequency (*kd*) possess the same slope and therefore the same group velocity. This result is according to physical expectations, due to the fact that energy in the total field has to travel as a unit.

Meanwhile, the phase velocity will depend on the space harmonic, some of them will travel faster than the free-space velocity while others are slow compared to it,

$$\frac{v_f}{c} = \frac{k}{b_0 + \frac{2p}{d}n} \quad , \qquad n = 0, \pm 1, \pm 2, ... \tag{B.11}$$

It is seen that for all space harmonics for which β is negative, the phase and group velocities are of opposite sign. These waves are called "backward waves".

As it was commented previously, in the stop band, the propagation wavenumbers κ_n of all the space harmonics are complex. Nevertheless, the attenuation constant α must be the same for all of the space harmonics because this corresponds with the mode attenuation,

$$k_n = \left(b_0 + \frac{2p}{d}n \right) - ja \tag{B.12}$$

While the real solution is composed of an infinite number of space harmonics, in practise only a finite number is significant. In general the amplitude of the space harmonics drops off sharply as the number of the space harmonic n moves away from n=0. At the stop bands, the two dominant space harmonics (n=0) with the same amplitude are crossed to produce the band gap.

In the periodic structure each space harmonic has a different transverse wavenumber (perpendicular to the propagation direction), this value is given by,

$$k_{tn} = \sqrt{k^2 - \left(k_0 + \frac{2p}{d}n \right)^2} \tag{B.13}$$

If n is such that $\left(k_0 + \frac{2p}{d}n \right)^2 > k^2$ at any given frequency, the space harmonic is a slow wave $(v_f < c)$ and k_{tn} is imaginary. This is the normal behaviour for the most of the space harmonics.

Nevertheless, if $\left(k_0 + \frac{2p}{d}n \right)^2 < k^2$, the space harmonics become in fast waves $(v_f > c)$ and the k_{tn} values are real.

In a closed structure, the slow waves correspond with attenuating space harmonics in the transverse direction and the fast wave with propagating space harmonics.

B.2 Open Periodic Structures

An open structure will be considered those whose cross-section is limited (not infinite or not metallic walls) in some transverse direction. These structures have an interface, which separates the guiding region from the external open region.

An example of these open structures is the case analysed in chap ter 4. This one corresponds to a 2-dimensional structure of drilled holes working as substrate for an antenna configuration, which is limited in the upper part by air.

The k versus β dispersion diagram studied for closed structures is also applicable to open structures, but taking into account some differences.

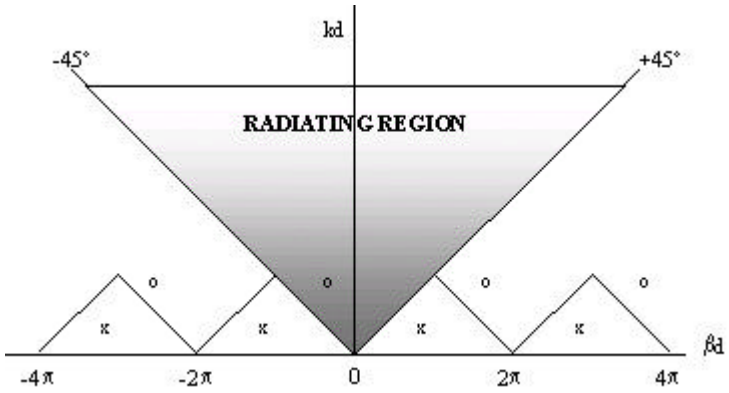

Figure B.5: *kd* versus *bd* for an open structure indicating the radiation region and the triangles for purely bound regions.

Considering Figure B.5, if a point on the dispersion curve for the open structure lies anywhere in the shaded region, the space harmonic corresponds to a fast wave. The transverse wavenumber k_{tn} is real. For the case of closed waveguides, the longitudinal wavenumber k_n remains purely real. However, in open waveguides, there is no opposite wall to reflect the wave which is transversely above cut-off for real values of k_{tn}, and as a result, radiation of energy occurs away from the interface, and k_n becomes complex. The shaded region in Figure B.4 is then labelled as radiating region.

Now, considering a point inside of one of the triangles (crosses in Figure B.5). Since, the rest of the space harmonic differ from this one by $bd = 2np$, this means that all the space harmonics are within the triangular regions, and no space harmonic solution exist in the radiation region. So, the total field will be completely bounded and this solution will correspond to guided modes.

If the solution occurs at the circles plotted in Figure B.5, then, at least one space harmonic solution appears within the radiating region, and the total solution is not completely bounded. Another consideration could be structures in which the solution lie within a triangle but near to one of its sides, under such conditions, a space harmonic may be radiating even though its phase velocity is slow.

As summary, if the harmonic solutions lie within the triangles, the total field is completely bound, the propagation wavenumber κ_n of all space harmonics are real, and all values of k_{tn} are purely imaginary. Such solution corresponds to "guided modes" or "surface waves". If at least one of the space harmonic solution lies in the radiation region, the field is not completely bound and some radiation away from the interface is produced. The values of κ_n for all the space harmonics are complex with the same value for the attenuation constant α.

It is clear that in a radiating period ic structure, the space harmonics are not either completely bound or completely radiating. The radiating space harmonics are called "leaky waves".

A surface wave on an interface possesses a field, which is completely bound to the interface. The propagating wavenumber along the interface corresponds to that of a slow wave and the field decays exponentially from the interface in the direction transverse to it. A completely bound field only occurs for sufficiently low frequencies or small periods.

When the value of *kd* is made sufficiently high a surface wave is not longer possible and one or more space harmonics will become radiating, appearing as leaky waves. The number of radiating beams at any given frequency is directly equal to the number of space harmonic solutions in the radiating region. The beam angle from broadside is given by,

$$\sin\theta_n = \frac{b_n}{k} \tag{B.14}$$

APPENDIX C

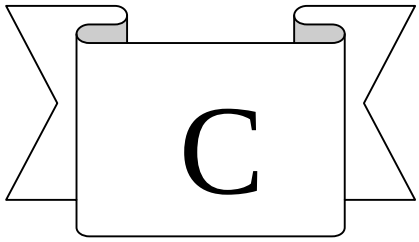

MPI CONFIGURATION

A basic explanation about the theoretical functioning of the MPI configuration will be developed. The mathematical process can be followed using Figure C.1.

Let us suppose that the source is formed by a single frequency signal, where *V* stands for the vertical polarisation and *H* for the horizontal one. The input plane-wave signal E_i of the wavelength λ and amplitude A will be of the form,

$$E_i = V \cdot A \cdot sin\left(\frac{2pct}{l}\right) \tag{C.1}$$

After crossing the beam splitter, a reflected field E_r and a transmitted field E_t will be generated, such that

$$\begin{aligned} E_r &= (V+H)\frac{1}{2}A \cdot sin\left(\frac{2pct}{l}\right) \\ E_t &= (V-H)\frac{1}{2}A \cdot sin\left(\frac{2pct}{l}\right) \end{aligned} \tag{C.2}$$

The output from one of the roof mirror will be a component polarised in the *V-H* direction when the input is a *V+H* polarised component and the output of the another roof mirror will be the *V+H* polarised component for a *V-H* polarised component input.

The field component returned to the beam splitter, after reflecting in the roof mirrors, will be on the form,

$$\begin{aligned} E_r' &= (V-H)\frac{1}{2}A\cdot sin\left(\frac{2p(ct-Z_1)}{l}\right) \\ E_t' &= (V+H)\frac{1}{2}A\cdot sin\left(\frac{2p(ct-Z_2)}{l}\right) \end{aligned} \tag{C.3}$$

where Z_1 and Z_2 are the distances covered in going to the roof mirrors to the polarising beam splitter and back.

The reflected and transmitted components recombine after the beam splitter generating a field such that,

$$E_0 = E_t' + E_r' \tag{C.4}$$

which is directed towards the detector.

Using standard trigonometric identities, E_0 may be written in the form,

$$\begin{aligned} E_0 = V\cdot A\cdot sin\left(\frac{p(2ct-Z_1-Z_2)}{l}\right)\cos\left(\frac{p(Z_1-Z_2)}{l}\right)+ \\ H\cdot A\cdot\cos\left(\frac{p(2ct-Z_1-Z_2)}{l}\right)sin\left(\frac{p(Z_1-Z_2)}{l}\right) \end{aligned} \tag{C.5}$$

Finally, by using the polarizer, the horizontal and vertical components can be directed to different detectors (see Figure C.1). The output from these detectors will indicate the power levels,

$$\begin{aligned} E_V = V\cdot A\cdot sin\left(\frac{p(2ct-Z_1-Z_2)}{l}\right)\cos\left(\frac{p(Z_1-Z_2)}{l}\right) \Rightarrow \\ P_V = \frac{1}{2}A^2\cos^2\left(\frac{p(Z_1-Z_2)}{l}\right) \end{aligned} \tag{C.6}$$

$$E_H = H \cdot A \cdot \cos\left(\frac{p(2ct - Z_1 - Z_2)}{l}\right) sin\left(\frac{p(Z_1 - Z_2)}{l}\right) \Rightarrow$$

$$P_H = \frac{1}{2} A^2 sin^2\left(\frac{p(Z_1 - Z_2)}{l}\right) \quad \text{(C.7)}$$

The output power levels will vary in function of the relative distance between the beam splitter and each one of the roof mirrors.

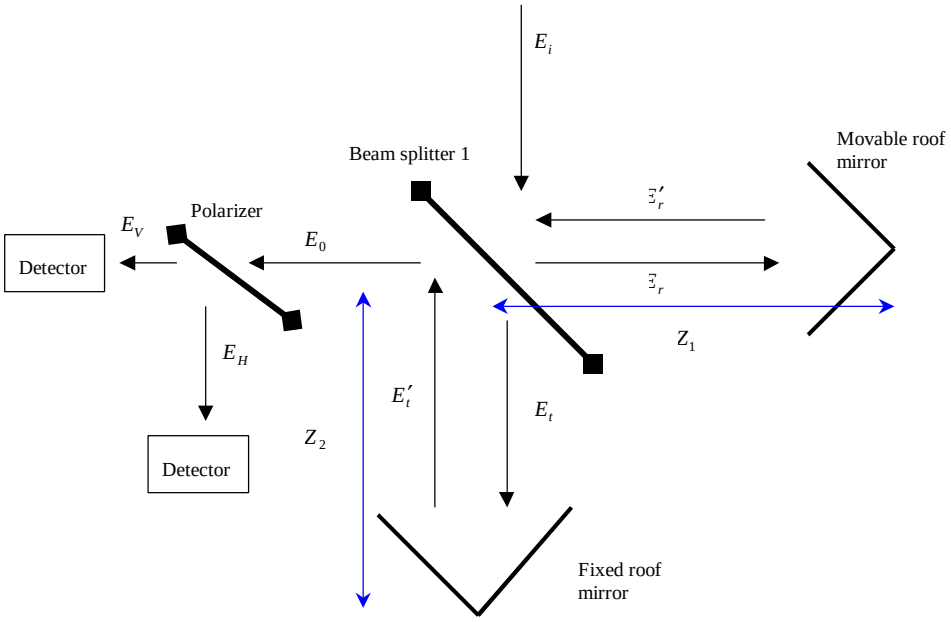

Figure C.1: Martin-Pupplet Interferometer configuration.

From the configuration used for the measurements (see Chapter 5) it is assumed that the input signal enters the system by being transmitted through the input polarizer and hence it is plane polarised with its electric field in the horizontal direction. At the output, only the vertical component of the field will therefore arrive at the detector; the horizontal component will be reflected back to the system, due to the last polarizer placed at the system. It will lead to an increasing in the system noise and a reduction of the dynamic range.

In the case of a broadband signal as input, the output signal has a shape as in Figure C.2a. In the case of a single frequency signal as in Figure C.2b.

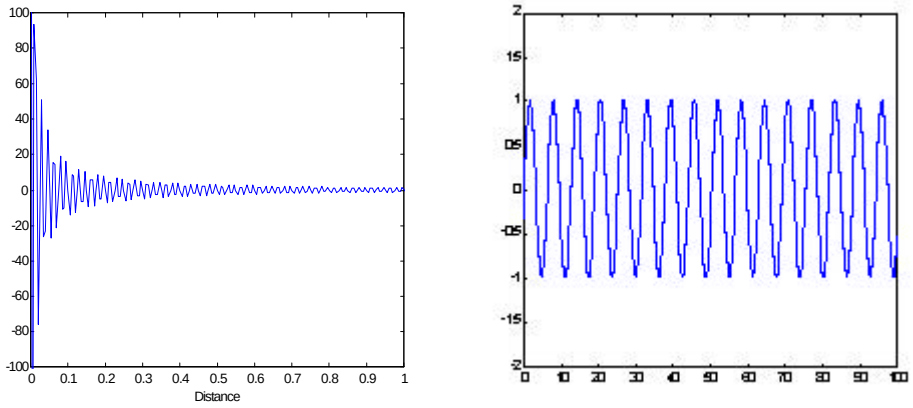

Figure C.2: Output power of the MPI system. (a) In the case of a broadband or (b) a single frequency input.

An interfero meter does not provide a direct measurement of signal frequency. Instead, measuring how the modulated signal varies as a function of the path difference, the signal frequency can be obtained. To make spectral measurements, the Fourier Transform Spectrometer (FTS) will be used. The expression for the FTS will be of the form,

$$A^2(f) = \frac{1}{D}\int_{-D}^{D} P(\Delta)\cdot\cos\left(\frac{2pf\Delta}{c}\right)d\Delta \qquad \text{(C.8)}$$

where, D is the maximum path moved by the movable roof mirror, Δ is the path difference $(Z_1 - Z_2)$ and P(Δ) is the detected power as function of the path difference.

If the range $2D$ were infinite, each calculated value of $A(f)$ would depend only on the level of the spectral component at the single frequency f. As it is impossible to perform the measurements over an infinite range of $2D$ values, the accuracy of the calculated $A(f)$ values will be limited. This limited accuracy is translated in a finite *spectral resolution*. In a general way, this spectral resolution is limited to $c/4D$. This means that any value of $A^2(f)$ will be affected for the rest of the spectral components over a range of frequencies centred upon f and span $c/8D$.

In reality, the *P(D)* value is measured at a discrete set of locations which are equally spaced some distance d apart. The measurements will be a series of values *P(md)*. As the amount of information measured will be finite, the *sampling theorem* has to be satisfied, this means,

1.-For a signal where *l* corresponds to the shortest component wavelength present, the change in path difference d between adjacent samples must be less than *l/2*.

2.- The samples must be measured sufficiently accurately such that this one is limited only by the random noise level present on the signal.

Satisfying these conditions, the set of sampled values *P(md)* will be identical to the continuous signal *P(D)*. Once the complete set of data samples has been measured, the calculation may proceed by replacing the integrals with equivalent series.

Finally and due to the modern computational methods, the Fast Fourier Transform is calculated instead of the Fourier Transform. A typical FFT routine can perform the required calculation without loosing information in from a tenth to a thousandth of the time required to compute the standard Fourier Transform. The only requirement for the FFT is that the number of input samples has to be 2^n, where *n* is an integer and the samples have to be equally spaced.